QUANTIFYING ENTRAINMENT AND DILUTION IN NUMERICAL SIMULATIONS
OF DEVELOPING THUNDERSTORMS

BY

LUKE ROBERT ALLEN

THESIS

Submitted in partial fulfillment of the requirements
for the degree of Master of Science in Atmospheric Sciences
in the Graduate College of the
University of Illinois at Urbana-Champaign, 2020

Urbana, Illinois

Adviser:

Professor Sonia Lasher-Trapp

ABSTRACT

Entrainment is the process by which turbulent clouds draw environmental air inward, and this process has long been understood to dilute the cloud, i.e., reduce the cloud liquid water content, buoyancy, and updraft velocity. In cumuli, entrainment results from overturning thermal circulations near cloud top. Past observational and numerical modeling studies have shown that in environments with significant vertical wind shear, the down-shear circulation is stronger. It has been hypothesized that greater entrainment (and thus dilution) occurs in stronger shear environments, but this relationship has not been suitably demonstrated with direct calculations of entrainment. This lack of understanding has consequences on the numerical weather prediction of convective initiation and development, as well as climate modeling.

Here, entrainment is quantified within six different high-resolution numerical simulations of developing thunderstorms in environments with different wind profiles to understand the role of vertical wind shear in modulating cumulus entrainment. Entrainment is directly quantified using the mass flux across a defined cloud core surface. Greater entrainment consistently occurs in simulated storms developing in environments with greater vertical wind shear, due to stronger overturning thermal circulations near the cloud tops, and greater storm-relative inflow on the down-shear side of the cloud.

Evaluations of the dilution produced by entrainment in the developing storms is often obscured by successive thermals in the sheared environments, often rising through the remains of previous thermals that modified the air entrained by the later thermals. The storms growing in strong-shear environments are also broader, so a smaller fraction of the cloud is affected by each individual entrainment event. Precipitation production appeared to be more related to the time

the cloud had been present, and the aid of successive thermals, than entrainment and dilution. Thus, while more entrainment occurs in the higher-shear environments, and stronger forcing is required for the storms to develop, the enhanced interaction of successive thermals in such environments, as well as their enhanced core widths, can enable the development of deep convective storms.

ACKNOWLEDGEMENTS

TABLE OF CONTENTS

CHAPTER 1: INTRODUCTION

1.1 Cumulus Entrainment and the Role of Thermals

Entrainment is the process by which turbulent clouds draw environmental air inward. This air is then mixed into the cloud, which can lead to *dilution*, or the reduction of cloud liquid water content (LWC) and updraft buoyancy. *Detrainment* is the process by which cloudy air is transported outward into the environment. Entrainment, mixing, and subsequent dilution can have profound effects on the development and precipitation output of the cloud: the rate of vertical cloud growth can be slowed (e.g. Malkus and Scorer 1955), and the precipitation can be reduced (e.g. Jonas and Mason 1982) or even precluded from forming. Over greater temporal and spatial scales, these processes can influence climate through modification of cloud radiative properties and precipitation (e.g. Del Genio 2012).

Early studies often focused on understanding the structure of vertical motion within the cloud and how it contributed to entrainment (e.g. Stommel 1947, Scorer and Ludlam 1953, Malkus and Scorer 1955, Morton et al. 1956, Squires 1958). Observational studies during this time found low values of LWC to be randomly distributed throughout the cloud, and some researchers thought entrainment to largely be caused by *penetrative downdrafts* (Squires 1958), such that vertical, rather than horizontal, mixing of environmental air led to dilution. Evaporative cooling or dynamical forcing was thought to cause mixed parcels to descend, thus forming a downdraft (Blyth 1993). There was disagreement at the time on how cumulus clouds could be described by a mathematical model. The three possibilities were described as the *plume, thermal,* and *starting plume* models, which originated from laboratory tank experiments (e.g. Morton et al. 1956, Woodward 1959, Turner 1962). Plumes could be described as a "maintained" source of

buoyancy (Morton et al. 1956), while thermals could be described as an "instantaneous" source of buoyancy (Woodward 1959). Starting plumes had characteristics of both plumes and thermals (Turner 1962). Later observational studies started to build a consensus that the vertical motions within shallow cumulus clouds strongly resembled laboratory thermals (e.g. French et al. 1999, Blyth et al. 2005). These thermals are associated with an overturning *toroidal circulation*, as illustrated in Fig. 1. As a result of this circulation, a substantial amount of entrainment occurs laterally, but mainly in the upper part of the cloud. Blyth et al. (2005) observed regions of reduced LWC at the center of thermals due to the inward flux of environmental, dry air at the bottom of the thermal circulation that was introduced into the central updraft. Despite these findings, most modern-day convective parameterization schemes in numerical weather prediction and climate models are based upon properties of the plume model, where entrainment is occurring laterally throughout the cloud depth, rather than near the upper part of the cloud. It may not be such a bad assumption for clouds containing multiple, or successive, thermals, or when representing an ensemble of many clouds, as entrainment patterns can then appear plume-like (e.g. de Rooy et al. 2013, c.f. Fig. 2 in Moser and Lasher-Trapp 2017).

When strong environmental vertical wind shear is present, the down-shear side of toroidal circulations tends to be enhanced, while the up-shear side is suppressed. This creates what is referred to as a *P-type circulation* (Kitchen and Caughey 1981, Zhao and Austin 2005) in the growing cloud, as shown in Figure 2. It has been thought that a P-type circulation entrains more than a symmetrical toroidal circulation (Malkus 1954, Blyth et al. 2005), but this conjecture has never been examined quantitatively. While environmental wind shear is known to strongly influence the eventual convective mode of storms, with greater shear required for organized convection (e.g. Weisman and Klemp 1982, 1984), it is also commonly accepted that vertical

2

wind shear inhibits the initial development of convection (e.g. Peters et al. 2019). There is yet no consensus if this limiting effect of shear is related to enhanced entrainment.

1.2 Dilution Effects of Entrainment on Cumulus Convection

The simplest observable effect of entrainment and mixing in cumuliform clouds is the reduction of LWC, evidence of dilution of the cloud core. Warner (1955) observed a decrease in the ratio of LWC to adiabatic liquid water content (ALWC) with height. Here, an 'adiabatic' parcel is one which does not exchange mass or energy with its environment as it is lifted from cloud base (and thus also does not lose mass via precipitation). Thus, ALWC is a theoretical maximum value for LWC. While earlier studies found low values of LWC to be randomly distributed throughout the cloud, Blyth et al. (2005) found regions of significantly reduced LWC near the center of moist thermals, when aircraft sampling accounted for the locations of rising thermals. A reduction in the LWC should ultimately reduce the precipitation produced over the course of the cloud lifetime. Although small amounts of entrainment and mixing may actually aid the initial onset of raindrop growth by collision-coalescence, through broadening of the droplet size distribution by droplets encountering varying supersaturation histories (e.g. Cooper 1989, Lasher-Trapp et al. 2005, Cooper et al. 2013), substantial reduction in LWC will always inhibit precipitation, or even prevent it altogether.

The buoyancy of ascending cloud parcels is also reduced by entrainment (deviating from an adiabatic prediction), which can ultimately limit the vertical development of the cloud. The buoyancy of an air parcel results from its lower density in the parcel compared to its environment at the same height, which is generally caused by higher temperatures in the buoyant parcel. Therefore, any mixing between the air in the cloud and the environmental air will reduce the

density difference and thus the buoyancy forcing the updraft (Scorer and Ludlam 1953, Woodward 1959). Evaporation of cloud droplets due to mixing of the entrained dry air within the cloud leads to latent cooling and a further reduction of buoyancy in the cloud. Additionally, the vertical momentum of environmental air should generally be much smaller than that of air in ascending cloud parcels, so the upward momentum of air parcels in the cloud is also reduced through entrainment and mixing (Scorer 1957). Thus, the updraft speed of air parcels experiencing entrainment will be reduced compared to the adiabatic values, and such parcels will not reach the same altitude as adiabatic parcels.

Dilution of the cloud by entrainment of environmental air is not always straightforward, as the 'environmental' air can have properties influenced by any previous cloud turrets, as most developing cumuli evolve through a series of *successive thermals* (Scorer and Ludlam 1953) that may travel through the wakes of their predecessors. This air, influenced by the passage of previous thermals, may be warmer and/or moister than the undisturbed environmental air. Scorer and Ludlam (1953) described the wake behind ascending thermals as "a region where the ascent of further bubbles is favoured." Thermals ascending through the wakes of previous thermals thus entrain air which has been modified from its original environmental state, as described by Saunders (1961). These successive thermals have been observed often. Blyth and Latham (1993) observed cumulus clouds with several ascending 'turrets' from aircraft observations of clouds in New Mexico. French et al. (1999) described pulsating growth resulting from multiple ascending bubbles indicated by radar reflectivity and velocity observations of shallow cumulus in Florida. Damiani et al. (2006) identified transient thermals, as indicated by their associated toroidal circulations, occurring in succession in airborne radar observations of cumulus in Colorado. The 'preconditioning' of the environment by older thermals allows later thermals to ascend a greater

4

distance, thereby promoting growth of the cloud (Kirschbaum 2011). Numerical simulations analyzed by Moser and Lasher-Trapp (2017) revealed a sharply reduced rate of dilution in numerically simulated successive thermals, relative to that experienced by the first thermal ascending into an undisturbed environment, even if later thermals had a stronger entrainment rate. The dilution of a numerically simulated cloud core by entrainment is generally reduced by the presence of a 'moist shell' around the core, and thus while entrainment should correspond to dilution, there is not always a strong correlation (e.g. Romps 2010, Hannah 2017, Moser and Lasher-Trapp 2017).

1.3 Prior Calculations of Entrainment and Detrainment

As stated above, entrainment generally leads to dilution, i.e. a reduction of cloud water content and buoyancy. Many past studies have made use of this cause-effect relationship to infer the origin level of entrained air from observations of *tracer variables,* such as the wet-equivalent potential temperature and the total water mixing ratio, which should be conserved in shallow, non-precipitating convection (e.g. Paluch 1979, LaMontagne and Telford 1983, Blyth et al. 1988). However, this method can be problematic (Grabowski and Pawlowska 1993), in that it can lead to an overestimate of the height of the source level of entrained air. Furthermore, while such "mixing diagrams" might have indicated the occurrence of cloud-top entrainment, LES particle tracking has shown that lateral mixing is far more significant (Heus et al. 2008).

Due to the difficulty in directly observing entrainment and detrainment, large eddy simulation (LES) studies have largely been used in recent years to investigate these processes. Large eddy simulations are capable of resolving the largest turbulent eddies within clouds, which are likely responsible for the most entrainment (de Rooy et al. 2013). Many of these studies have

also made use of tracer variable budgets (e.g. Siebesma and Cuijpers 1995, Romps and Kuang 2010) or vertical distributions of water content and/or updraft velocity (e.g. Zhao and Austin 2005, Peters et al. 2019) to infer the rate of entrainment from the dilution occurring in the simulation. The method of tracer variable budgeting is referred to as the *bulk-plume method,* and was historically used to evaluate entrainment.

In contrast, *direct calculation* of entrainment in LES studies has been a relatively recent development (Romps 2010, Dawe and Austin 2011). It generally involves calculating the air mass flux into a cloud or cloud core volume. Romps (2010) used passive particle tracers to quantify entrainment directly. This method involved tracking the 'activity' of air parcels (i.e. whether they exceeded thresholds of vertical velocity and hydrometeor mixing ratio). The particle tracer method produced entrainment and detrainment values roughly twice as large as those found using a bulk-plume method. This difference was attributed to the occurrence of dilution rates slower than expected for a given rate of entrainment, as discussed in Section 1.2. In a different approach, Dawe and Austin (2011) calculated the mass flux into the cloud cores, with a *cloud core* defined by the volume in which vertical velocity and condensate mass both exceeded some user-defined threshold values. The core surface was then interpolated onto the sub-grid scale using a tetrahedral interpolation scheme. This method allows for instantaneous entrainment rates to be calculated, and resulted in slightly smaller rates of entrainment and detrainment than that of Romps (2010), although the two methods correlated well. Both methods require high temporal output and thus are computationally expensive, and require high spatial resolution.   The method of Dawe and Austin (2011) partially mitigates the effects of the finite spatial resolution by locating the "core" of the cloud at a sub-grid scale, through which surface the max fluxes are quantified.

1.4 Entrainment in Deep Convection

While a substantial amount of work has been done on investigating entrainment in numerically-simulated shallow convection, comparatively little work has been done on entrainment in deep convection (i.e. cumulonimbus or cumulus congestus). Deep convection produces abundant precipitation over the earth, and while entrainment can in principle limit its development and precipitation production, a lack of (safe) observational techniques for studying its effects have limited progress. Thus, numerical modeling studies are currently the only option for studying entrainment in deep convection.

Derbyshire et al. (2000) used cloud-resolving model simulations and parallel single-column model tests to investigate the sensitivity of moist convection to mid-tropospheric humidity. The authors determined that mixing between clouds and environment was an important aspect, and fundamental differences between convection schemes were largely related to mixing processes. Kirschbaum (2011) found the transition from shallow convection to deep convection can be favored when the impacts of entrainment are suppressed (e.g. by moister mid-level flow). Convective parameterizations in global climate models (GCMs) have tended to underestimate entrainment into developing clouds, thus producing deep convection too easily. This issue can affect diurnal and seasonal cycles of convective precipitation, particularly over continents, in GCM simulations (Del Genio 2012). Knight et al. (2007) and Klocke et al. (2011) found that more variance in climate sensitivity was explained by the variance in entrainment in shallow convection compared to any other variable the authors examined, and Klocke et al. (2011) found the representation of entrainment in deep convection also affected climate model skill.

The question of why deep convection is suppressed in environments with strong vertical wind shear remains open. Peters et al. (2019) recently investigated the effects of shear on numerically simulated developing thunderstorms, and concluded that the difference in the ascent rate of thermals in a strong-shear and a no-shear environment was not caused by entrainment, but instead by an enhanced downward-oriented dynamic pressure acceleration in simulations with strong vertical wind shear. However, entrainment was quantified in that study only as its effects in reducing the vertical momentum budget by advecting air inward with less vertical momentum (i.e., one form of dilution). Conversely, Engelsen (2018) directly quantified entrainment into similar numerically simulated clouds and found greater entrainment rates in the simulation with wind shear. The latter result, in combination with the effects of entrainment on buoyancy discussed in section 1.2, appear to conflict with the result of Peters et al. (2019). Notably, entrainment was quantified in different ways (indirectly versus directly) in each of these studies, so it may therefore be the difference in methods leading to the different results.

Some LES studies of entrainment in cumulus congestus have been conducted using observed environmental soundings or soundings based on observations (e.g. Carpenter et al. 1998, Moser and Lasher-Trapp 2017, Romps 2010), while other studies of developing deep convection (e.g. Engelsen 2018, Peters et al. 2019) have used idealized soundings, such as that of Weisman and Klemp (1982). While using observed wind profiles can lead to more practical interpretation of results, it can be difficult to identify the trends between the wind profile and entrainment. Idealized wind profiles can be more useful for this purpose, and results can be compared to the plethora of past modeling studies using these same idealized environmental profiles. The aforementioned studies only conducted simulations using an environment with

8

either no initial wind or very strong wind shear, preventing any systematic relationships from being found as the vertical wind shear is increased.

1.5 Objectives of this Study

Based upon the open questions revealed by this review of the literature, the primary goals of this study are:

- to directly quantify entrainment into numerically-simulated, developing thunderstorms occurring in environments with different amounts of vertical wind shear, in order to evaluate if the P-type circulation does indeed entrain more air into the cloud than a symmetric toroidal circulation;

- to relate this entrainment to dilution effects within the developing storms to understand their role in modulating cloud top height and the amount of condensate in the core (including effects on precipitation development); and

- to identify any systematic relationships among vertical wind shear and entrainment and its effects.

While this study is limited to the early ("developing") stage of supercell thunderstorms, i.e., before a rotating updraft alters the storm dynamics, it seeks to improve understanding of the influence of entrainment and dilution on storm development, particularly with regard to cloud top ascent, and the reduction of cloud condensate and buoyancy.

Chapter 2 discusses the methods used, which include high-resolution idealized model simulations of developing supercell thunderstorms growing in environments with different vertical wind profiles. Entrainment is directly calculated into the core of the simulated developing storms using the method of Dawe and Austen (2011), and new approaches for

evaluating dilution are developed. Chapter 3 presents the results from these simulations, including calculated entrainment and dilution values. Chapter 4 presents conclusions and discusses possibilities for future work.

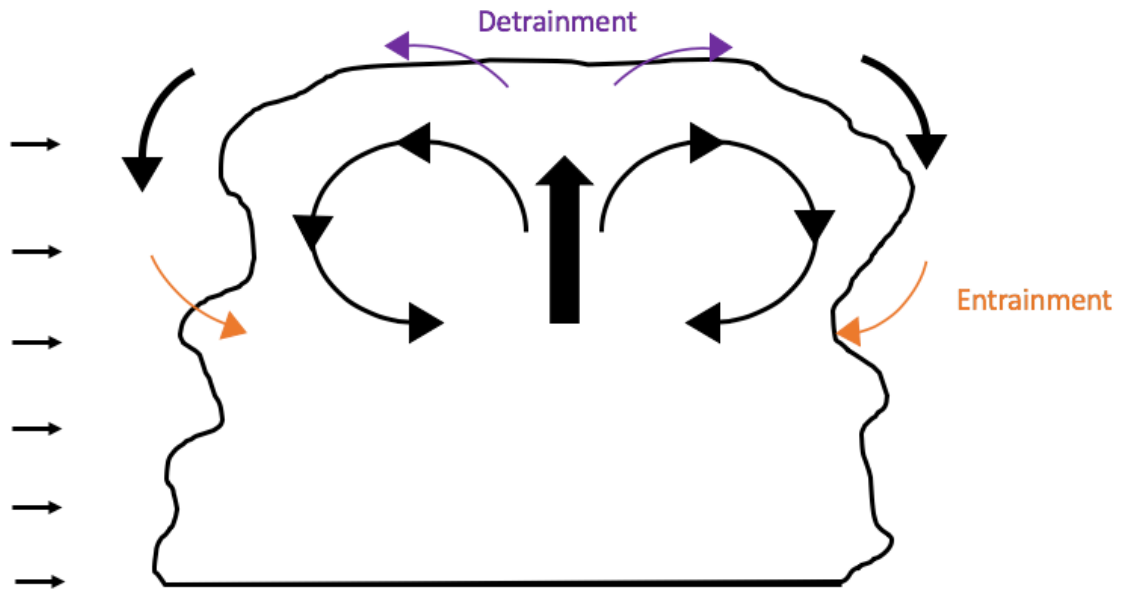**1.6 Figures**

Figure 1: Conceptual diagram of a toroidal circulation for a thermal ascending within a cumulus

cloud in an environment with no vertical wind shear, as indicated by the vectors on the left.
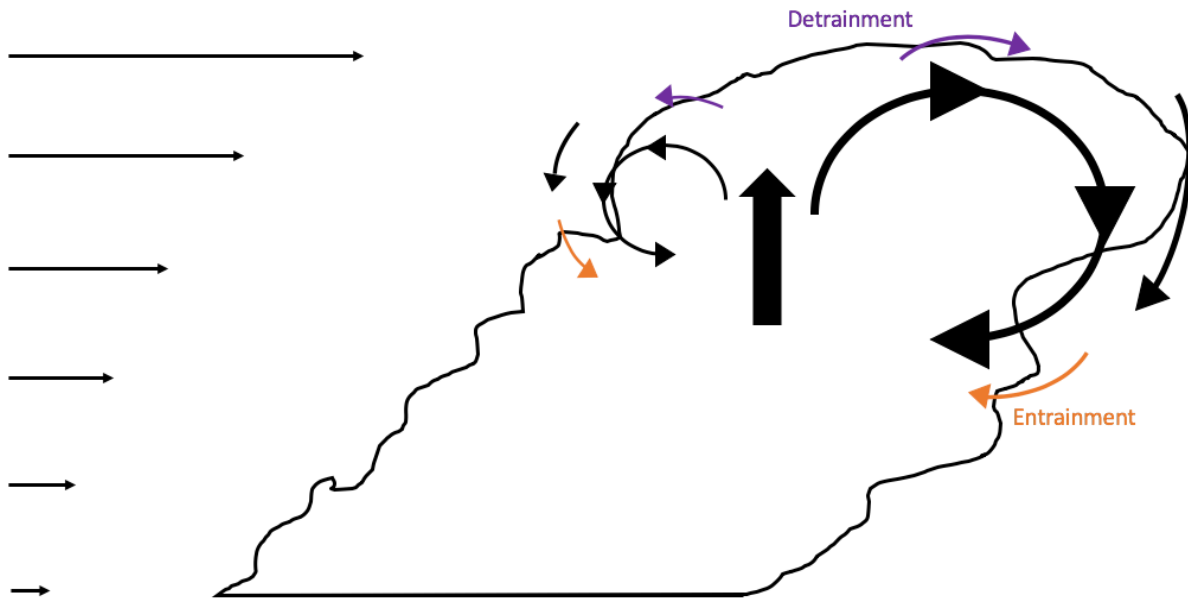
Figure 2: Conceptual diagram of a toroidal circulation for a thermal ascending within a cumulus

cloud in a strongly sheared environment, as indicated by the vectors on the left.

CHAPTER 2: METHODS

2.1 Model Description and Initiation Technique

All simulations were produced using Cloud Model 1 (CM1; Bryan and Fritsch 2002)

version 19.6. CM1 is a nonhydrostatic, 3D, idealized, cloud-resolving numerical model used for

simulating mesoscale processes in the atmosphere. Calculations are made on an Arakawa C-grid,

which has scalar values located at grid box centers and velocity components located at the center

of grid box faces. Derivatives are approximated using finite differences, and this arrangement

allows for greater precision in these calculations than one with the scalars collocated with the

vector components. CM1 solves the fully-compressible form of the Navier-Stokes equations that

includes the Coriolis force; it calculates the three components of velocity, non-dimensional

pressure, potential temperature, and sub-grid scale turbulent kinetic energy. Advection of scalar

quantities and momentum is calculated by integrating sixth-order spatial derivatives in time.

All simulations used for this study had a similar thermodynamic environment, based on

that used by Weisman and Klemp (1982), with a mixed layer water vapor mixing ratio of 14 g

kg^{-1} (Figure 3). The initial state was in hydrostatic balance and horizontally-homogeneous, with

the exception of random temperature perturbations up to +/- 0.05 K inserted at the start of the

simulations. These random perturbations were included to introduce turbulence more quickly

into the simulation[1]. The environmental wind and horizontal domain size were varied as

described in Section 2.2; the height of the domain was always 20 km. Rayleigh damping was

used above 17 km altitude to prevent wave reflection off the top of the domain. The top and

---

[1] Simulations were produced with different values of these random temperature perturbations, as well as with no
random perturbations. With no random perturbations, there is much less turbulence initially, and the initial thermals
require more time to develop. With random perturbations too large, thermals can be produced just by regions with
relatively warm random temperature perturbations, apart from the Gaussian heating that initiates the storm as
described by Eqn 2.1.

bottom boundary conditions were free-slip, and the east, west, north and south boundary

conditions were open (radiative). The NSSL microphysics scheme used here is a two-moment

scheme which calculates the number concentration and mass mixing ratios for 6 hydrometeor

classes: cloud water, cloud ice, rain, snow, graupel, and hail (Mansell et al. 2010).

The grid spacing used for every simulation was 100 m. The effect of this grid spacing

was tested (Appendix A) to determine the adequacy of this resolution for performing the direct

entrainment calculations described in the next section. This grid-spacing required a time step of

0.2 s in order to meet the CFL criterion. Acoustic waves were represented by splitting the 0.2

second time step into 10 smaller steps (as in Klemp and Wilhelmson 1978). Sub-grid scale

turbulence was represented by a 1.5 order turbulence scheme (Deardorf 1980). Table 1 lists some

parameters and settings used in each simulation.

To perturb the hydrostatic base state and initiate convection, a Gaussian surface heat flux

(Carpenter et al. 1998) was utilized. This heat flux was strongest at the surface and decreased in

magnitude exponentially in the radial and vertical directions. It can be expressed mathematically

as

$$H(t) = H_g(t) * e^{-\left(\frac{(x-x_0)^2}{\sigma^2} + \frac{(y-y_0)^2}{\sigma^2}\right)} * e^{-\left(\frac{z}{\alpha}\right)}. \tag{2.1}$$

where $H(t)$, refers to the magnitude of the heat flux (in W m^{-2}) at point (x, y, z) and time t. $H_g(t)$

is the maximum magnitude of the heat flux (in W m^{-2}) at time t, located at $(x_0, y_0, 0)$. The

horizontal width and height (in m) of the Gaussian are given by σ and α, having respective

values of 5000 m and 1500 m. H_g linearly increased in time from 0 W m^{-2} at the start of the

simulation until reaching its maximum value at 5 minutes. The peak value of H_g varied by

simulation (Table 2), which will be discussed in Section 2.2. The heating was maintained at this amplitude for 24 minutes, then linearly decreased to 0 W m^{-2} over one minute, for a total of 30 minutes of active heating. This technique enabled the formation of buoyant thermals which produced the developing thunderstorm.

2.2 Initial Conditions of Simulations, and Determination of Analysis Period

   Environmental wind profiles were varied for the six different simulations (Figs. 4 and 5) to understand the effects of wind shear upon entrainment and dilution. The control simulation, BASE, was initialized with the original quarter-circle wind profile as used by Weisman and Klemp (1982) to produce a supercell, and other simulations were variations of this wind profile. A hodograph showing the wind profiles of BASE and SPD100, which have the same wind speed at all altitudes but different wind directions, is shown in Figure 4. For 'speed shear' simulations (SPD050, SPD100, SPD125), the original wind was modified such that the wind direction was constant and due westerly at all heights, with the magnitudes of the wind vectors being 50%, 100%, or 125% of the original values, for the SPD050 SPD100, and SPD125 simulations, respectively (Fig. 5). The CONST run was initialized with a wind profile matching SPD100 up to 850 m, but with constant westerly winds of 5 m s^{-1} above 850 m (Fig. 5). The NOWND run was initialized with no (zero) environmental wind. The 0-6 km bulk wind shear values were 0, 5, 15.9, 31.8, 31.8, and 39.7 m s^{-1}, for the NOWND, CONST, SPD050, BASE, SPD100 and SPD125 runs, respectively.

   For these different simulations, domain size and cloud forcing also differed. The size of the domain varied because the propagation speed of the clouds varied according to the environmental winds, requiring a larger domain for stronger winds as the clouds traveled farther

during the integration time. Additionally, the strength of the forcing used to initiate convection (Table 2) varied by simulation, as required to achieve similar cloud top heights.

For the analysis of entrainment and dilution, it was necessary to define a time period as the "developing stage" of the simulations. In the simulations with initial wind profiles favoring supercell formation, storm-splitting occurred, which produced two counter-rotating updrafts. The storm-splitting would have resulted in two separate, large cloud cores which at times were marginally connected. Splitting complicates interpretation of the direct entrainment calculations, as the changing shape of the cloud core(s), and their nonlinear dynamical interactions, affects the results of the entrainment diagnostic algorithm. Thus, for the BASE, SPD050, SPD100, and SPD125 runs, a modified Pearson correlation (MPC, Naylor et al. 2012) was used to detect a rotating updraft over 3 km by 3 km horizontal subsets of grid points, and objectively determine the end of the "developing stage". MPC is defined as

$$MPC = \frac{w' \zeta'}{\sigma_w \sigma_\zeta} \tag{2.2}$$

where w' is the deviation from the subset mean vertical velocity, ζ' is the deviation from the subset mean vertical component of vorticity, and σ is the standard deviation of each as denoted by the subscript. The MPC was then averaged between 2 km and 5 km altitude over the horizontal subsets of grid points. Once any subset had an MPC value exceeding 0.3, a rotating updraft was deemed present, and the developing stage was over for the purpose of analysis in this study. Rotation was generally found when the cloud top height was near 6500 m. For NOWND and CONST, where storm-splitting and rotation did not occur, the developing stage was thus limited to the period at which cloud top heights did not exceed 6500 m.

16

2.3. Direct Entrainment Calculation

Entrainment was calculated using the direct method of Dawe and Austin (2011) in all simulations. This method involves calculating the air mass flux into a three-dimensional cloud core, where the cloud core was defined[2] using the set of points in the model domain where the vertical velocity exceeded 2 m s^{-1} and the total mixing ratio of cloud water, cloud ice, rain, and graupel ($q_c + q_i + q_r + q_g$) exceeded 0.5 g kg^{-1} (Snow and hail mass were negligible over the developing stage of the simulations). Grid boxes were sub-divided into 48 tetrahedrons to better resolve the cloud core surface on a sub-grid scale. Mathematically, Dawe and Austin (2011) defined entrainment and detrainment as

$$e - d = \int_C \rho(\boldsymbol{u}_i - \boldsymbol{u}) \cdot d\boldsymbol{C} \qquad (2.3)$$

where e and d are the local entrainment and detrainment rates (in kg m^{-3} s^{-1}), ρ is the moist air density, $\boldsymbol{u}$ is the velocity vector of the air, $\boldsymbol{u}_i$ is the velocity vector of the core surface (both velocities in m s^{-1}), and $\boldsymbol{C}$ is the vector normal to the cloud core surface area (in m^2). Where $e - d$ is positive, net entrainment occurs locally, and where $e - d$ is negative, net detrainment occurs locally (Romps 2010). This equation is difficult to express in a model framework, so Dawe and Austin (2011) performed the following derivation to apply to the model output.

First, the Leibnitz integral rule is used to decompose the time derivative of cloud core mass into the following terms:

---

[2] Experimentation using different threshold values of the cloud core yielded similar entrainment values, but lower values of these thresholds increased dilution values. Both constant thresholds and thresholds which varied with time (e.g. using percentiles of the total hydrometeor mixing ratio) were tested.

$$\frac{d}{dt} \int_{V(t)} \rho dV = \int_{V(t)} \frac{\partial \rho}{\partial t} dV + \int_{C(t)} \rho \boldsymbol{u}_i \cdot d\boldsymbol{C} + \int_{W(t)} \rho \boldsymbol{u}_i \cdot d\boldsymbol{W} \qquad (2.4)$$

where $\boldsymbol{W}$ is the vector oriented normal to the grid box walls and has a magnitude equal to the grid box face area occupied by the cloud core volume (units of m^2), and all other variables are as in Eqn 2.3. For a single time step, $\frac{\partial \rho}{\partial t}$ is typically small and can be neglected, eliminating the first term on the right hand side. Also, $\boldsymbol{u}_i$ is zero at the grid box face because the grid box faces are stationary, eliminating the third term. Therefore, (2.4) reduces to

$$\frac{d}{dt} \int_{V(t)} \rho dV = \int_{C(t)} \rho \boldsymbol{u}_i \cdot d\boldsymbol{C}. \qquad (2.5)$$

Substituting Eq. (2.5) into Eq. (2.3) yields:

$$e - d = \rho \frac{dV}{dt} - \int_C \rho \boldsymbol{u} \cdot d\boldsymbol{C}. \qquad (2.6)$$

The first term on the right-hand side of Eq. (2.6) describes an increase of the mass flux into the cloud core when the volume of the cloud core expands. The second term describes a decrease in the inward mass flux when air flows outward across the cloud core surface. This means that changes in the cloud core volume only by advection of the core surface will not result in entrainment or detrainment.

Gauss' divergence theorem applied to the mass flux $\rho \boldsymbol{u}$ through the cloud core surface area $\boldsymbol{C}$ results in:

$$\int_C \nabla \cdot (\rho \boldsymbol{u}) dV = \int_C \rho \boldsymbol{u} \cdot d\boldsymbol{C} + \int_W \rho \boldsymbol{u} \cdot d\boldsymbol{W}. \tag{2.7}$$

Since $\frac{\partial \rho}{\partial t}$ is negligible, the mass continuity equation implies $\nabla \cdot (\rho \boldsymbol{u}) = 0$, and Eq. (2.7) reduces

to:

$$\int_C \rho \boldsymbol{u} \cdot d\boldsymbol{C} = -\int_W \rho \boldsymbol{u} \cdot d\boldsymbol{W}. \tag{2.8}$$

Substituting Eq. (2.8) into Eq. (2.6) results in:

$$e - d = \rho \frac{dV}{dt} + \int_W \rho \boldsymbol{u} \cdot d\boldsymbol{W}. \tag{2.9}$$

In Eq. (2.9), the left-hand side again represents local entrainment and detrainment rates. The first

term on the RHS represents core expansion and contraction, and the second term represents the

component of the flow normal to the cloud core surface. Where the second term is positive, the

flow is inward relative to the core, and this term will contribute to entrainment, and where it is

negative, the flow is outward relative to the core, contributing to detrainment.

Calculations of entrainment using Eqn. 2.9 can be made using either the total winds, or

perturbation winds (i.e. the deviation of the winds from the environmental state). The

perturbation winds were generally used in order to more fairly compare the effects of the internal

cloud motions upon entrainment in the simulations with different environmental winds (see

Section 2.2). Furthermore, this method allows for the visualization of overturning thermal

circulations to be distinguished more clearly from any entrainment resulting from the

impingement of the environmental winds upon the cloud.

Output was written from the model simulations every 6 seconds in order for the direct entrainment calculations to adequately include the turbulent motions occurring in and around the cloud core, as well as the rapid changes in the core surface. One-minute averages of the entrainment rate normalized by surface area at each altitude (E_{SA}, in kg m^{-2} s^{-1}) are designed to encompass the full sequence of the overturning circulations.

2.4. Integrated Entrainment

Comparing individual profiles of entrainment rate (i.e. plots of E_{SA} against height for a single one-minute period) can be useful for understanding the particular turbulent eddies contributing to entrainment in different simulations. However, to more easily compare the broader effects of entrainment on simulated storms which might develop very differently (see Section 2.2), it is useful to obtain single values of entrainment for the entire cloud depth.

In order to calculate total-core entrainment rate, the following equation was used:

$$E_{SA,t} = \frac{\sum_{z=(2000\ m+dz)}^{CT}(E_{SA,z}*SA_z)}{\sum_{z=(2000\ m+dz)}^{CT}(SA_z)} \qquad (2.10)$$

where $E_{SA,t}$ refers to the *average entrainment rate* across the cloud core depth, normalized by the core surface area, in units of kg m^{-2} s^{-1}, at some time t. The value $E_{SA,z}$ is the entrainment rate normalized by the core surface area at that time for a single height level z (in kg m^{-2} s^{-1}). The value SA_z is the surface area of the cloud core at height level z (in m^2). The summation over altitude was conducted starting at 2100 m, up to the cloud top height CT. Heights below 2100 m were excluded because the entrainment diagnostic algorithm considers updraft entering the cloud

core from below to be 'entrainment,' as it cannot distinguish entrainment from the updraft mass flux at the core base. These cloud core average values also were obtained every 60 s.

It is also useful to calculate the cumulative entrained mass throughout the storm development. This was first done while maintaining the adjustment for core surface area using the following equation:

$$E_{SA,total} = \sum_{t=t_0}^{t_1} (E_{SA,t} * 60 \ s). \tag{2.11}$$

Here, $E_{SA,total}$ is the *cumulative entrained mass per core surface area*, in units of kg m^{-2}. The quantity t_0 refers to the first appearance of the cloud core, and t_1 refers to the end of the developing stage (Table 2). In effect, Eq. (2.12) converts each one-minute average $E_{SA,t}$ value into a surface area-normalized entrained mass for the respective one-minute period, then these values are summed across the developing stage.

Obtaining the *total cumulative entrained mass* can be done starting from the original $E_{SA,z}$ values produced by the direct entrainment algorithm using

$$E_{total} = \sum_{t=t_0}^{t_1} 60 \ s * \sum_{z=(2000m+dz)}^{CT} (E_{SA,z} * SA_z) \tag{2.13}$$

where E_{total} is the cumulative entrained mass (in kg), and all other variables are as described previously. Equation (2.12) effectively removes the surface area adjustment for each one-minute averaging period while summing across the cloud depth to calculate an entrainment rate in kg s^{-1}, then this is multiplied by 60 s and summed across the developing stage to calculate the cumulative entrained mass into the cloud core.

21

2.5. Evaluation of Dilution

Dilution was primarily evaluated with regard to reduction in LWC. This involved both obtaining and manipulating evaporation and sublimation rates directly from the model output, as well as tracking values of the hydrometeor mixing ratios within and outside the core. In both cases, trends with entrainment rates were studied both qualitatively and quantitatively.

The following rates of evaporation or sublimation were specifically output from the model for this project (all in g kg^{-1} s^{-1}):

1. Evaporation rate of cloud water ($\frac{dq_c}{dt}_{evap}$)

2. Sublimation rate of cloud ice ($\frac{dq_i}{dt}_{sub}$)

3. Total evaporation and sublimation rate for larger hydrometeors (rain, graupel, hail, and snow; $\frac{dq_{precip}}{dt}_{evap}$).

Relevant statistics include the maximum rates of evaporation and/or sublimation, both within the core and throughout the entire domain. Additionally, the total evaporated and/or sublimated mass (in grams) was calculated from these rates with the following equations:

$$cw_{evap} = \sum_{i=1}^{n} \frac{dq_c}{dt}_{evap} * \rho_d * \Delta^3 * \Delta t \qquad (2.13)$$

$$ci_{sub} = \sum_{i=1}^{n} \frac{dq_i}{dt}_{evap} * \rho_d * \Delta^3 * \Delta t \qquad (2.14)$$

$$precip_{evap} = \sum_{i=1}^{n} \frac{dq_{precip}}{dt}_{evap} * \rho_d * \Delta^3 * \Delta t \qquad (2.15)$$

where cw_{evap}, ci_{sub}, and $precip_{evap}$ refer to the evaporated cloud water mass, sublimated cloud ice mass, and evaporated and sublimated mass of the larger hydrometeors, respectively, ρ_d is the dry air density, Δ is the model grid-spacing (and thus Δ^3 is the volume of a grid cell; Δ is 100 m for all simulations), Δt is the time between model output (6 s in all simulations), and n is the number of grid points across which the sum is being calculated (all of the grid points for a given model height level). These values were averaged across one-minute intervals to correspond to the same averaging period used in entrainment calculations. Not only evaporation and sublimation occurring inside the core, but also outside the cloud core, are relevant because entrainment can influence where the core surface lies (i.e. dilution related to an entrainment event can cause some points to transition from inside the core to outside the core).

Cloud water and rain mixing ratios (q_c and q_r) within the core were also used to diagnose dilution, as well as values of buoyancy. Median values of the sum $q_c + q_r$ within the core, at each vertical level, were found, and the change of this median was compared to entrainment calculated at the same vertical level. Liquid hydrometeors were primarily considered, rather than ice hydrometeors, because ice did not form in substantial quantities in any simulation until after the end of the analysis period.

In addition to evaluating changes in condensate mass, changes in buoyancy were also evaluated. Buoyancy relative to the initial model state was output from the model. Profiles against altitude of both the median and maximum value of the buoyancy acceleration within the cloud core were obtained in order to evaluate dilution by entrainment events. It was important to be cautious when evaluating reductions in buoyancy, as it could be caused by either dilution due to entrainment, or by the presence of a large total hydrometeor mass.

2.5.1 Precipitation Efficiency

In order to evaluate the development of precipitation in each simulation, and to investigate how the rate of precipitation development varies with shear, entrainment microphysical precipitation efficiency (EMPE) was calculated throughout the developing stage of each simulation. EMPE is defined by the following expression:

$$EMPE = \frac{m_r + m_s + m_g + m_h}{m_c + m_i} \qquad (2.16)$$

where m_x refers to the total mass of hydrometeor class x within the cloud core, and the subscripts $r, s, g, h, c,$ and i refer to rain, snow, graupel, hail, cloud water, and cloud ice, respectively. In other words, EMPE is the ratio of the mass of larger ("precipitation") hydrometeors to the mass of smaller ("condensate") hydrometeors within the cloud core. Thus, EMPE allows for the efficiency of precipitation formation in the cloud core to be compared across simulations, and differences in EMPE might be related to entrainment and dilution.

2.6. Tables and Figures

Table 1. List of model parameters used in all simulations for this study.

Model Aspect	Scheme/Setting
Microphysical parametrization	NSSL Two-Moment (Mansell et al. 2010)
Horizontal and vertical advection schemes for scalars and vectors	All 6th order
Advection with WENO Scheme	5th order; only scalars; only on final Range-Kutta step
Artificial diffusion	Monotonic version applied to all variables
Subgrid-scale turbulence scheme	TKE (Deardorff 1980)
Pressure solver	Klemp-Wilhelmson time-splitting, fully-explicit
Large-scale pressure gradient acceleration	Applied to u and v based on geostrophic balance using base-state wind profiles
Lateral boundary conditions	Open-radiative
Lower and upper boundary conditions	Free-slip

Table 2. Differences in characteristics of the simulations used for this study.

| Simulation Name	Wind Profile	Maximum Forcing (H_g; in W m^{-2})	Domain Size ($x * y$; in km)	Developing Stage Start and End Time (min.)
BASE	Weisman and Klemp (1982), quarter-circle hodograph as shown in Fig. 3	500	124 * 124	41.5 – 60.1
NOWND	No environmental wind	250	36 * 36	49.5 – 63.0
CONST	Constant west wind of 5 m s^{-1}	325	80 * 80	56.3 – 71.0
SPD050	Speed shear only, west winds, magnitudes halved from BASE	400	124 * 124	41.0 – 59.5
SPD100	Speed shear only, west winds, magnitudes same as BASE	500	124 * 124	40.1 – 62.9
SPD125	Speed shear only, west winds, BASE magnitudes multiplied by 1.25	600	124 * 124	29.2 – 59.0
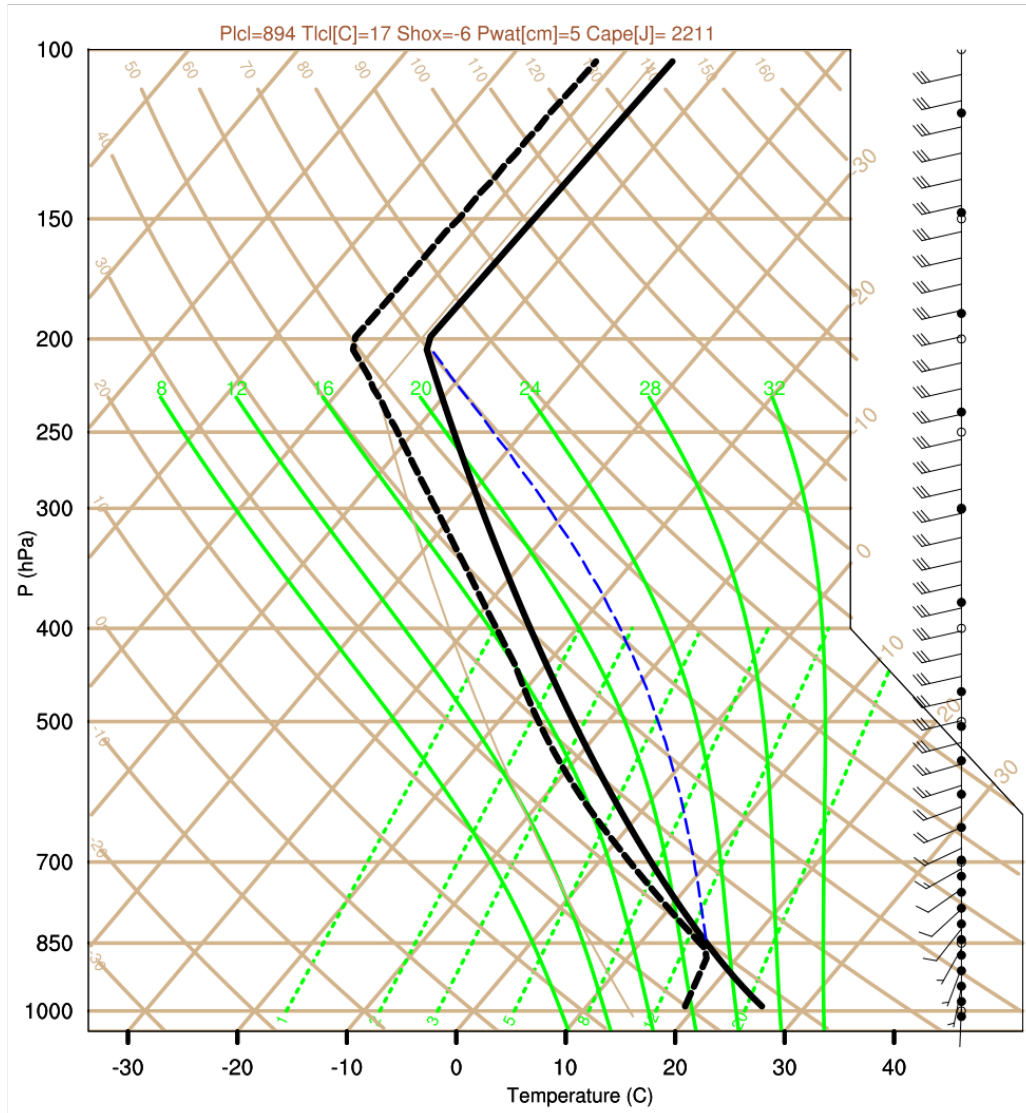
Figure 3. The environmental sounding used for BASE, which has the same thermodynamic profile as all other simulations. Solid and dashed black lines show the environmental temperature and dew point, and dashed blue line shows the temperature of a parcel lifted adiabatically from the surface.
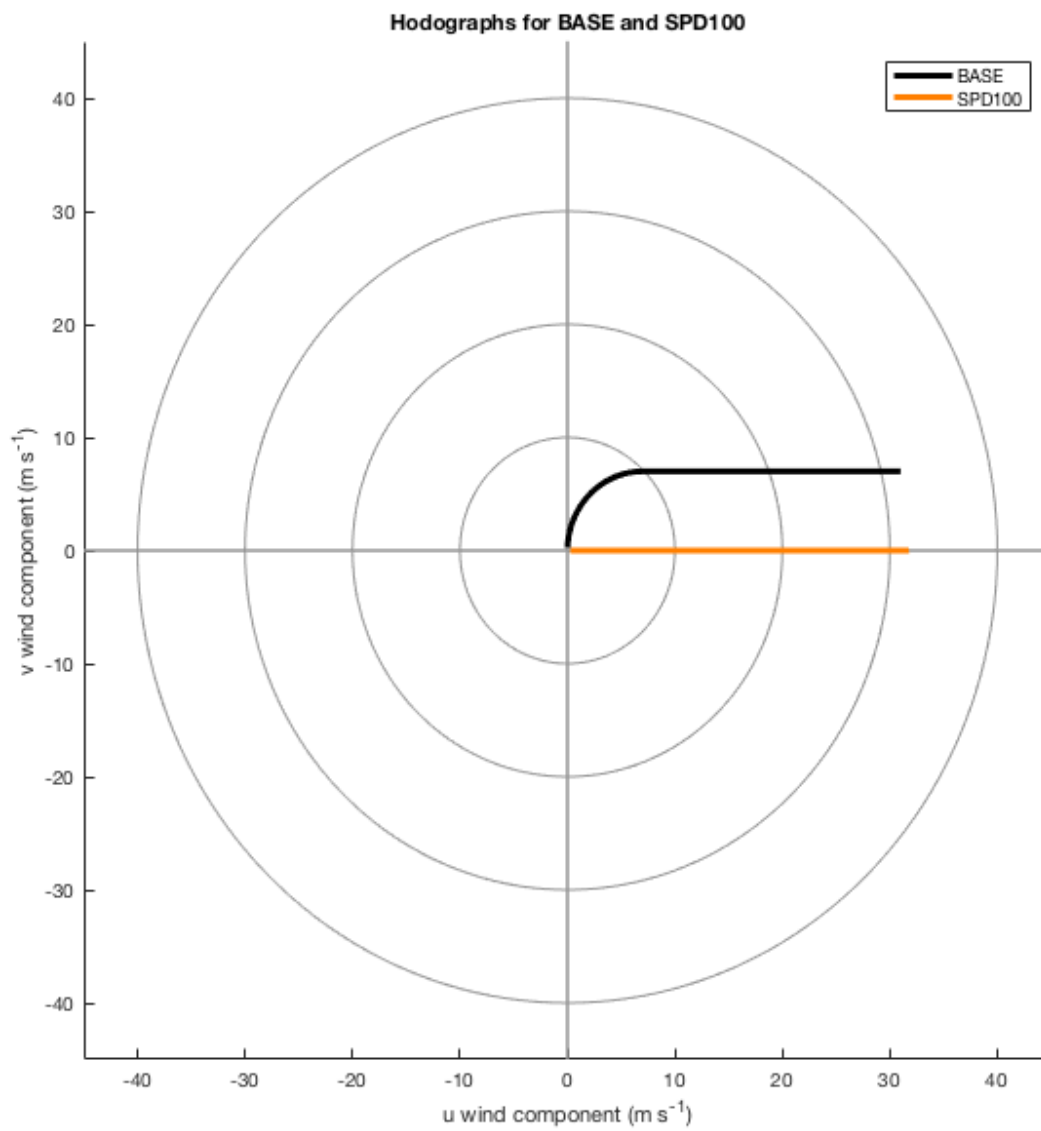
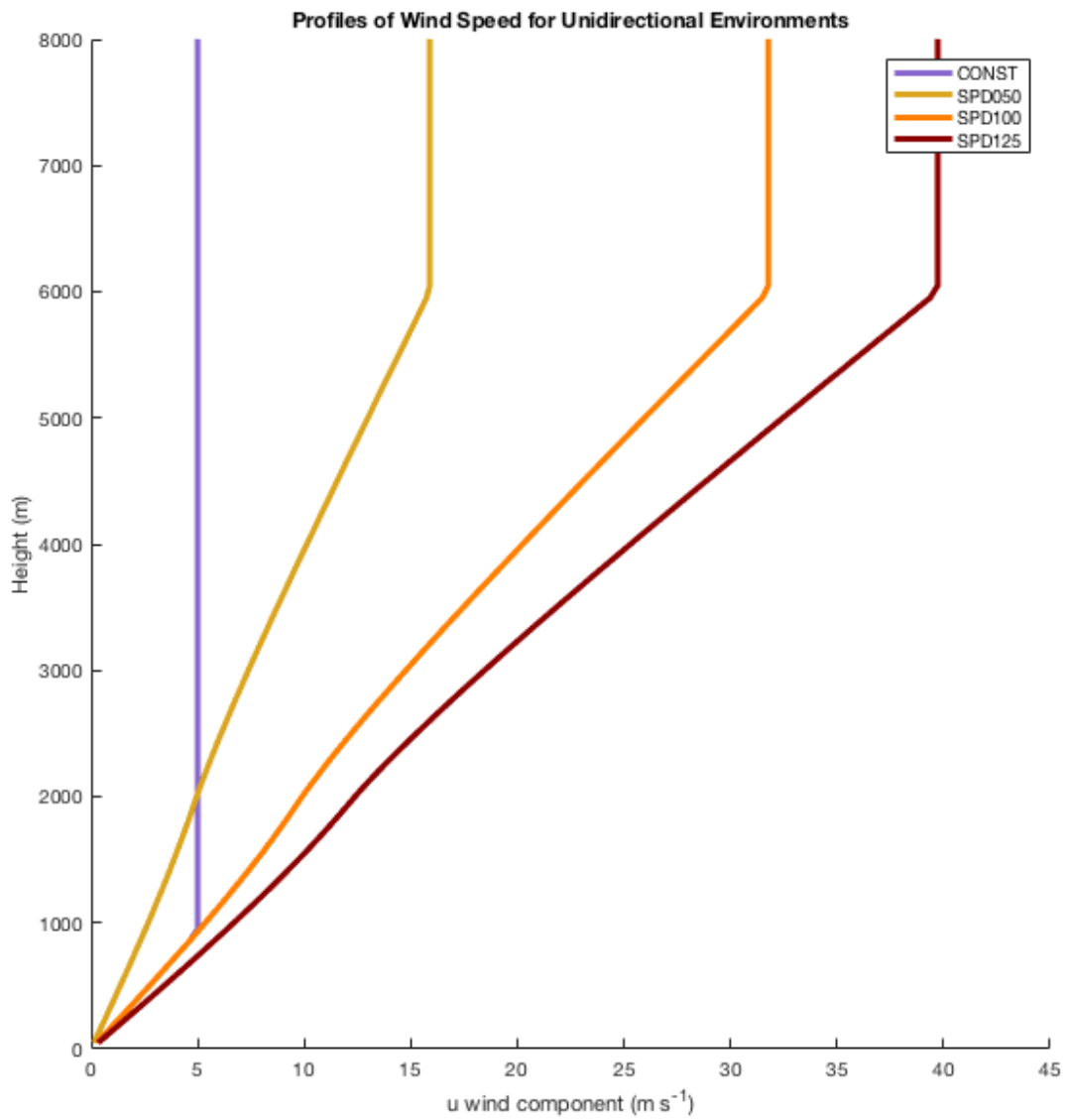Figure 4. Hodograph of wind profiles used in BASE and SPD100.

Figure 5. Vertical profiles of the zonal wind component in CONST, SPD050, SPD100, and SPD125 simulations. Meridional wind component was 0 m s^{-1} at all altitudes for these profiles.

CHAPTER 3: RESULTS

3.1 Overview of Storm Development in All Simulations

In order to better compare entrainment and its effects in different shear environments, it is important to understand first the differences in storm development that occur within those environments. Figure 6 includes time series diagrams of cloud top height and maximum updraft speed for each simulation. Notably, NOWND and CONST had a cloud form much later (after 30 minutes) than the other simulations (clustered around 24 minutes), due to the weaker heating required to initiate convection in the environments without shear (Table 2). All simulations have a cloud top height at or greater than 6 km by the end of their developing stage (end of solid lines). The cloud top ascent rates (Table 3) of NOWND and CONST during the developing stage (each 5.6 m s^{-1}) were greater than all the other simulations. In contrast, the maximum updraft speeds of NOWND and CONST are generally relatively low (Figure 6b), likely again due to the much weaker forcing (often half) required to initiate convection in those simulations. For the simulations with vertical wind shear, the SPD050 run generally had the greatest cloud top ascent rate and maximum updraft speed, followed by SPD125 (Table 3, Figure 6). It is surprising that SPD125 would have greater cloud top ascent rate and maximum updraft speed than BASE or SPD100, given the greater wind shear present. Peters et al. (2019) found that convection deepened at a slower rate in idealized simulations of moist thermals in sheared environments than in un-sheared environments. This discrepancy is likely due to the greater heating used for convective initiation in SPD125, as well as the successive thermals which will be discussed later.

In each simulation except CONST, multiple thermals formed, and merged with each other over time to varying degrees. The random temperature perturbations initialized over the domain led to the formation of thermals at random locations within the region of heating. The

extent of merging thermals was least in NOWND, in which there was no background flow acting

on the thermals. The main cloud core was the one instance in NOWND where two separate

thermals happened to occur close enough to merge to form a single cloud core (Figure 7). The

CONST run was prevented from having multiple thermals because air parcels heated by the

Gaussian heat flux were advected away from the location of the forcing, having the strongest

horizontal wind at the 1500 m altitude (Figure 5) where the top of the Gaussian heating function

occurred. In the simulations with vertical wind shear (BASE, SPD050, SPD100, SPD125),

multiple thermals formed and generally combined over time to produce a larger cloud. For

example, vertical cross-sections of buoyancy for the SPD100 run (Figure 8) initially show two

separate regions of positive buoyancy (i.e. thermals), each part of a distinct cloud core,

combining into one cloud core and region of positive buoyancy within 6 minutes. While the

advection of parcels heated by the Gaussian heat flux would also have occurred in the

simulations having vertical wind shear, the heat flux was stronger in these cases, and mechanical

turbulence introduced by the vertical wind shear may have also promoted the formation of more

thermals than in the no-shear runs.

In each simulation with vertical wind shear, thermals tended to ascend and tilt up-shear,

and move more slowly down-shear than the environmental winds. Malkus (1949) described the

up-shear tilt of ascending parcels as resulting from the difference in momentum at their source

height (i.e., below the cloud base) versus at higher altitudes. This phenomenon is illustrated for

SPD125 in Figure 9. At 52 minutes, a new thermal emerged in the buoyancy field (solid outlined

circle near x = 11,300 m and z = 2200 m in Figure 9a), with an older thermal to the west (dashed

circle in Figure 9a). Two minutes later, the newer thermal was located at x = 12,600 m and z =

3000 m (solid outlined circle in Figure 9c). This implies an eastward motion of roughly 11 m s^{-1},

slower than the environmental westerly wind that exceeded 13 m s^{-1} in the layer through which it ascended. This resistance to the background wind is also apparent in the surrounding perturbation wind field, which was mostly easterly. By 55 minutes, the newer thermal merged with the older thermal (Figure 9d). Thus, the vertical wind shear present in BASE, SPD050, SPD100, and SPD125 facilitated the interaction of older and newer thermals that was absent in the simulations without vertical wind shear. It will be shown that this interaction makes the effects of entrainment a little more difficult to diagnose, and indeed helps to mitigate its effects upon the developing storm.

During the late developing stage in BASE, SPD050, SPD100, and SPD125, interactions between thermals led to strengthening of the cloud, as evidenced by the increasing updraft speeds for these cases as compared to the NOWND and CONST cases (Figure 6b). In Figure 10, vertical cross sections from SPD050 were used to illustrate this phenomenon. At 53 minutes, three separate buoyancy maxima were present in the cross-section, representing three separate thermals (Figure 10a). Over the following 6 minutes, these thermals merged and interacted with one another, producing a broader region of high buoyancy, and thus a faster updraft (Figure 6b). During this time period, the height of the top of the cloud core in this cross-section increased by over 2000 m (Figure 10b-d) and is seen as an increase in ascent rate in Figure 6a. The rapid storm strengthening in SPD050 during the period 53 minutes to 59 minutes was also apparent in the time series of maximum updraft speed (Figure 6b). These results are consistent with the results of successive thermals described, for example, by Scorer and Ludlam (1953), and more recently investigated by Moser and Lasher-Trapp (2017).

In the simulations with environmental wind shear, counter-rotating vortices did begin to form just before rotating updrafts were detected according to the MPC method described in

Section 2.2. Figure 11 shows horizontal cross-sections (at 3450 m altitude) of vertical velocity

with perturbation wind vectors at the end of the developing stage (i.e. the time when a rotating

updraft was detected) for BASE, SPD050, SPD100, and SPD125. In each case, there was a

region of counterclockwise rotation on the south (or southeast) side of the main updraft. It was

least apparent in SPD050 (Figure 11b). There was little evidence that the storm-splitting process

actually began by the time rotation was detected in these cases. There was only one 'primary'

cloud core in each of these cross-sections, larger than any other cloud cores. Once splitting

begins, two cloud cores of similar size are expected. Thus, the method of rotation detection did

effectively define the end of the developing stage prior to storm-splitting as intended, but there

may have been further storm development prior to splitting which will not be analyzed here.

3.2 Direct Entrainment Calculations for All Simulations

For an overview of entrainment rates in each simulation, time-height plots of E_{SA}

calculated using the perturbation wind are shown in Figure 12. When interpreting the plots in this

figure, values below 2000 m (near cloud base) can be largely disregarded, as they represent

updraft entering the cloud core from below. Clearly greater entrainment rates were present in

simulations with greater environmental wind shear, as the largest E_{SA} value in SPD125 was

roughly 6 kg m^{-2} s^{-1} (Figure 12f), while the largest E_{SA} value in NOWND was roughly one sixth

of this value (Figure 12a). The E_{SA} values in CONST were also generally larger than the E_{SA}

values in NOWND (Figure 12a-b), implying that increases in wind magnitude, even for an initial

wind profile with no vertical wind shear above cloud base, can lead to increases in the amount of

entrained air during the developing stage. This is also despite the fact that the maximum updraft

speeds in NOWND were greater than those in CONST for most of their respective developing

32

stages (Figure 6b). It is more difficult to find systematic differences in E_{SA} for SPD100 and

BASE (Figure 12d-e), which had the same initial wind magnitude at all vertical levels, but with

different wind directions. This implies that the low-level turning in the hodograph in BASE does

not lead to different entrainment values than the straight hodograph in SPD100 for the

developing stage. However, all of the curvature in the hodograph was below the cloud base

altitude, so other hodographs with curvature extending to greater altitudes might differ from this

result.

There was also a common trend of increasing entrainment rates with time for each of the

simulations with initial vertical wind shear (Figure 12c-f). This resulted in the peak one-minute

average entrainment rate for each of these simulations, except SPD100, occurring in the final

minute of the developing stage. In some simulations (particularly SPD050 and BASE; Figs. 12c

and e), multiple "streaks" of relatively high entrainment can be seen over the depth of the plotted

values. These correspond to the overturning eddies near the tops of multiple ascending thermals,

discussed in Section 3.1. The trends of increasing entrainment rates with time and with vertical

wind shear both agree with the results of Engelsen (2018).

The trends discussed above were largely true regardless of whether E_{SA} was calculated

using the total winds or the perturbation winds. Figure 13 again shows time-height plots of E_{SA}

for each simulation, but E_{SA} was calculated using the total wind for these plots. The entrainment

rates were still generally greater with stronger initial shear (Figure 13d-f) than with weak or no

initial shear (Figure 13a-c) when calculated using the total winds. The trend of increasing

entrainment rates with time (i.e. storm growth), particularly for the stronger shear simulations,

was still present when E_{SA} was calculated using the total winds. The primary difference in the

resulting entrainment rates from the two methods of calculation was the magnitudes of E_{SA} at

mid- and upper-levels of the cloud; there were greater values of E_{SA} when the perturbation winds were used for calculations. For example, the greatest one minute-averaged E_{SA} values in BASE were roughly 5.2 kg m^{-2} s^{-1} when calculated using the perturbation winds, and 3.7 kg m^{-2} s^{-1} when calculated using the total winds (Figure 12e, Figure 13e). The higher entrainment rates when calculated using the perturbation winds can be explained by both the mid-level storm-relative inflow and the P-type circulation, both of which cause more entrainment on the down-shear side. These features are both masked by the relatively stronger background flow, as illustrated in vertical cross-sections such as that shown in Figure 14, and thus are not recognized as entrainment by the algorithm when using the total winds. In Figure 14a, there was inflow on the east (i.e. downwind) side of the cloud core between 2 and 3 km altitude apparent in the perturbation wind field, and above 3 km altitude, the overturning P-type circulation was entraining air into the cloud core (i.e. the flow is directed from outside to inside the cloud core). When this same cross-section is plotted with the total wind (Figure 14b), the flow appears to be directed from inside to outside of the cloud core. There was still entrainment occurring above 3 km altitude because of the motion of the cloud relative to the total flow (i.e. the cloud core boundary was shifting faster than the local total wind), but less, as the storm-relative inflow and P-circulation were partially cancelled by the background wind. This is shown using the storm-relative wind, which was again directed from outside the core to inside the core (Figure 14c). [The storm-relative wind was calculated for Figure 14c by subtracting the approximate eastward storm motion (10.8 m s^{-1} at the cloud base) between 62 and 63 minutes from the total zonal wind.]

3.2.1 Integrated Entrainment for All Simulations

To better quantify the differences in directly-calculated entrainment across simulations with different wind shear profiles, the integrated entrainment values described in Section 2.4 ($E_{SA,t}$, $E_{SA,total}$, and E_{total}), calculated using the perturbation winds, are plotted against time for each simulation in Figure 15. As the time at which a cloud core formed varied by simulation, the beginning point of each curve for these integrated entrainment values varies by simulation as well. It can be seen that SPD125, SPD100, and BASE had the highest entrainment rates normalized by the core surface area (Figure 15a). SPD125 achieved the highest entrainment rate averaged across the cloud depth (3.85 kg m^{-2} s^{-1} at 59 minutes), but its total entrained mass, whether or not it was adjusted for the core surface area, was lower than SPD100 (found by comparing the values at the end of the curves in Figs. 15 b and c). However, the greater total entrainment in SPD100 was due to the longer time period (before rotation was detected) in which entrainment could occur. In other words, the time period between cloud formation and storm rotation was shorter in the stronger shear simulation (SPD125), and entrainment therefore had less time to act upon the cloud during the defined developing stage. In comparing the non-sheared cases, their entrainment rates and cumulative entrained mass is far less than for the sheared cases, and CONST has a greater peak $E_{SA,t}$ (1.53 kg m^{-2} s^{-1}) than NOWND (0.61 kg m^{-2} s^{-1}). This again implies that the presence of any background flow could lead to enhanced entrainment rates compared to an environment with no background wind, regardless of whether there is vertical shear present in that background flow.

Scatter plots of the maximum $E_{SA,t}$ in the developing stage (Figure 15a), final cumulative $E_{SA,total}$ (Figure 15b), and final cumulative E_{total} (Figure 15c) further illustrate the relationship between vertical wind shear and entrainment. In each case, there is a strong linear relationship (R

35

exceeding 0.94) between either the maximum entrainment rate, or the entrained mass, and the vertical wind shear. While quantitative statistical analysis would require more data points (i.e. more simulations), these scatter plots and correlations demonstrate an underlying systematic relationship between entrainment and the environmental vertical wind shear.

As discussed in Section 3.1, there are many differences in the rate of development of each simulation (Figure 6). Therefore, it is perhaps clearer to plot integrated entrainment for each simulation against cloud top height, to more fairly compare storms which develop at very different rates. The trend in $E_{SA,t}$ becomes clearer when plotted this way: at every cloud top height above 4000 m, simulations which had more initial shear had greater entrainment rates (Figure 16a). In addition, the cumulative entrained mass (i.e. E_{total}) up to every cloud top height above 3500 m was always greater in simulations with more vertical wind shear (Figure 16c). This was true with one exception when normalizing the cumulative mass by core surface area (i.e. $E_{SA,total}$); SPD125 had a lower $E_{SA,total}$ than SPD100 at a cloud top height of 5950 m (Figure 16b), but this again may be an implication of the determination of the end of the developing stage. Overall, there were roughly two orders of magnitude more entrained mass at any given cloud top height in the simulations with vertical wind shear than the simulations without vertical wind shear. There was also clearly more entrainment at a given cloud top height in CONST than in NOWND, except above 6000 m cloud top height, where E_{total} was greater in NOWND than in CONST when compared on a logarithmic scale (Figure 17). This might be explained by the several separate thermals in NOWND providing more core surface area across which entrainment could occur (Figure 7).

Because entrainment by overturning thermal circulations can be related to updraft strength, fractional entrainment was also considered; that is, the entrainment rate normalized by

36

the vertical mass flux, or E_{frac} (in km^{-1}). E_{frac} averaged over the cloud depth (weighted by vertical mass flux and excluding heights below 2050 m associated with the updraft mass flux) is plotted in Figures 18a and b versus time and cloud top height, respectively. In general, the simulations with vertical wind shear had greater fractional entrainment, as shown in Fig. 18c. There was a strong, positive, linear correlation between maximum cloud depth-averaged E_{frac} and 0-6 km bulk wind shear (R = 0.97). The greater E_{frac} values for simulations initialized with vertical wind shear indicate that the trend of more shear leading to more entrainment is not simply a result of the shear simulations having stronger updrafts.

3.2.2 Physical Explanations for Entrainment Trends

Both the entrainment profiles and integrated values of entrainment strongly indicate a positive relationship between vertical wind shear and entrainment; i.e. more environmental shear is associated with more entrainment. Figure 19 shows vertical cross-sections of buoyancy aligned along the shear vector for SPD050, SPD100 and SPD125 at times when the cloud top height was between 5000 m and 6000 m for each respective simulation. For the times plotted, $E_{SA,t}$ was 2.12 kg m^{-2} s^{-1} in SPD050, 3.56 kg m^{-2} s^{-1} in SPD100, and 3.86 kg m^{-2} s^{-1} in SPD125. In other words, the simulations with stronger environmental wind shear had greater entrainment rates, and the difference was especially large between SPD050 and SPD100. This can be explained by both the stronger P-type thermal circulation and the "leaning over" of the cloud with stronger wind shear. The perturbation wind vectors in Figure 19 show stronger overturning on the down-shear side of the cloud leading to entrainment (indicated by wind vectors pointing into the cloud core outline) between 3500 m and 5000 m altitude in SPD100 and SPD125 relative to SPD050. The perturbation wind vectors also indicated stronger storm-relative inflow

in the stronger-shear simulations, in addition to the overall cloud leaning more down-shear rather than being vertically upright in the SPD050 simulation. This down-shear tilt allowed for ascending air over a broader core area to be included as "entrainment" by the algorithm. While it may be uncommon to consider such inflow as "entrainment", the air entering the core here does not have the thermodynamic properties of the air below cloud base, and thus once entering and mixing with the cloud core, would contribute to diluting that cloud base air. Since $E_{SA,z}$ appeared to be greater for the stronger shear simulations throughout almost the entire depth of the cloud (Figure 12), the contributions of both the thermal circulation and the storm-relative inflow seem to be important to differences in calculated entrainment.

3.3 Dilution of Liquid Water Content and Buoyancy

3.3.1 Quantified Evaporation

Evaluating dilution using values of evaporation and sublimation rates output from the model was complicated by the persistent evaporation present along the sides of the cloud at all altitudes, particularly on the upwind side. This will be referred to as "*environmental evaporation*," and was likely due to the environmental winds being incident on the cloud core[3]. Figure 20 shows vertical (x-z) cross-sections of the total evaporation and sublimation rates (i.e. the sum of $\frac{dq_c}{dt}_{evap}$, $\frac{dq_i}{dt}_{sub}$, and $\frac{dq_{precip}}{dt}_{evap}$, as defined in Section 2.5) for NOWND, CONST, and SPD100. The background westerly wind in SPD100 was greater (above 1 km altitude) than that in CONST, and it was greater in CONST than in NOWND throughout the cloud depth (Figure 5). For NOWND (Fig. 20a), the evaporation on the upwind side of the cloud near 5000 m

---

[3] When entrainment calculations are made using the total winds, rather than the perturbation winds, the effects of the environmental winds are included in the calculations. In other words, "environmental evaporation" is only separate from other entrainment effects because entrainment was calculated using the perturbation winds.

appears to be associated with an overturning thermal circulation, and has some of the highest evaporation rates (decreases in condensate; near -10^{-2} g kg^{-1} s^{-1}). Overturning circulations on the upwind/up-shear sides for CONST (Fig. 20b) and SPD100 (Fig. 20c) are not present. Below 5000 m for NOWND, and for both upwind or up-shear sides for CONST and SPD100, evaporation results from the environmental winds impinging on that side of the core, considered entrainment by the algorithm, at comparable rates. Figure 21 shows similar cross-sections, but for SPD050, BASE, and SPD125. Broader regions of larger values of evaporation are associated with the locations of the overturning P-circulations on the down-shear sides, especially prominent in BASE by comparing with the perturbation flow show in Fig. 14a. From both Figures 20 and 21, it is evident that nearly all evaporation and sublimation occurred outside the cloud core, i.e., either acted to remove the edge of the cloud core or to prevent the edge of the core from expanding there. Even the region of substantial evaporation within the core from 3 to 4 km altitude on the down-shear side in BASE was still directly adjacent to the core edge (Figure 21b).

Figure 22 shows a time-height diagram of the maximum total evaporation and sublimation *within* the cloud core, and further illustrates the lack of evaporation or sublimation occurring within it. Only at the latest times in the developing stage do higher evaporation rates occur within the core. The highest rates do not tend to occur at the times and locations of the highest entrainment rates (contoured values). This was surprising, but could be explained by how the cloud core was defined, with a minimum threshold in updraft speed of 2 m s^{-1}. Therefore, since the entire cloud core had updraft by definition, condensation (or deposition) would usually have dominated over evaporation (or sublimation), even when unsaturated environmental air was introduced into the core at higher levels by the storm-relative inflow.

Figure 23 consists of time-height diagrams of the maximum total evaporation and sublimation rate, *anywhere in the model domain*, for each simulation. Here, there appears to be a general trend of greater maximum evaporation rates in the stronger shear simulations. However, as illustrated by the E_{SA} contours included on these plots, the greatest evaporation rates again did not necessarily line up with the greatest entrainment rates. In NOWND and CONST, there was some correspondence between large values of E_{SA} and large values of maximum evaporation rate (Figure 23a-b), but this could simply be due to the relatively small clouds present in those simulations. The trend of increasing maximum evaporation and sublimation rates with increasing shear might also be due to the storm inflow on the down-shear side, and the environmental evaporation discussed previously.

3.3.2 Dilution of Liquid Water Content (LWC)

Where dilution occurs, it was expected that, because smaller drops evaporate more quickly, cloud water should primarily be reduced, rather than rain drops. However, conversion from cloud droplets to rain drops in the model can also lead to less cloud water than expected at a given location, and in the extreme, liquid water can be removed via rain fallout. Therefore, the mixing ratios of cloud water (q_c) and rain (q_r), as well as their sum (q_c+q_r) were all considered here, in order to qualitatively evaluate where the reduction of liquid water was due to entrainment and dilution, and avoid misdiagnosing areas of autoconversion or rain fallout as dilution.

Despite the difficulty in identifying dilution due to entrainment using the evaporation output from the model, it was possible to qualitatively identify regions of dilution within the cloud core, likely due to entrainment, by reduction in LWC. This is illustrated in Figure 24 for

SPD100, in which a thermal produced a large quantity of liquid water between 60 minutes and 62 minutes (due in part to the successive thermal phenomenon discussed previously). This thermal also produced a strong overturning P-type circulation on its down-shear side, and this led to entrainment corresponding to a region within the cloud core of reduced $q_c + q_r$ between 4000 m and 4500 m altitude (Figure 24c). Similar regions of relatively low $q_c + q_r$ within the cloud core corresponding to thermal overturning on the down-shear side of the cloud were found in each simulation with vertical wind shear (BASE, SPD050, SPD100, and SPD125).

In order to assess the effects of entrainment on the overall distribution of liquid water within the cloud core, time-height diagrams of the median and maximum values of q_c, q_r, and $q_c + q_r$ are shown in Figures 25-30 for NOWND, CONST, SPD050, BASE, SPD100, and SPD125, respectively. Each plot within these figures also includes contours of instantaneous values of E_{SA} (i.e. rather than averaging over one-minute periods, the values are plotted for each 6 s time step).

In NOWND (Figure 25), several separate thermals were produced, leading to 'streaks' of high values in the time-height diagrams of median q_c, q_r, and $q_c + q_r$. The greatest values of these variables were consistently just below cloud top, associated with the 'strongest' thermal. The overturning associated with this thermal also likely produced the relatively high entrainment values just below the relatively high hydrometeor mixing ratio values.

Because of the simpler structure in CONST (Figure 26), with only a single thermal produced, the time-height diagrams of median q_c, q_r, and $q_c + q_r$ each have a single 'band' of relatively high values just below cloud top. The highest values of entrainment were just below this 'band,' where the liquid water content was substantially lower, so it appears that dilution due to entrainment did have a notable effect on the liquid water content in NOWND and CONST (Figures 25, 26).

In the shear simulations (SPD050, BASE, SPD100, and SPD125), the picture is more complicated because of the successive thermals. In SPD050, there did not appear to be a decrease in median $q_c + q_r$ associated with the highest E_{SA} values (Figure 27). A strong increase in the maximum $q_c + q_r$ after 53 minutes and above 3000 m (Figure 27c,f) was due to the newer thermal emerging, described in Section 3.1 and shown in Figure 10. Figure 28 appears to reveal some dilution resulting from entrainment in BASE; at roughly 60 minutes and 5000 m altitude, there was a peak in entrainment exceeding 5 kg m^{-2} s^{-1}, and from that time through the end of the developing stage, the median $q_c + q_r$ decreased with height, which is not possible for adiabatic ascent. The maximum $q_c + q_r$ appeared to be affected less than the median, which is to be expected as entrainment due to overturning thermal circulations should only affect a particular region of the cloud core. However, the median q_r also increased directly below the area of 'dilution,' so there may have been rain produced which was not lifted further by the updraft, producing the decrease in $q_c + q_r$ with height. However, since median q_c values were also relatively low at these times and heights, entrainment and dilution likely contributed to the pattern in median $q_c + q_r$, but it was accentuated by rain fallout (Figure 28b,e). SPD100 (Figure 29) was more similar to BASE, in that there were lower-than-expected median $q_c + q_r$ values in the top 1000 m of the cloud at the end of the developing stage. Also, this simulation had a region of relatively high $q_c + q_r$ at roughly 57 minutes and 4500 m altitude, and E_{SA} values exceeded 5 kg m^{-2} s^{-1} at the same time and altitude. Subsequently, median $q_c + q_r$ values decreased with time at around 4500 m. Since there does not appear to be a substantial amount of rain indicated by the median q_r values below that height, it is likely that dilution due to entrainment caused the decrease in median $q_c + q_r$ after 57 minutes and at roughly 4500 m altitude in SPD100 (Figure 29c). SPD125 (Figure 30) was certainly affected by successive thermals, as implied by the rapid

42

cloud top height increase and the very high median $q_c + q_r$ values after 56 minutes. As a result, the time-height diagrams do not show strong evidence of dilution due to entrainment in SPD125.

In order to better quantify the relationship between entrainment and dilution of liquid water, the correlation between one-minute averaged E_{SA} and the two-minute percentage change in the horizontal median of $q_c + q_r$ (i.e. the change over the minute over which E_{SA} was averaged and the minute afterwards) within the cloud core was calculated for each simulation and reported in Table 4. Scatter plots of these two quantities are also shown in Figure 31. The two-minute change in $q_c + q_r$ was considered in order to capture more of the mixing resulting from entrainment, which requires more time after the entrainment event. A negative correlation would be expected, as dilution due to entrainment should reduce the core liquid water content. In NOWND, there was a moderate negative correlation, and in CONST, there was a weak negative correlation between one-minute E_{SA} and two-minute percent change in core median $q_c + q_r$. In each of the shear simulations, the two were effectively uncorrelated when considering all altitudes. However, as has been discussed, the shear simulations produced successive thermals which likely entrained modified air from prior thermals (similar to Moser and Lasher-Trapp 2017). Also, storm-relative inflow, which did not appear to cause substantial dilution, was stronger in the stronger-shear environments, and this inflow was strongest at low levels in the cloud (Figure 19). As a result, the points in Figure 31c-f corresponding to lower altitudes appear to be scattered randomly, while those corresponding to higher altitudes do show a negative relationship. Each simulation did have a moderate or strong negative correlation between one-minute E_{SA} and two-minute percent change in core median $q_c + q_r$, when only considering points above 4 km (Table 4). A perfect negative correlation was not present, as other factors such as condensation and rain fallout influence the liquid water content at a given altitude as well as

entrainment. This imperfect correlation seems to agree with Hannah (2017), who also did not find a strong correlation between entrainment and dilution in a series of bubble simulations, largely due to the 'moist shell' surrounding the cloud core.

3.3.3 Dilution of Buoyancy

Because the developing stage of each simulation only included the period up to a cloud top height of 6500-7500 m, below the height where the buoyancy of an adiabatically lifted parcel from the surface should begin decreasing for the thermodynamic sounding used (Figure 3), reductions in buoyancy should be evident from entrainment and mixing. This is especially true where environmental air has clearly been introduced into the cloud core by overturning thermal circulations. Cross-sections previously discussed already show some examples. Figure 10 shows reduced buoyancy in SPD050, particularly on the down-shear side where the overturning circulation entered the cloud core. This was also the case in Figure 19, which included vertical cross-sections from SPD050, SPD100, and SPD125. It was also apparent from this figure that as the shear (and "leaning over" of the cloud) increased, the region of greatest buoyancy became more concentrated along the up-shear side of the cloud core.

Although NOWND and CONST had much lower entrainment rates than the other simulations (Figures 12, 13, 15a), reductions in buoyancy due to entrainment did appear to occur in those simulations as well. This was perhaps aided by the fact that the clouds produced in NOWND and CONST were much narrower than those produced in the other simulations, and thus allowed for a greater portion of the cloud core to be diluted. The cloud core volume in NOWND and CONST was always substantially less than the cloud core volume in any of the shear runs for a given time or cloud top height (Figure 32). This difference in the sizes of the

44

clouds also likely contributed to the previously discussed dilution of liquid water content in CONST and NOWND. Figure 33 shows cross-sections of buoyancy in NOWND and CONST when the cloud top height was roughly 6500 m, and there were regions near the core edge with reduced buoyancy in both simulations. This dilution occurred at a higher cloud top height than in the other simulations, which was consistent with the lower entrainment rates in NOWND and CONST. The dilution in NOWND and CONST also appeared symmetrical, supporting the notion that the vertical wind shear in the other simulations produced the asymmetrical dilution patterns (Figures 18, 31).

Time-height diagrams of median buoyancy (in m s^{-2}) within the core with E_{SA} contours (Figure 34) for each simulation lend further evidence to the reduction of buoyancy by entrainment and mixing. All simulations except SPD125 appeared to have a period when the median buoyancy in the cloud core was substantially reduced at some altitudes above 3000 m. For example, at roughly 56 minutes and 4500 m altitude in SPD100, entrainment peaked at over 5 kg m^{-2} s^{-1}, then almost immediately afterward, the median buoyancy in the cloud core was notably decreased (Figure 34d). In CONST, the median buoyancy in the cloud core was roughly 0 m s^{-2} at 71 minutes and 5500 m altitude, following a time when entrainment at that altitude exceeded 2 kg m^{-2} s^{-1} (Figure 34b). The maximum buoyancy in the cloud core did not usually decrease in the same manner after an entrainment event, as the time-height diagrams in Figure 35 show. There were even notable increases in the maximum buoyancy in the cloud core above 3000 m altitude during the late developing stage of BASE, SPD050, SPD100, and SPD125. These increases in maximum buoyancy are associated with successive thermals, such as the thermal which emerged between 54 and 56 minutes in SPD050 (Figure 35c).

3.4 Differences in Precipitation Development

There were differences in the rate of precipitation formation within the cloud core among the different simulations, which could be attributable to successive thermals as well as entrainment. Figure 36 shows three comparisons of entrainment microphysical precipitation efficiency (EMPE) among the simulations. The first is a simple time series of EMPE (Figure 36a), which was not very useful for comparison because the simulations formed clouds at different times. Therefore, EMPE was also plotted in a time series where the time at which a cloud core first appeared was defined as 0 minutes (Figure 36b). This revealed a trend of quicker EMPE increases for the simulations with less vertical wind shear, with the exceptions of NOWND and SPD125. EMPE was lowest in SPD125 for most of the developing stage, as would be expected, but at 54 minutes, or roughly 15 minutes after a cloud core first formed, in SPD125, the EMPE increased rapidly. This corresponds roughly to the time at which the later thermal illustrated in Figure 9 ascended into air modified by a previous thermal, which also produced the rapid cloud top ascent and spike in maximum updraft speed around that time (Figure 6). This connection between successive thermals and precipitation production agrees with the results of Moser and Lasher-Trapp (2017).

The low EMPE values throughout the developing stage in NOWND were much more surprising. Given the relatively fast cloud top ascent rate in NOWND (Figure 6), the difference in EMPE between NOWND and the other simulations was even greater when comparing at the same cloud top height (Figure 36c). Figure 37 includes comparisons of the components of EMPE, each normalized by cloud core volume, plotted in the same manner as Figure 36b, where the time of the initial cloud core appearance was defined as 0 minutes. When compared in this way, the condensate mass normalized by core volume (in g m^{-3}) was greatest in NOWND for

46

most of the developing stage (Figure 37a). However, the precipitation mass normalized by core volume (in g m^{-3}) for NOWND was more similar to BASE and SPD100, and it was lower than CONST and SPD050 throughout the developing stage (Figure 37b). The precipitation mass (numerator) component of EMPE appeared to largely control the resulting EMPE values more than the condensate mass (denominator) component, as indicated by the similarities between Figure 36b and Figure 37b. The total condensate mass, however, in NOWND was relatively high and similar to CONST for much of the developing stage (Figure 37c).

It seems that a slower conversion of condensate to precipitation (e.g. from cloud droplets to rain drops) was the cause of the lower EMPE in NOWND, rather than less available condensate to convert due to dilution by entrainment. In Figure 6a, it was shown that clouds initially appeared in NOWND and CONST at roughly 35 minutes. It then took an additional 14.5 minutes for a cloud core to appear in NOWND, but 21.3 minutes in CONST. This delayed growth in CONST is also apparent from the later "upturn" in the cloud top height time series (Figure 6a). Because the autoconversion of cloud water to rain depends upon the cloud droplet sizes, which is a function of condensational growth time, NOWND may have had less time to begin the autoconversion process prior to cloud core formation, such that it achieved higher condensate mass but lower rain mass, producing lower values of EMPE.

Besides these complications, however, the simulations broadly follow a trend of greater shear being associated with more entrainment, as well as slower precipitation formation, with successive thermals complicating their relationship.

3.5 Tables and Figures

Table 3. Summary of the change in cloud top height during the developing stage in each simulation.

Simulation Name	Start of Developing Stage (min.)	Cloud Top Height at Start of Developing Stage (m)	End of Developing Stage (min.)	Cloud Top Height at End of Developing Stage (m)	Cloud Top Ascent Rate (m s^{-1})
BASE	41.5	1950	64.1	6050	3.0
NOWND	49.5	1850	63.0	6350	5.6
CONST	56.3	1850	71.0	6750	5.6
SPD050	41.0	1950	59.5	7350	4.9
SPD100	40.1	1950	62.9	6450	3.3
SPD125	39.2	1950	59.0	5950	3.4

Table 4. Correlation coefficients between the two-minute percentage change in the horizontal median of $q_c + q_r$ within the cloud core and E_{SA} averaged horizontally and for the first minute of that two-minute period, each for a given altitude.

Simulation Name	R for All Heights	R Only for Heights Above 4 km
NOWND	-0.52	-0.76
CONST	-0.23	-0.41
SPD050	-0.01	-0.41
SPD100	0.05	-0.72
BASE	-0.07	-0.61
SPD125	0.06	-0.88
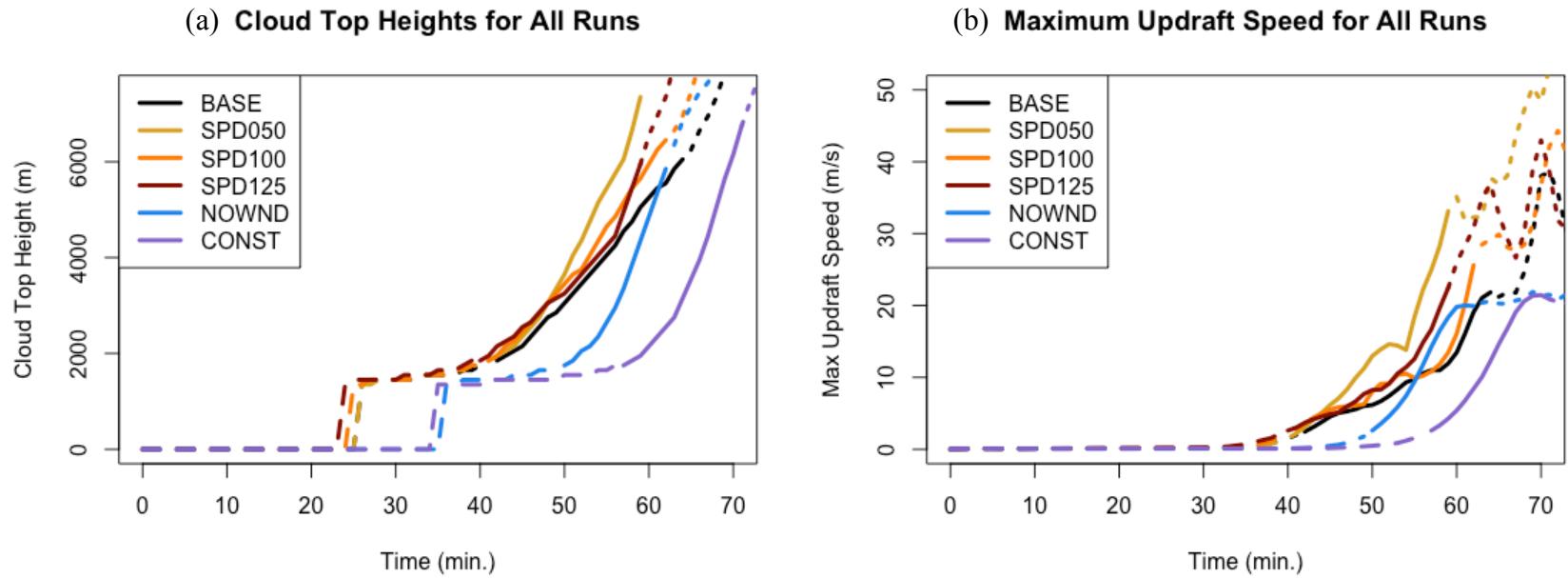
Figure 6. Time series of (a) cloud top height and (b) maximum updraft speed, for all simulations. Solid part of curves denote time of the developing stage for each simulation. Dashed part of curves show times before the developing stage, and dotted portions for the time after the developing stage.
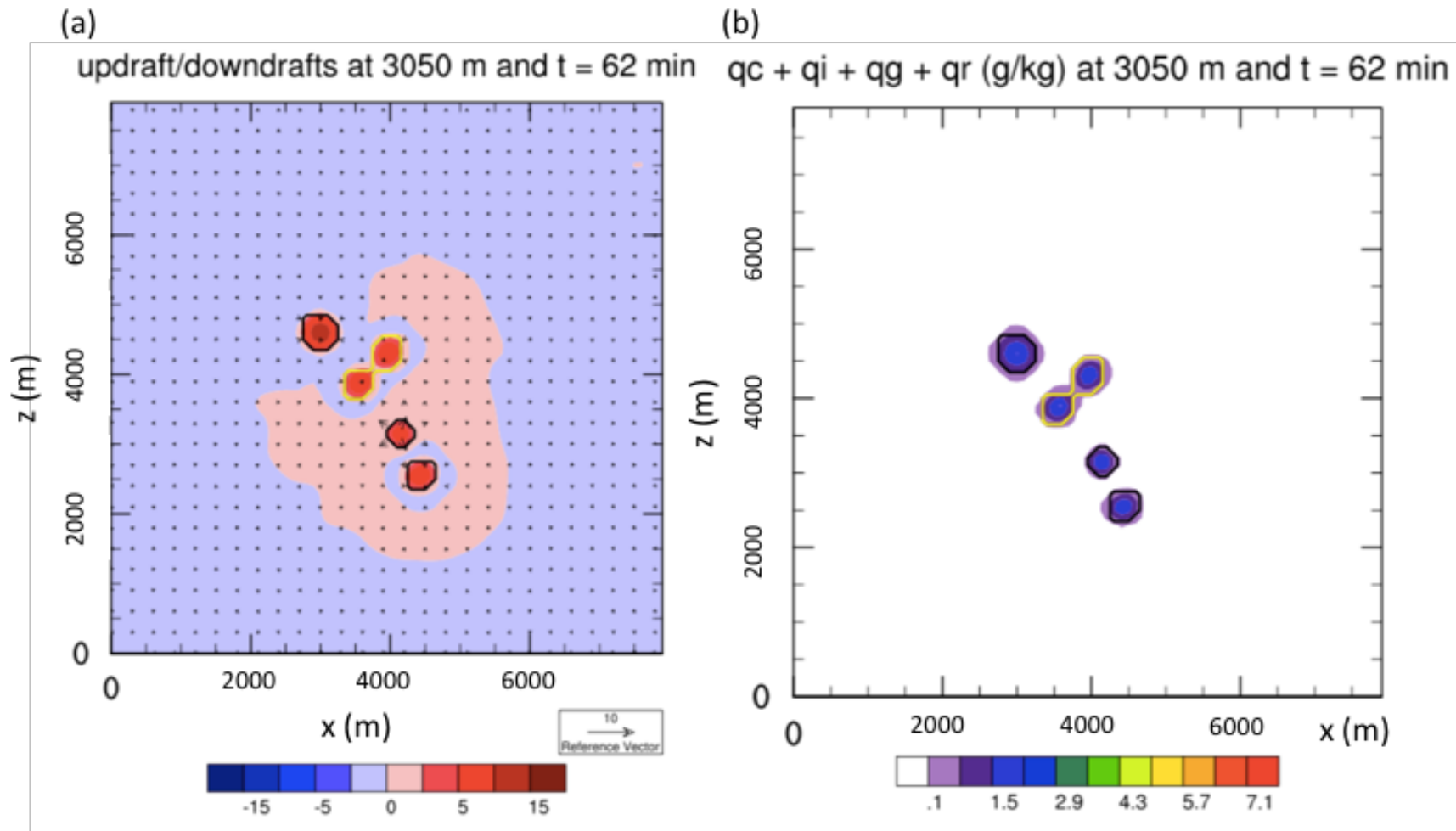
Figure 7. Horizontal cross-sections for NOWND at 62 minutes and 3050 m altitude, showing (a) vertical velocity and wind vectors (in m s⁻¹) and (b) hydrometeor mixing ratio (in g kg⁻¹). Cloud cores are outlined in black, with the 'main' cloud core outlined in yellow.
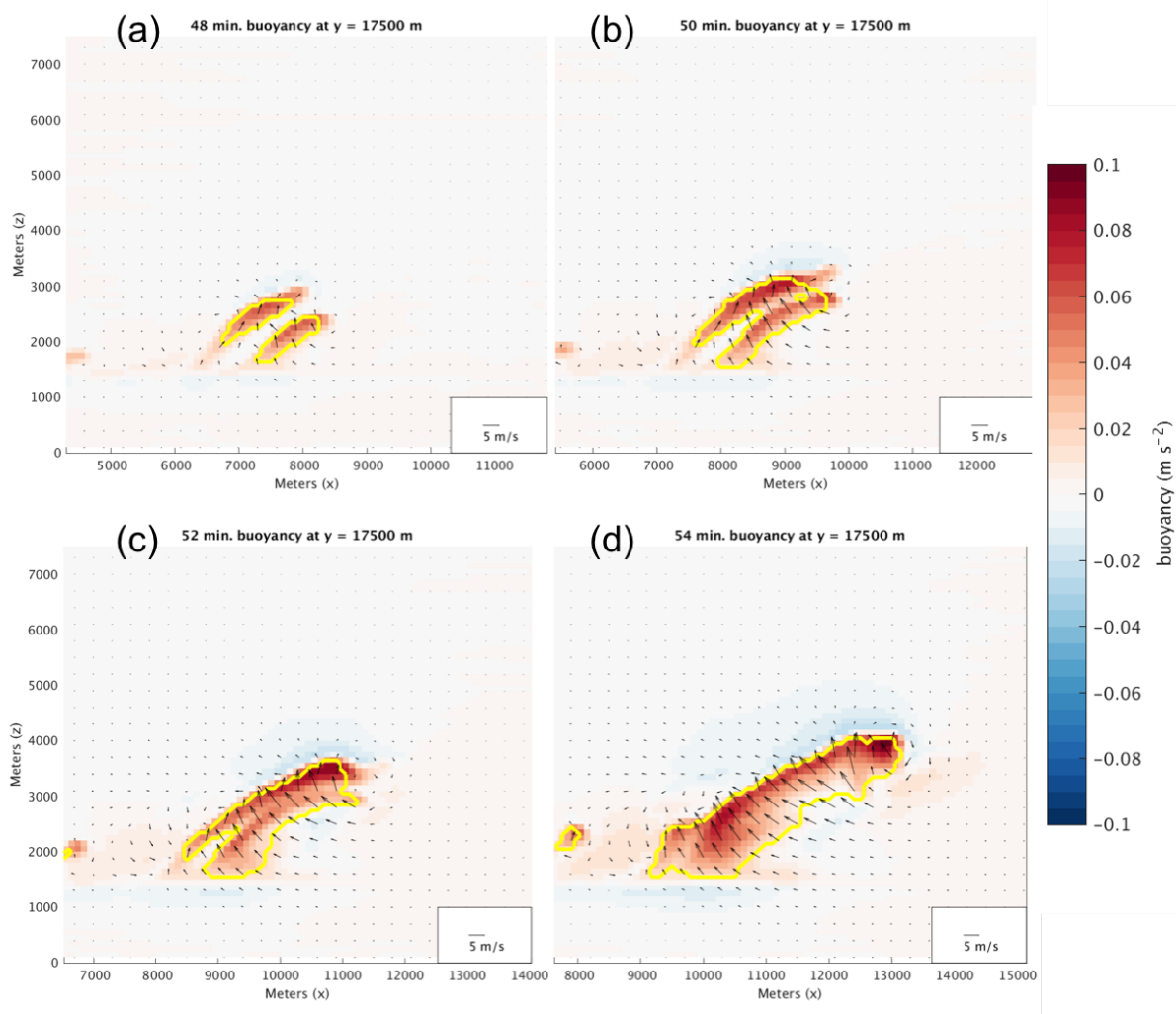
Figure 8. Vertical (west-east) cross-sections of buoyancy for SPD100, at (a) 48 minutes, (b) 50 minutes, (c) 52 minutes, and (d) 54 minutes. Perturbation wind vectors overlaid. Cloud cores outlined in yellow. X-axis shifts eastward for each sequential plot.
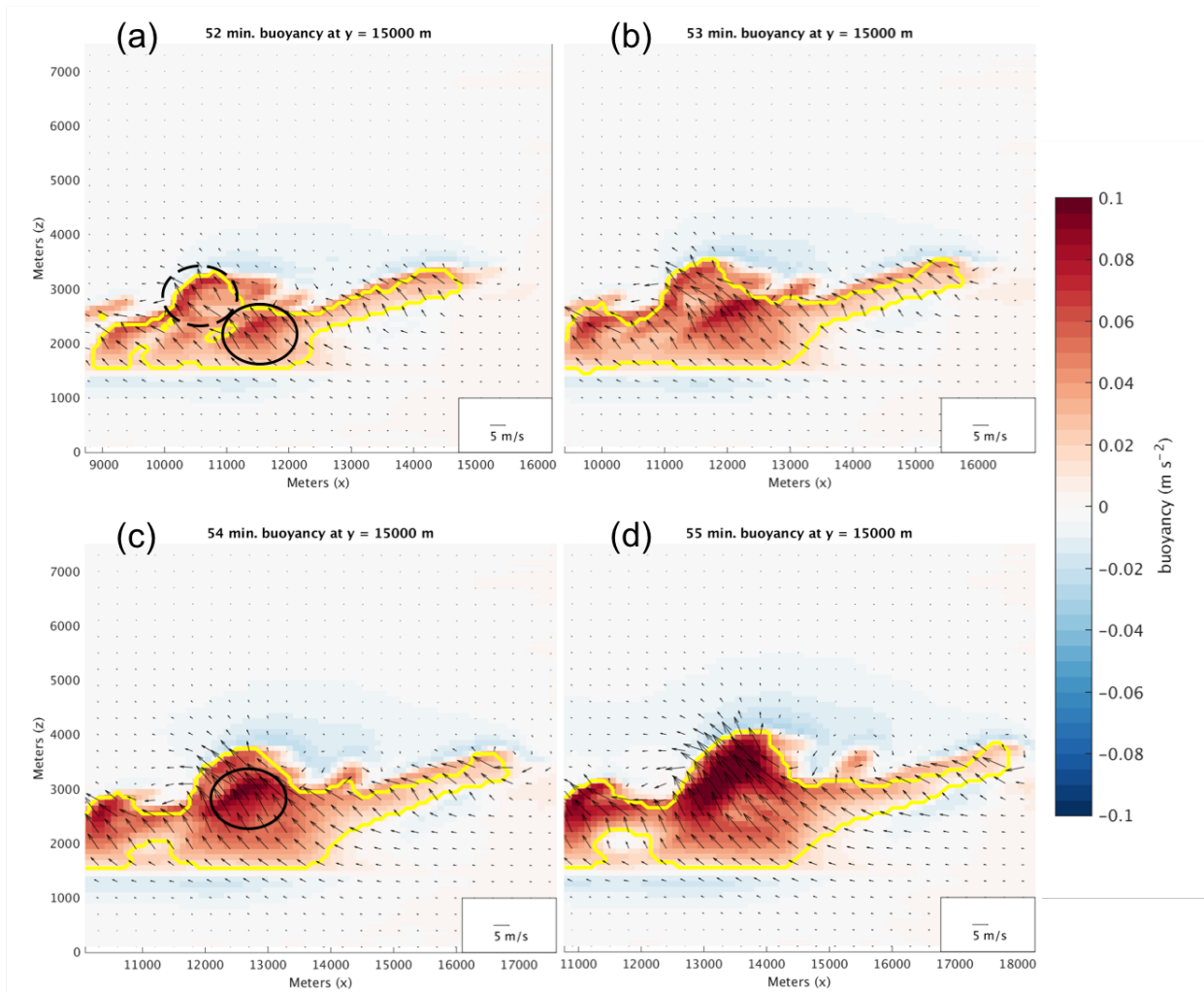
Figure 9. As in Fig. 8, except for SPD125 at (a) 52 minutes, (b) 53 minutes, (c) 54 minutes, and (d) 55 minutes.
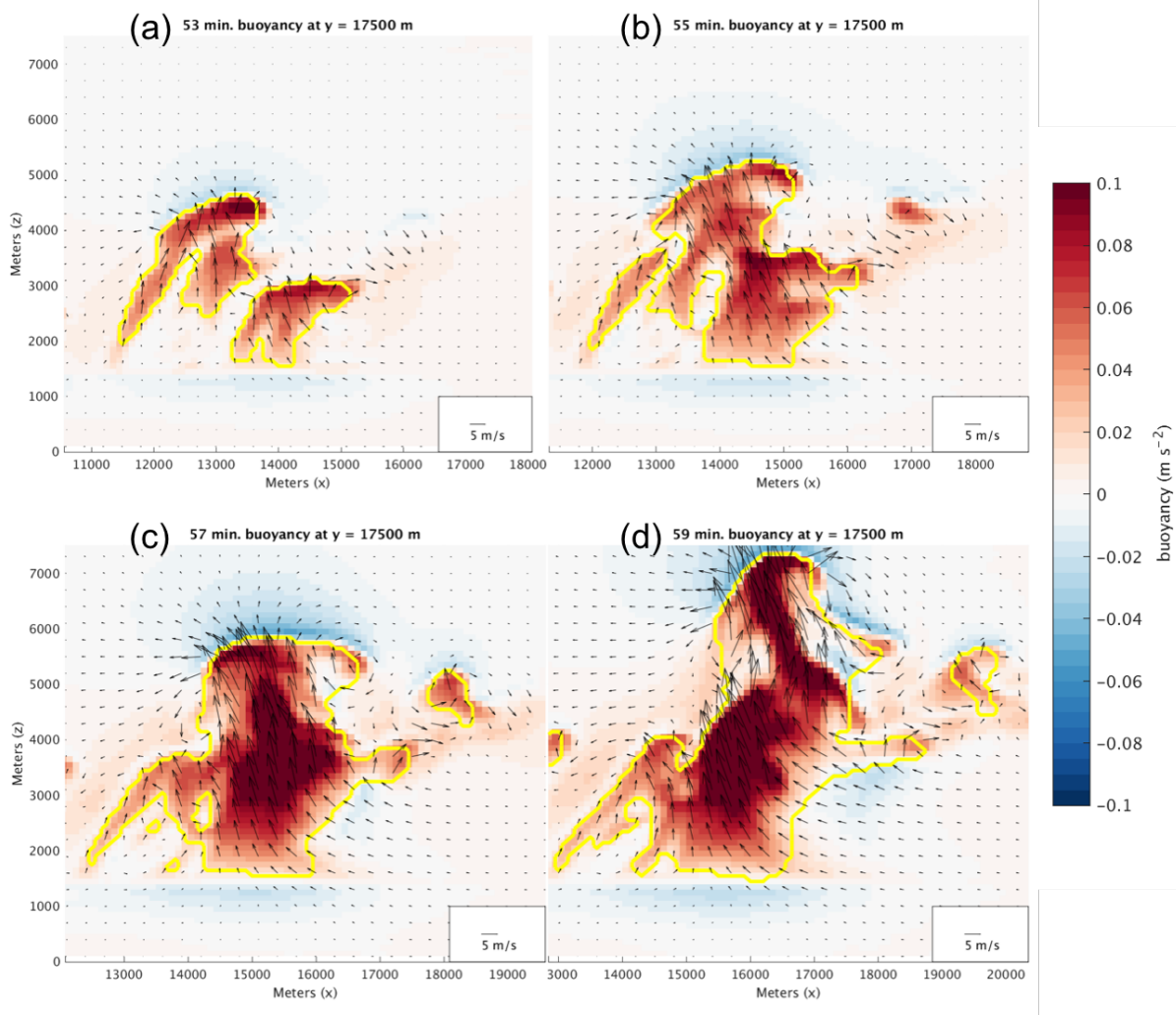
Figure 10. As in Fig. 8, except for SPD050 at (a) 53 minutes, (b) 55 minutes, (c) 57 minutes, and (d) 59 minutes.
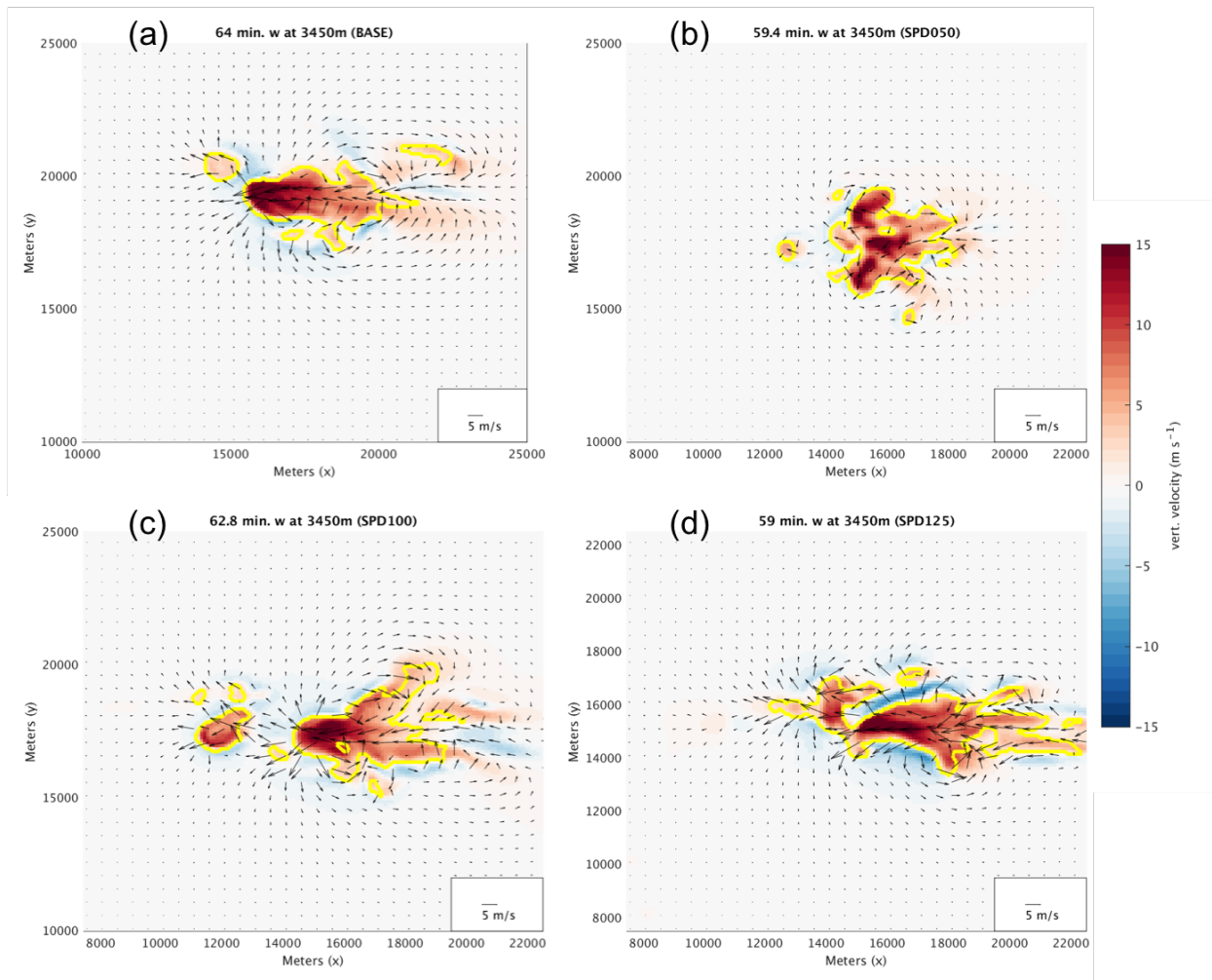
Figure 11. Horizontal cross-sections of vertical velocity with horizontal perturbation wind vectors at 3450 m altitude at the end of the developing stage for (a) BASE, (b) SPD050, (c) SPD100, and (d) SPD125. Cloud cores outlined in yellow.
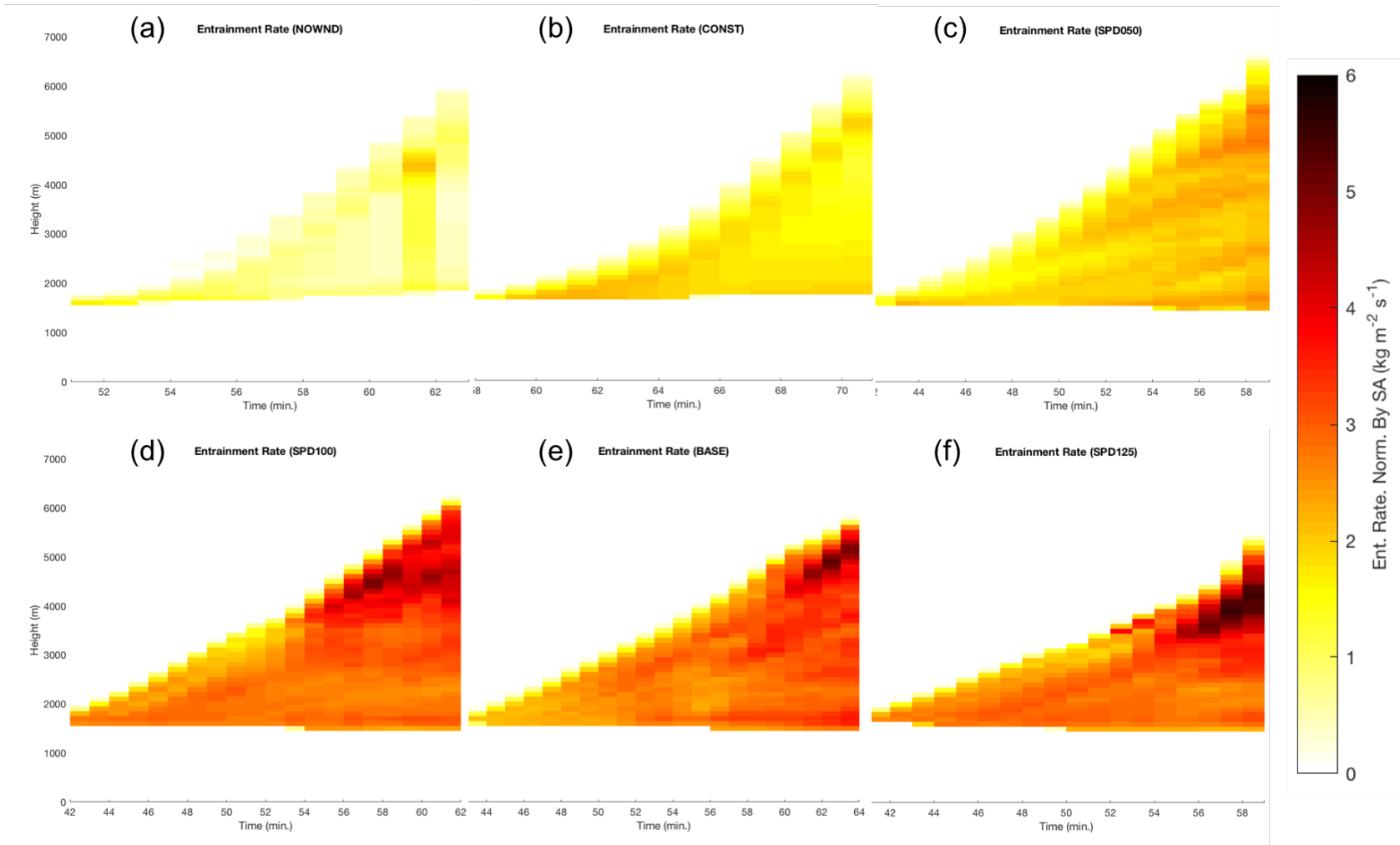
Figure 12. Time-height diagrams of E_{SA} (in kg m^{-2} s^{-1}, calculated using the perturbation winds) for (a) NOWND, (b) CONST, (c) SPD050, (d) SPD100, (e) BASE, and (f) SPD125. Time axes are different for each simulation based on the definition of the developing stage for each simulation.
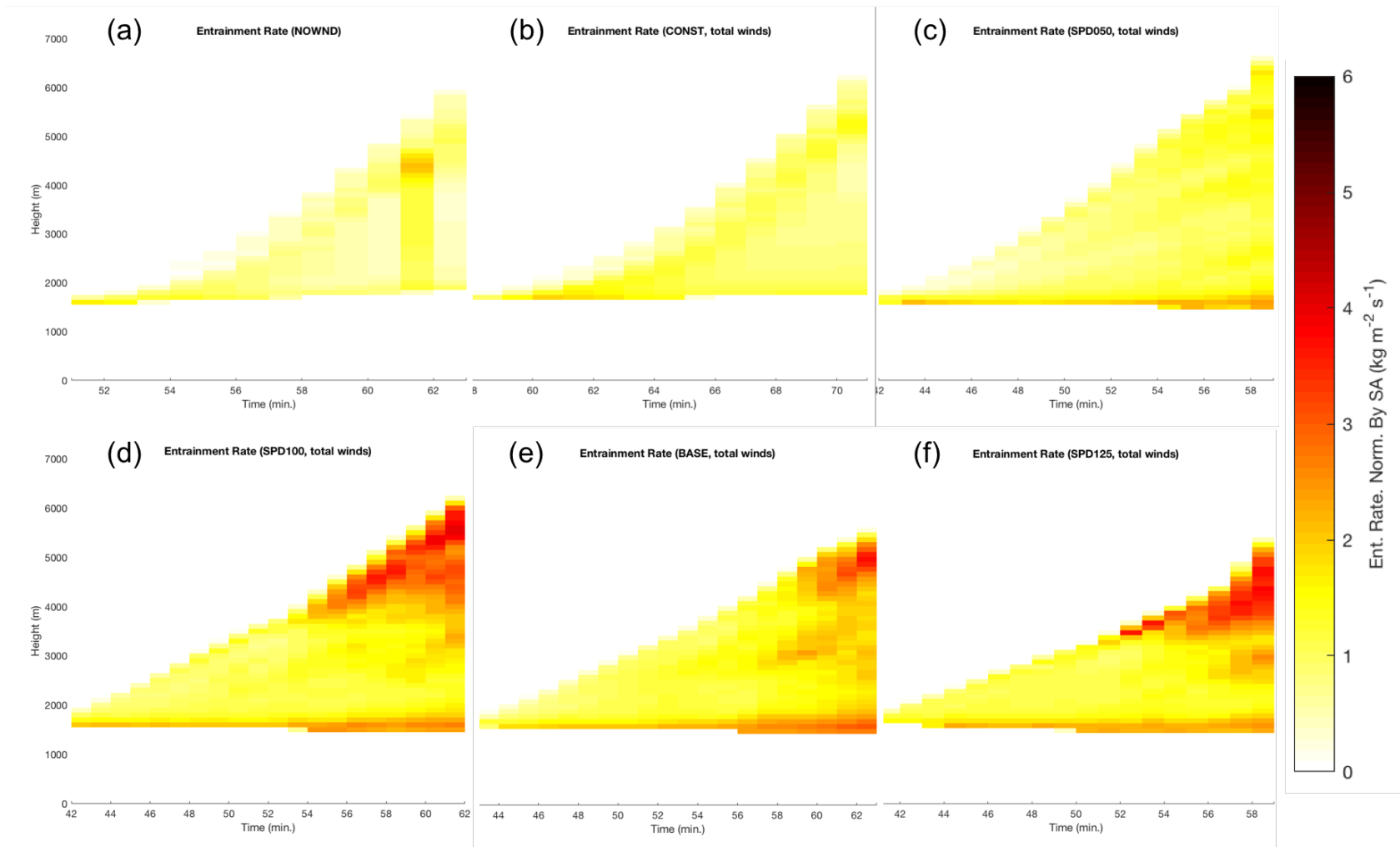
Figure 13. As in Fig. 12, except values calculated using the total wind.
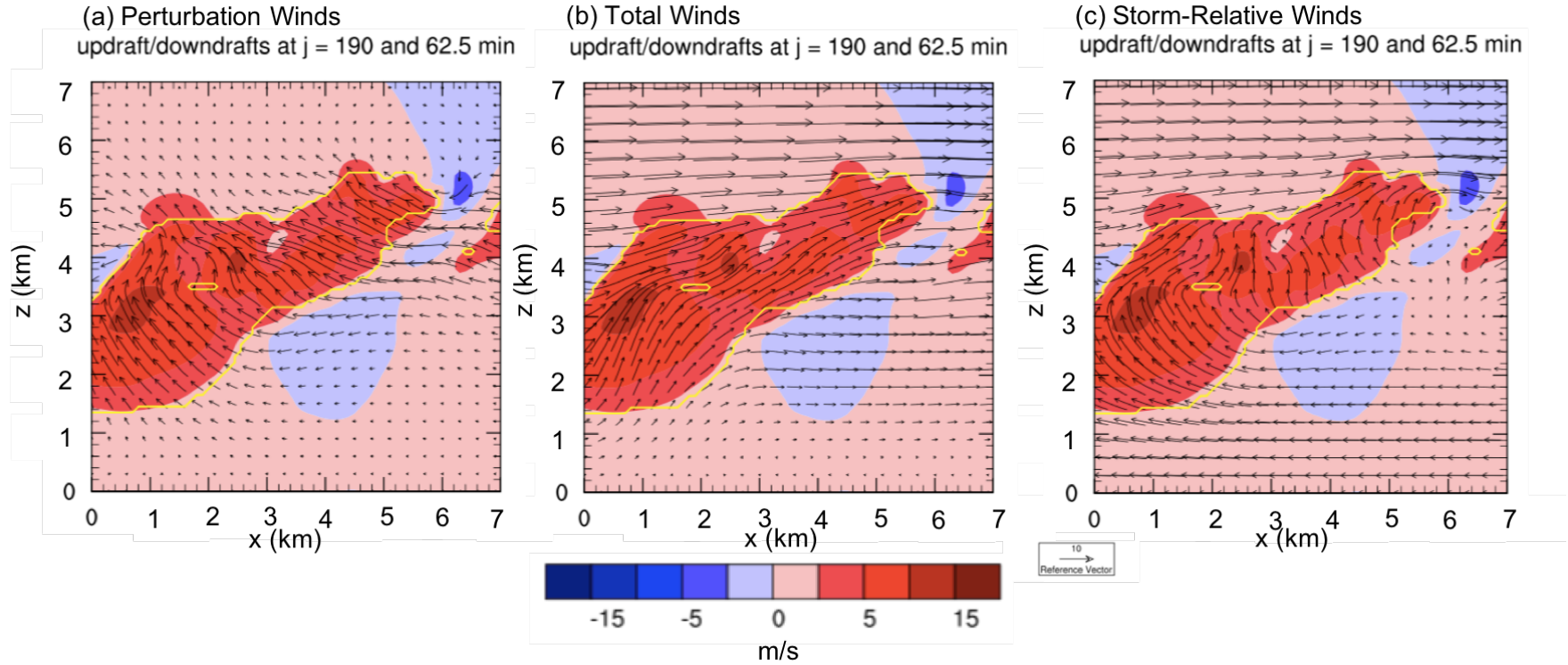
Figure 14. Vertical (west-east) cross-sections of vertical velocity from BASE at 62.5 minutes, overlaid with (a) perturbation wind vectors, (b) total wind vectors, and (c) storm-relative wind vectors.
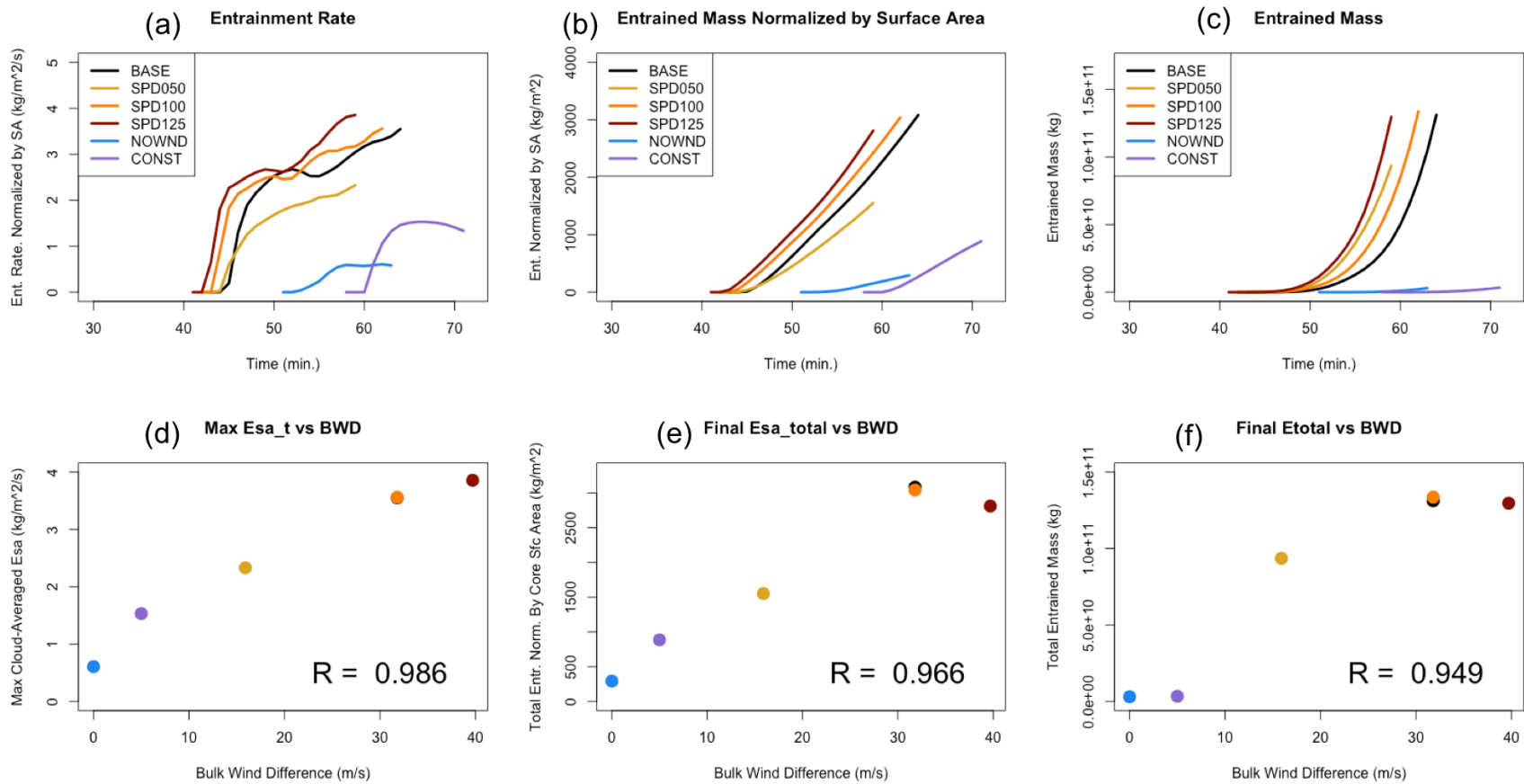
Figure 15. Top row: time series of (a) $E_{SA,t}$, (b) $E_{SA,total}$, and (c) E_{total}, for all simulations as indicated in the legend of each plot. Bottom row: scatter plots of (d) maximum $E_{SA,t}$, (e) $E_{SA,total}$ at end of developing stage, and (f) E_{total} at end of developing stage against 0-6 km bulk wind shear. Color of points in scatter plots corresponds to simulation colors in top row; correlation coefficients as noted. Points for BASE and SPD100 overlap in each scatter plot.
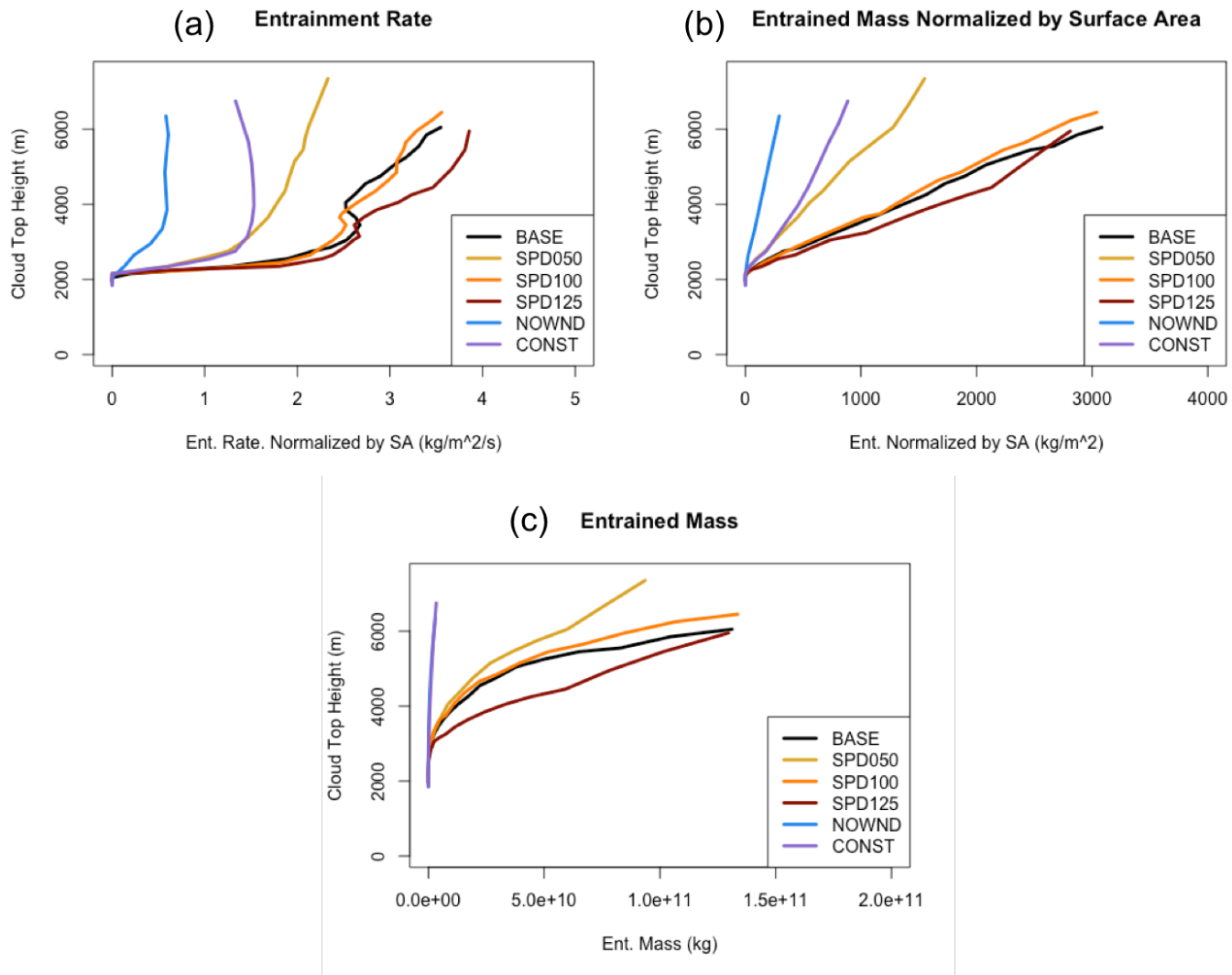
Figure 16. (a) $E_{SA,t}$, (b) $E_{SA,total}$, and (c) E_{total} plotted against cloud top height for each simulation as indicated in the legend of each plot.

In (c), CONST curve obscures the NOWND curve.
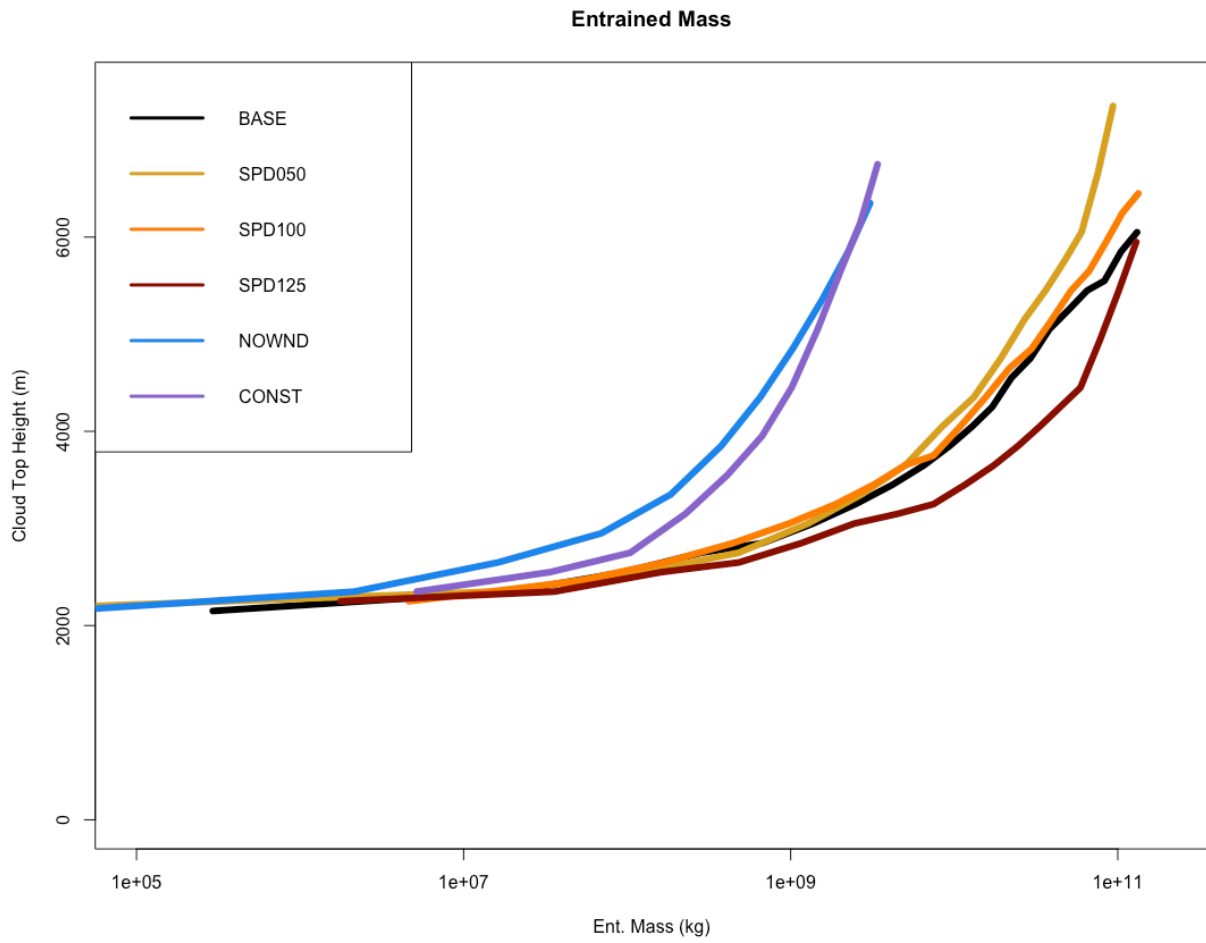
Figure 17. As in Figure 16c, but with E_{total} on a logarithmic scale.
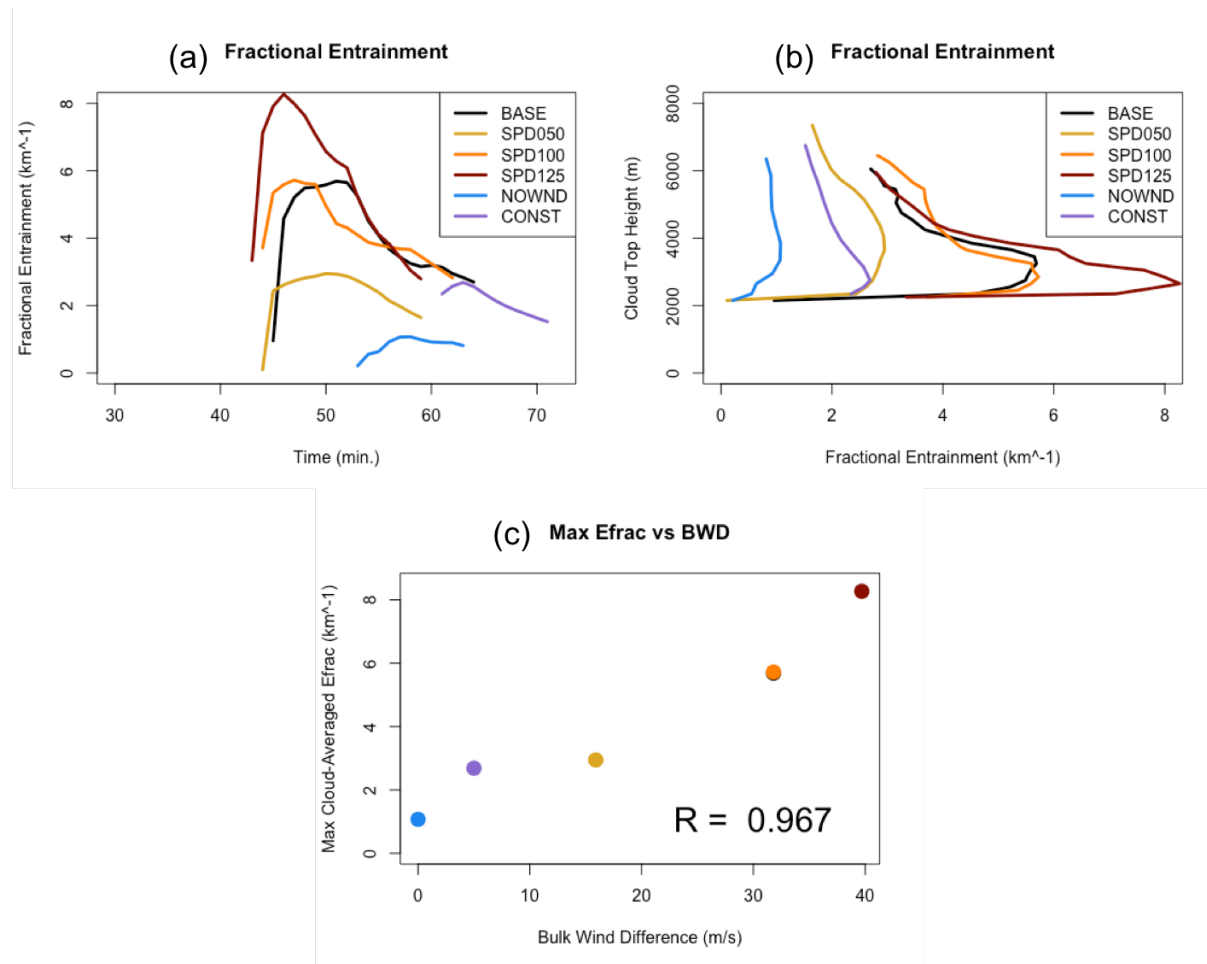
Figure 18. Fractional entrainment for the six different simulations: (a) time series, (b) versus cloud top height, and (c) maximum value during the developing stage versus 0-6 km bulk wind shear, with correlation coefficient as shown. Points in (c) are colored by simulation, as in (a) and (b), and points corresponding to BASE and SPD100 overlap in (c).
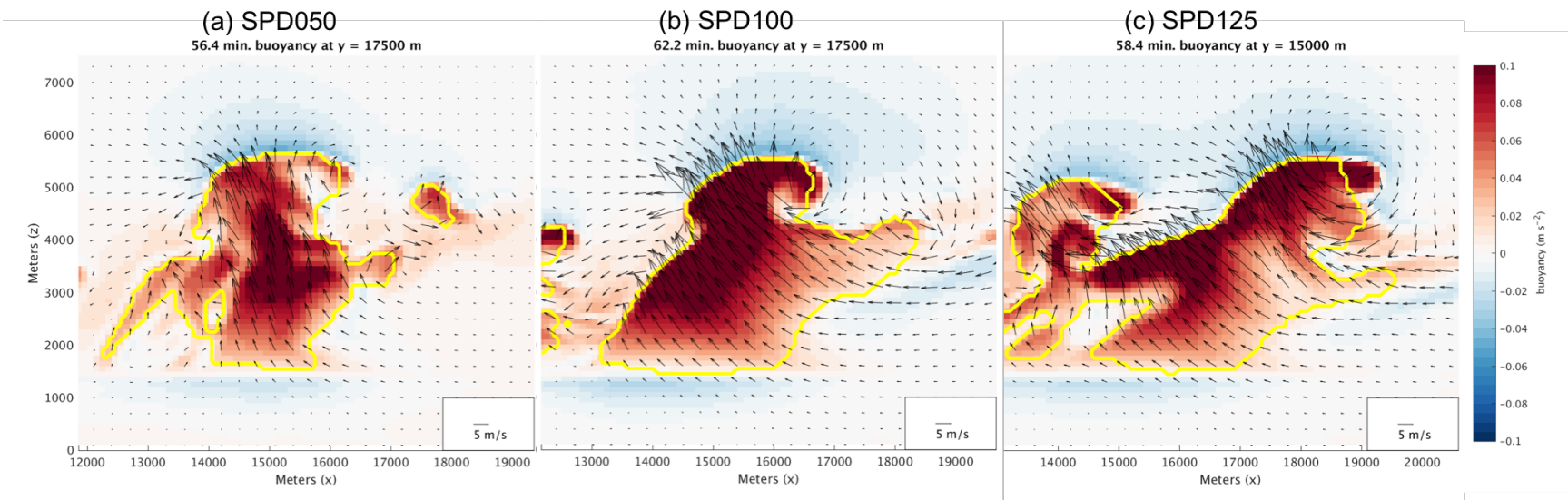
Figure 19. Vertical (west-east) cross-sections of buoyancy with perturbation wind vectors overlaid, for (a) SPD050, (b) SPD100, and

(c) SPD125 at times when the cloud top height was between 5000 and 6000 m. Cloud cores outlined in yellow.
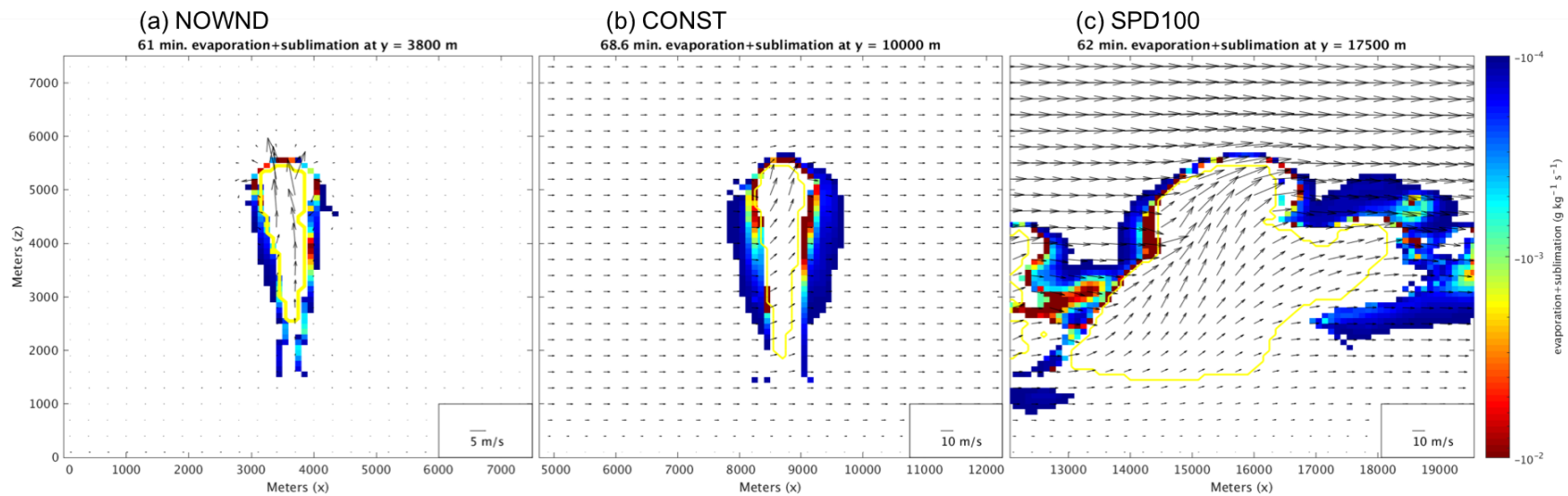
Figure 20. Vertical (west-east) cross-sections of total evaporation and sublimation, with total wind vectors overlaid, for (a) NOWND, (b) CONST, and (c) SPD100, at times when the top of the main cloud core was at roughly 5500 m altitude. Cloud cores outlined in yellow. Color scale indicates negative values and is logarithmic, so that larger rates are warmer colors. Reference vector magnitude is different for NOWND than for other cases.

63
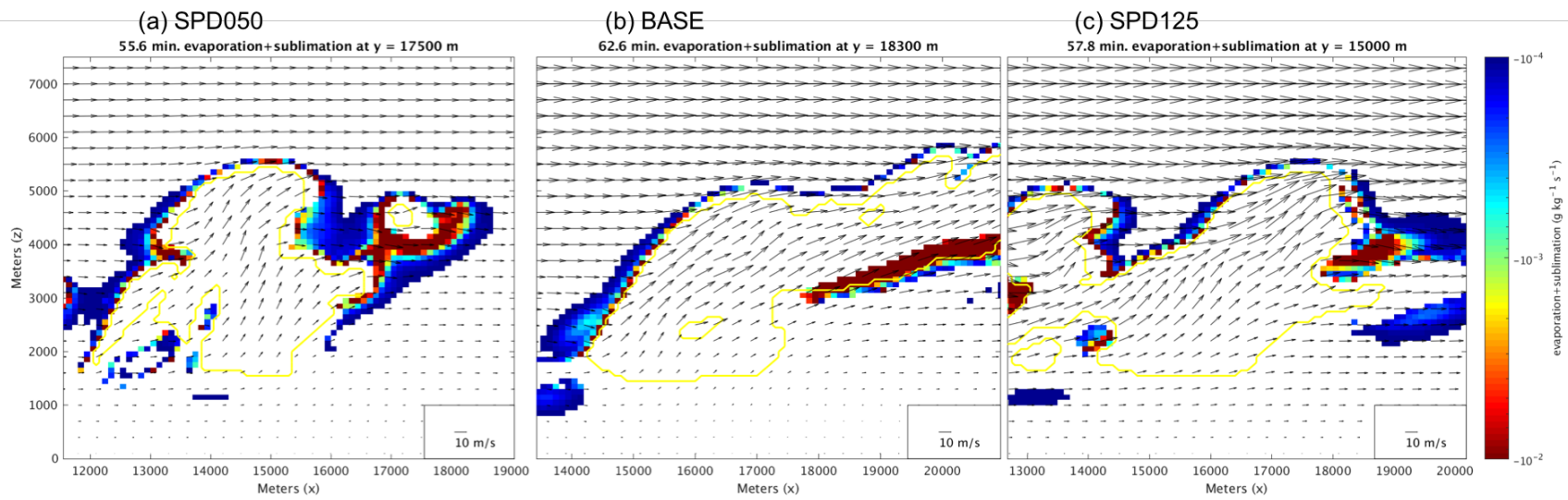
Figure 21. As in Figure 20, but for (a) SPD050, (b) BASE, and (c) SPD125.
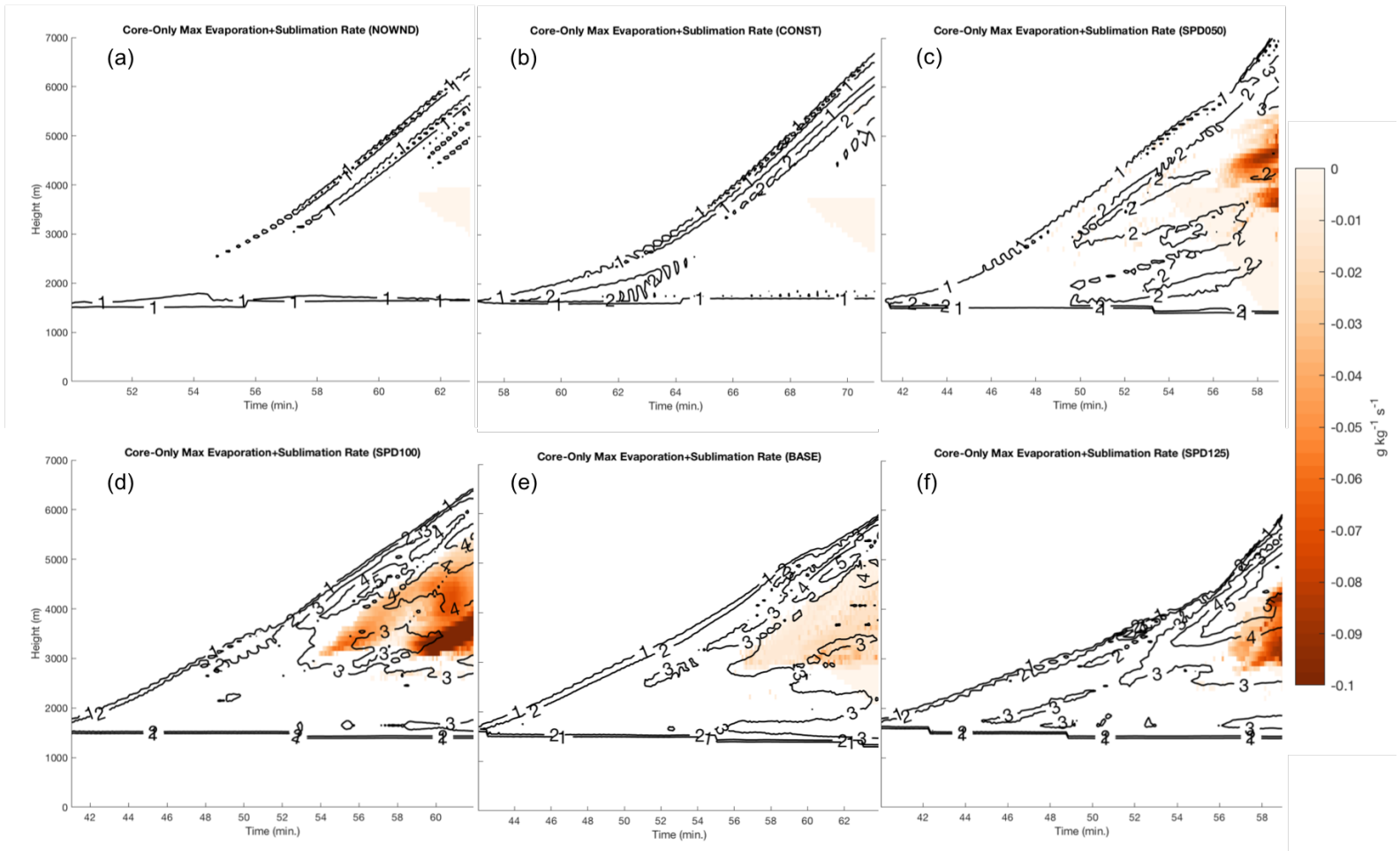
Figure 22. Time-height diagrams of the maximum total evaporation and sublimation rates within the cloud cores for (a) NOWND, (b) CONST, (c) SPD050, (d) SPD100, (e) BASE, and (f) SPD125. Contours of instantaneous (i.e. at each 6-second time step) E_{SA}, calculated using the perturbation wind, overlaid.
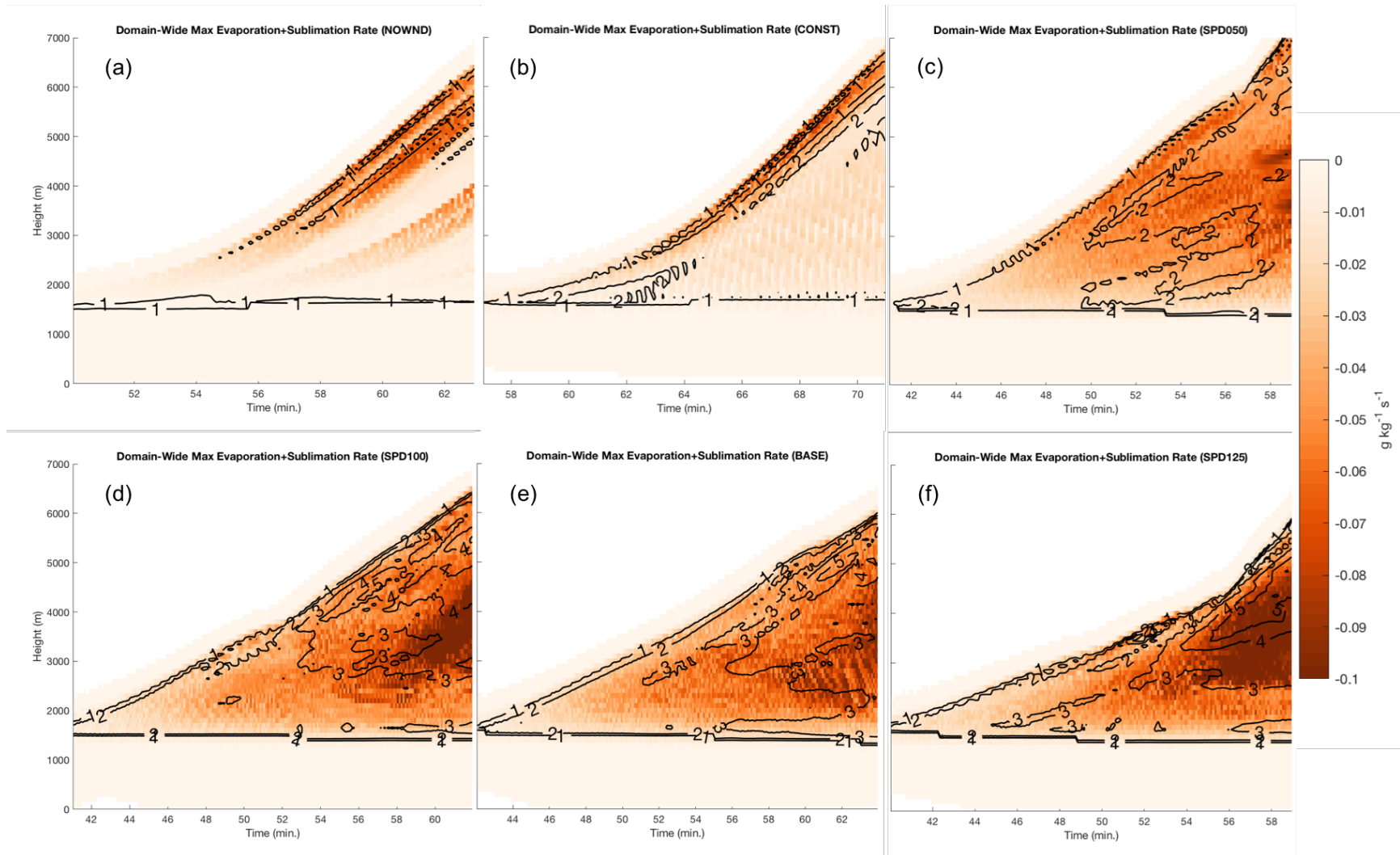
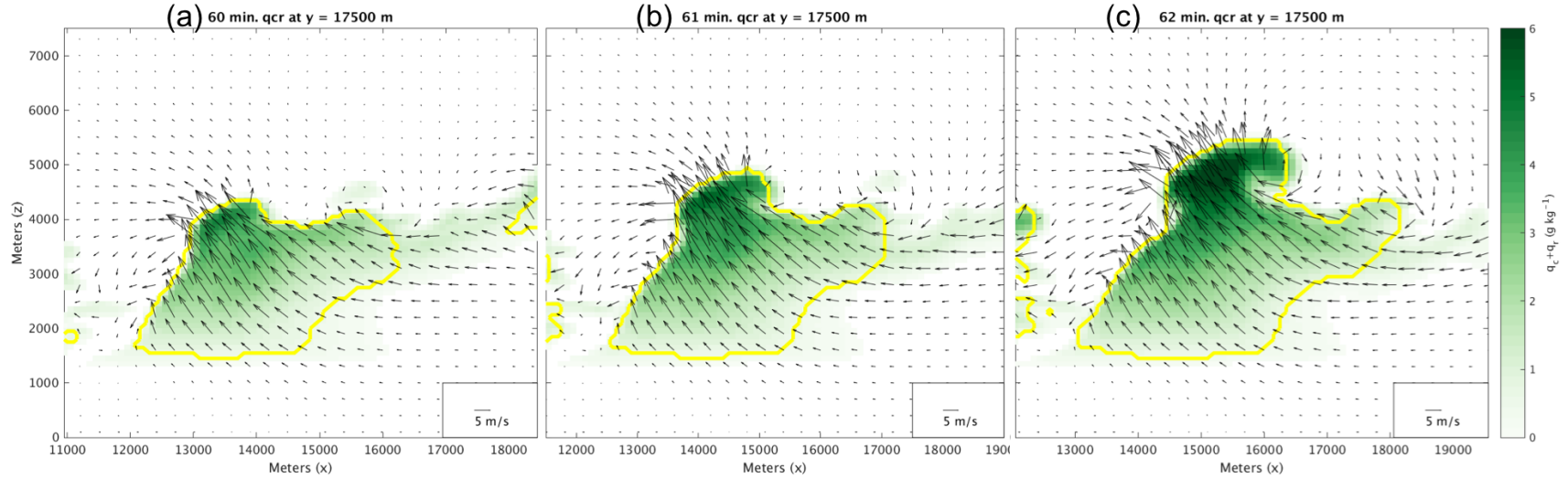Figure 23. As in Figure 22, but with the maximum total evaporation and sublimation rate over the entire domain.

Figure 24. Vertical (west-east) cross-sections of combined cloud and rain water mixing ratios for SPD100 at (a) 60 minutes, (b) 61 minutes, and (c) 62 minutes, with perturbation wind vectors overlaid. Cloud cores outlined in yellow. X-axis shifted eastward with each sequential plot.
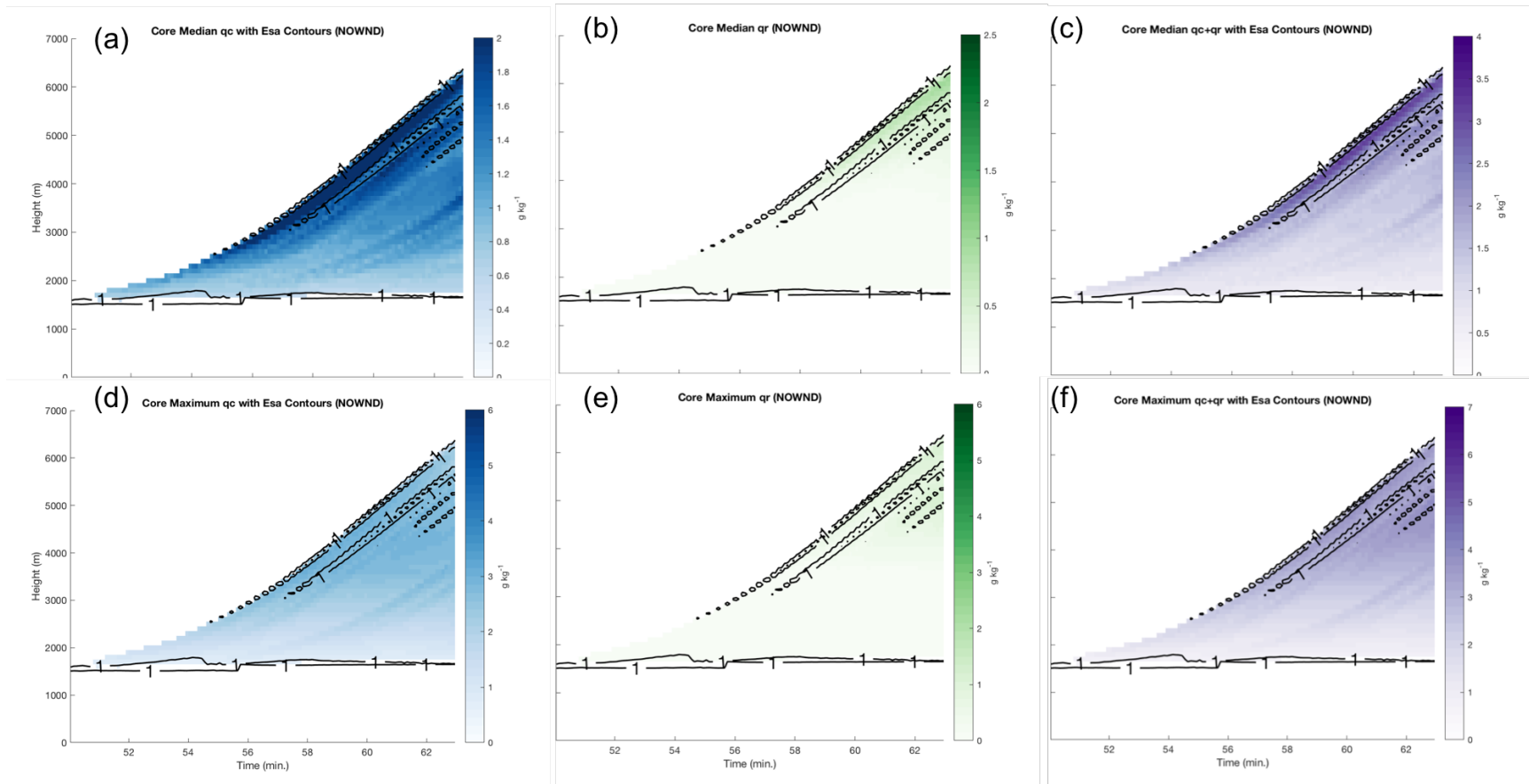
Figure 25. Time-height diagrams from NOWND showing (top row) median and (bottom row) maximum values of (left) q_c, (center) q_r, and (right) $q_c + q_r$ within cloud core. Contours of instantaneous (i.e. at each 6-second time step) E_{SA}, calculated using the perturbation wind, overlaid.
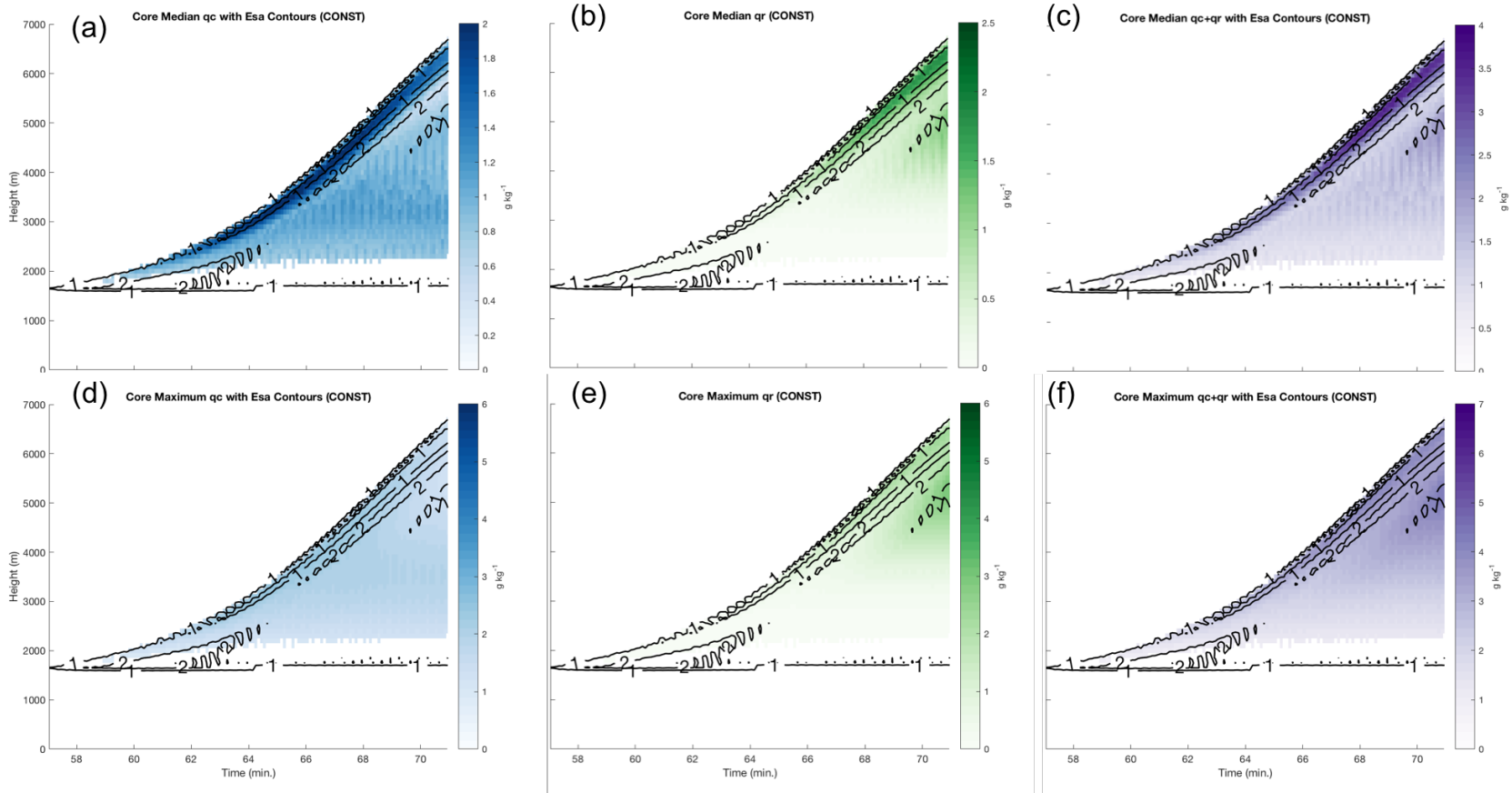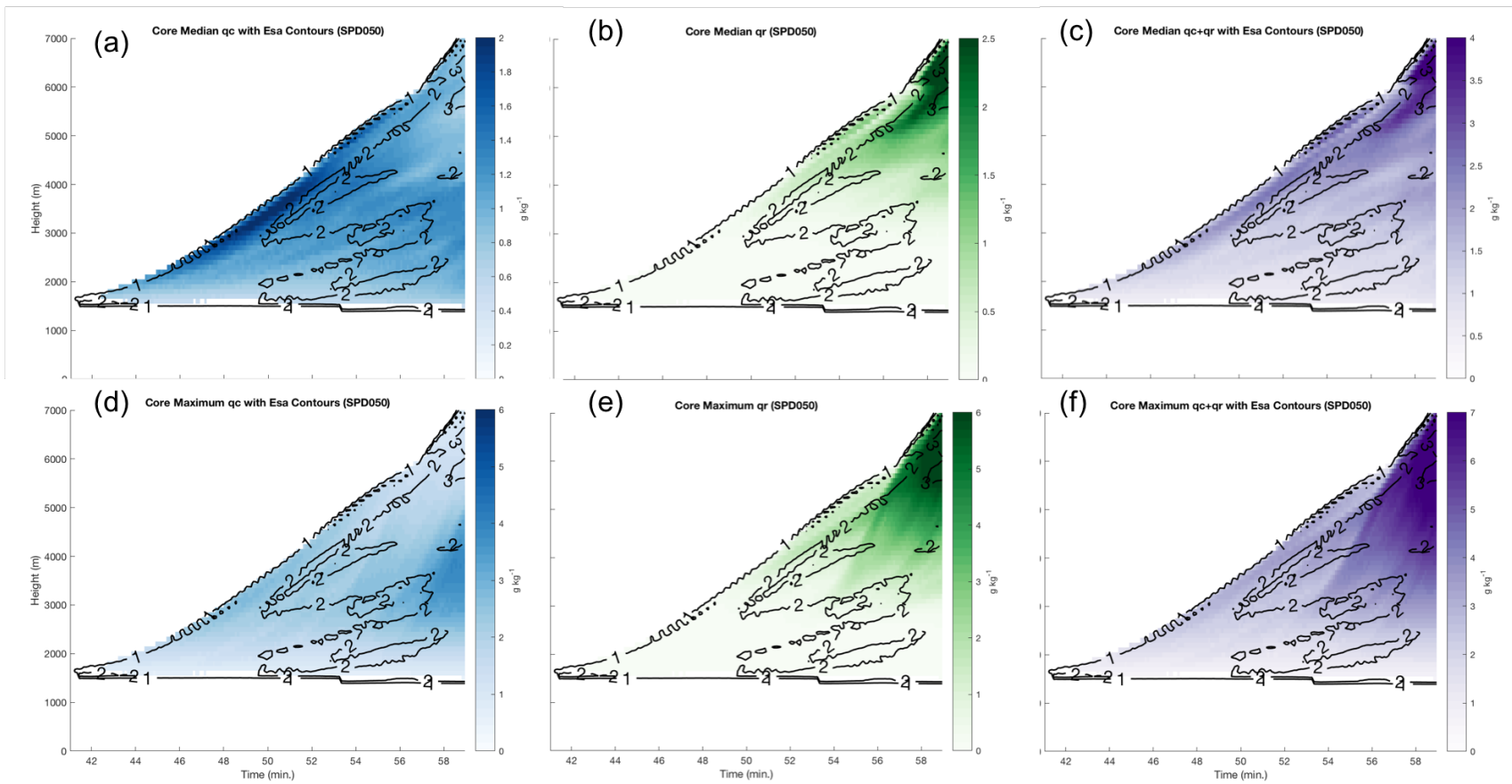
Figure 26. As in Figure 25, but for CONST.

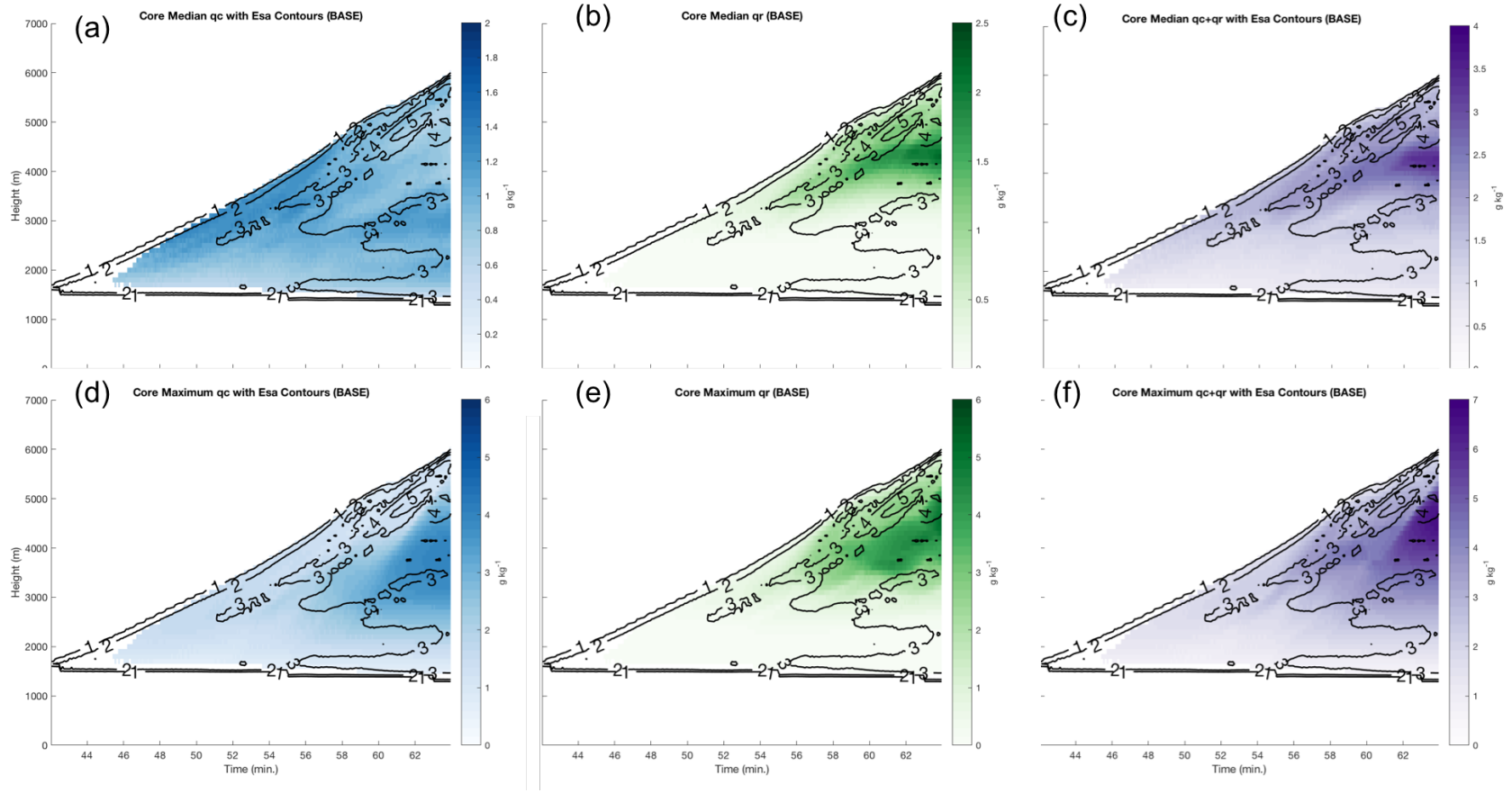Figure 27. As in Figure 25, but for SPD050.

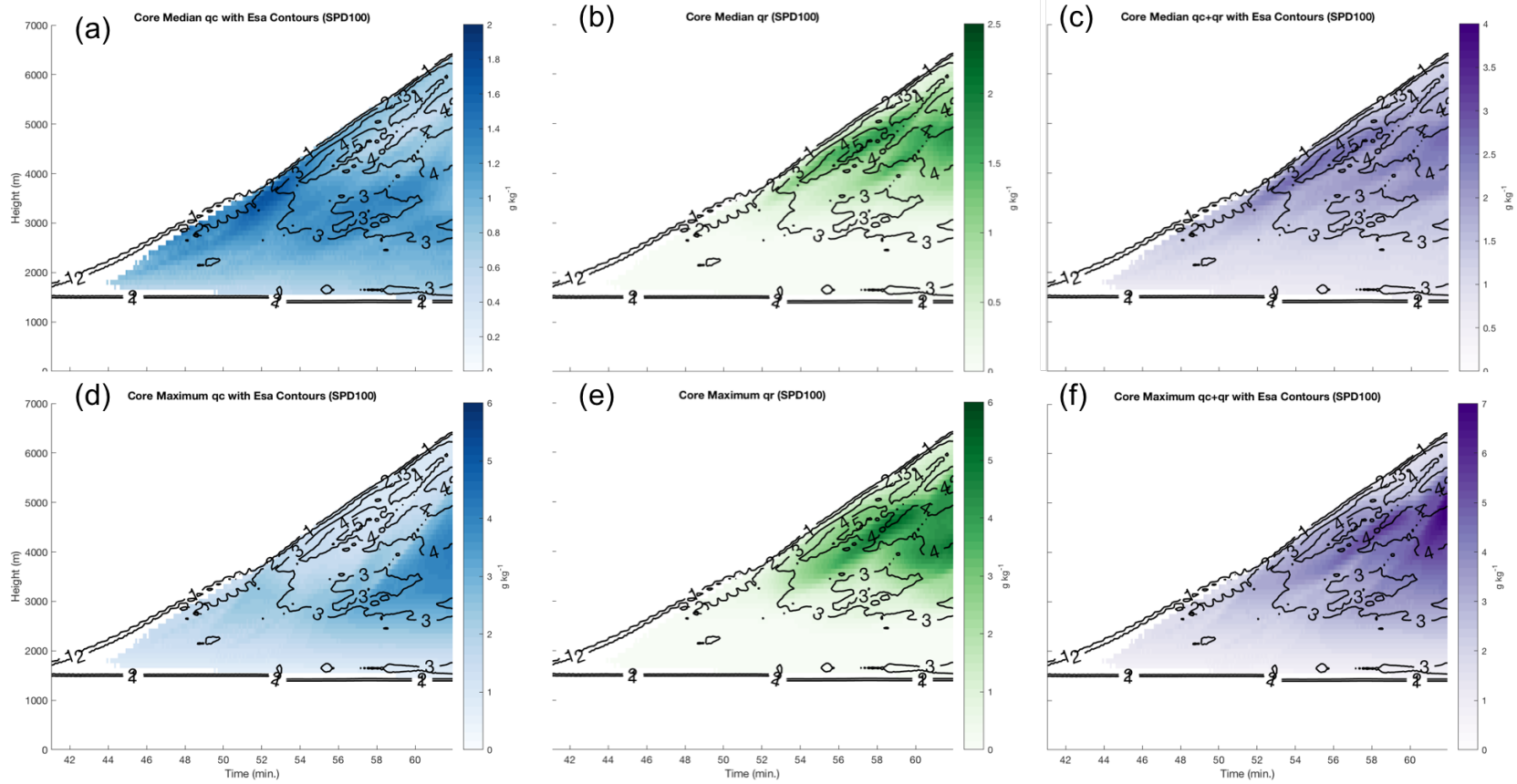Figure 28. As in Fig. 25, but for BASE.
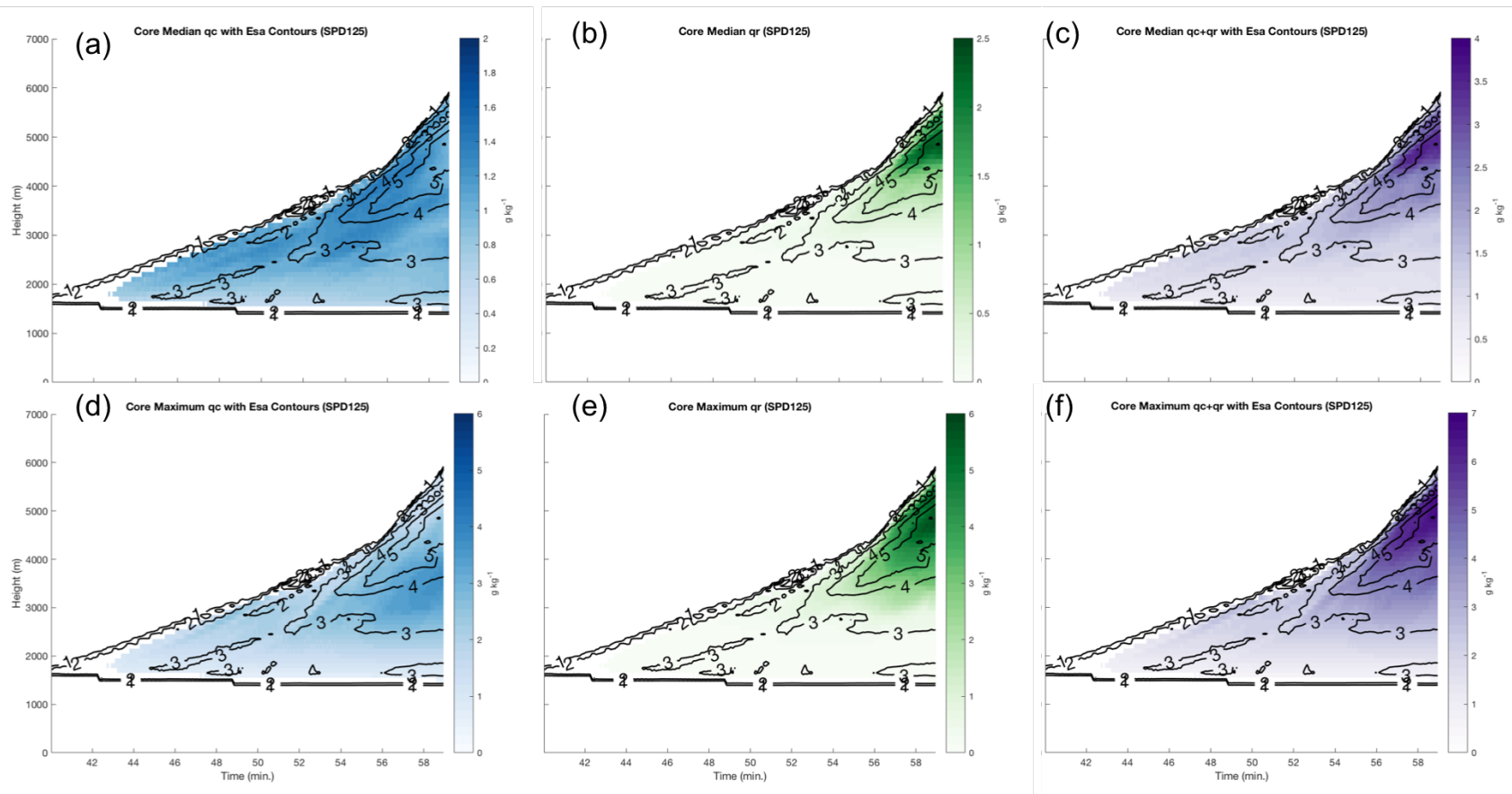
Figure 29. As in Figure 25, but for SPD100.

Figure 30. As in Figure 25, but for SPD125.
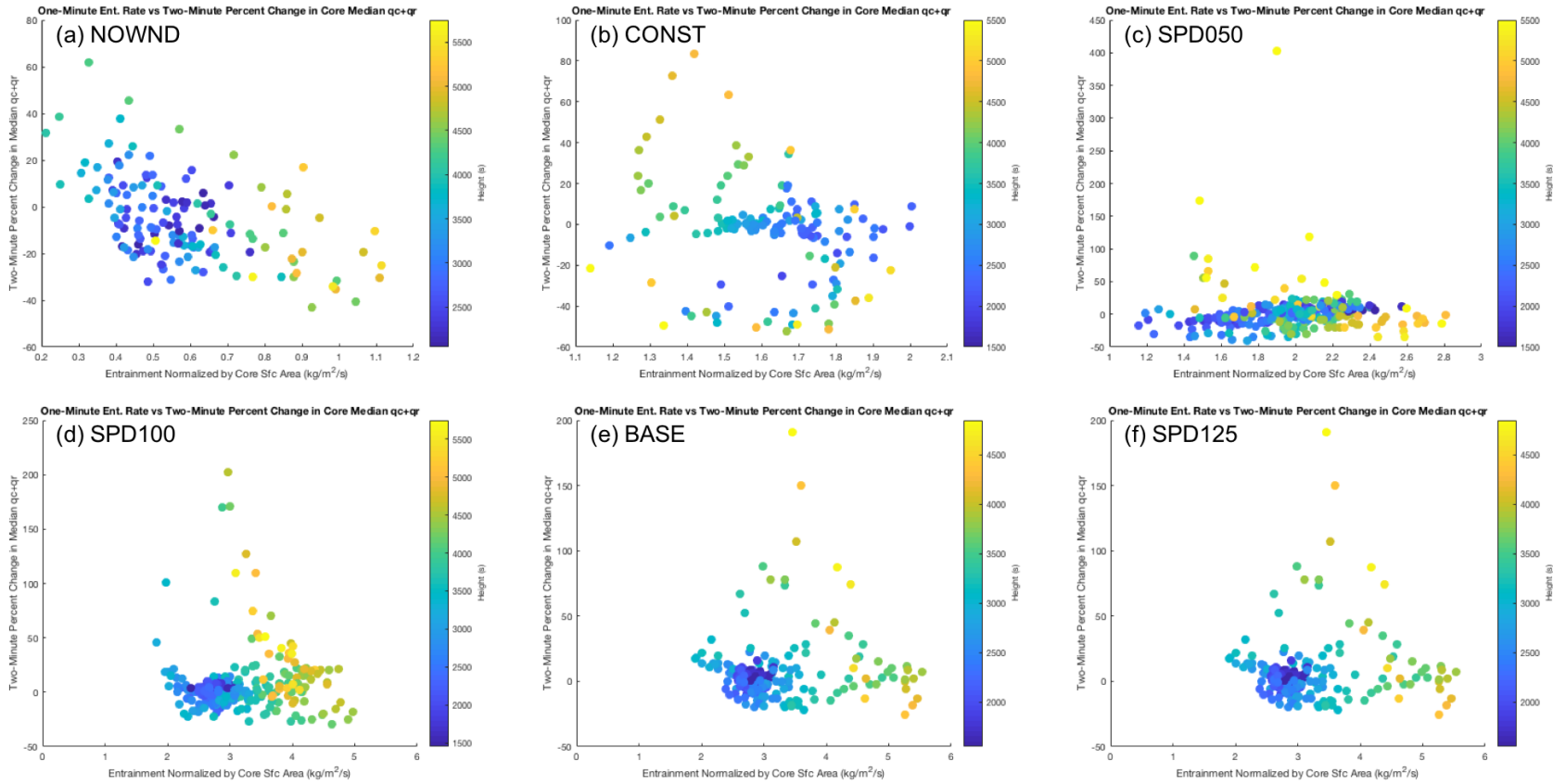
Figure 31. Scatter plots for each simulation of the two-minute percentage change in core median $q_c + q_r$ (ordinate) against E_{SA} (calculated using the perturbation wind) averaged for the first minute of that two-minute period. Each point represents an entire model height level for a two-minute period. Points are colored according to height (in m).
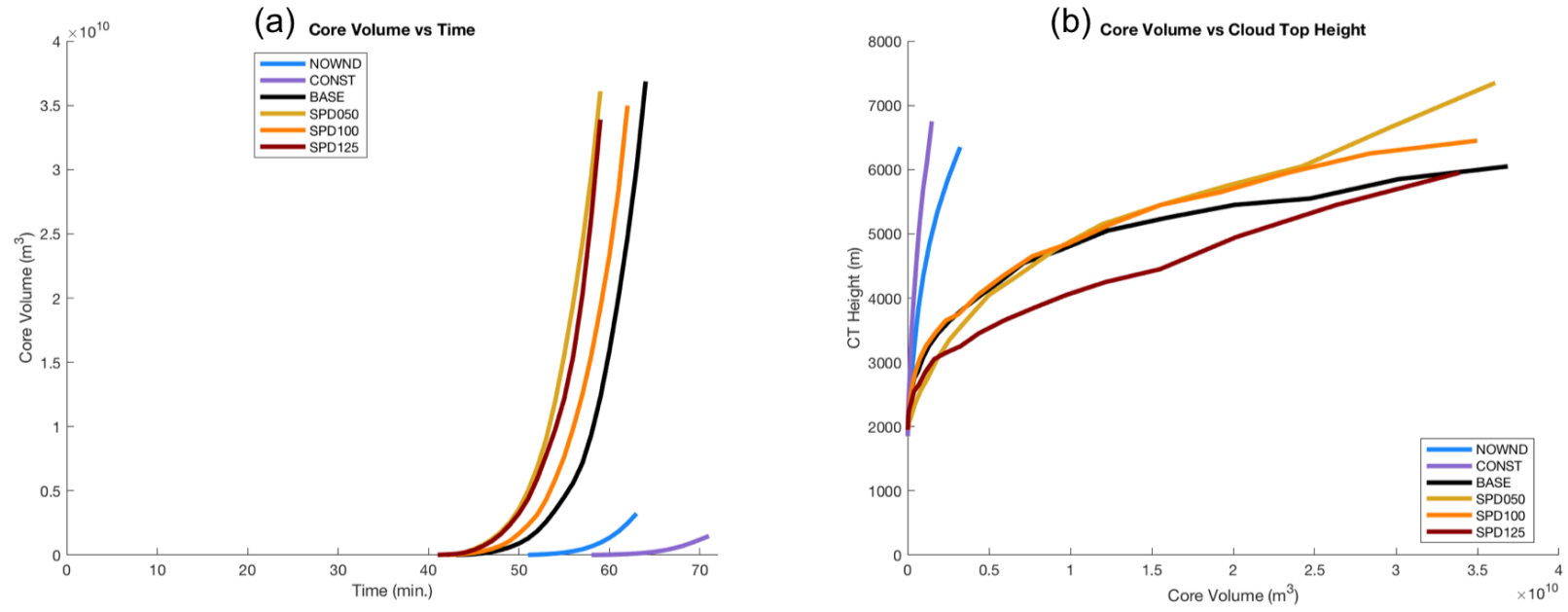
Figure 32. Cloud core volume plotted against (a) time and (b) cloud top height for all simulations.
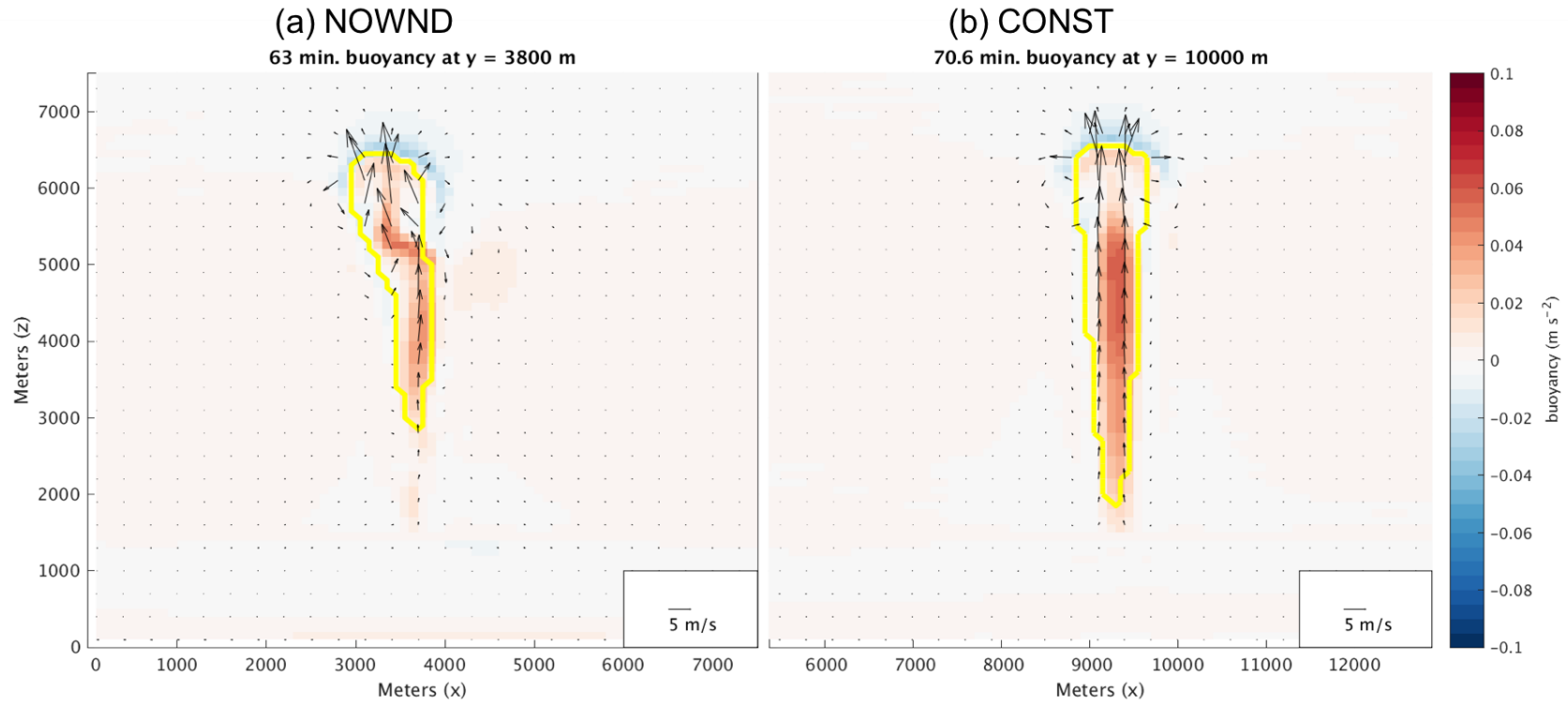
Figure 33. Vertical (west-east) cross-sections of buoyancy, with perturbation wind vectors overlaid, for (a) NOWND and (b) CONST, at times when the cloud top height was roughly 6500 m. Cloud cores outlined in yellow.
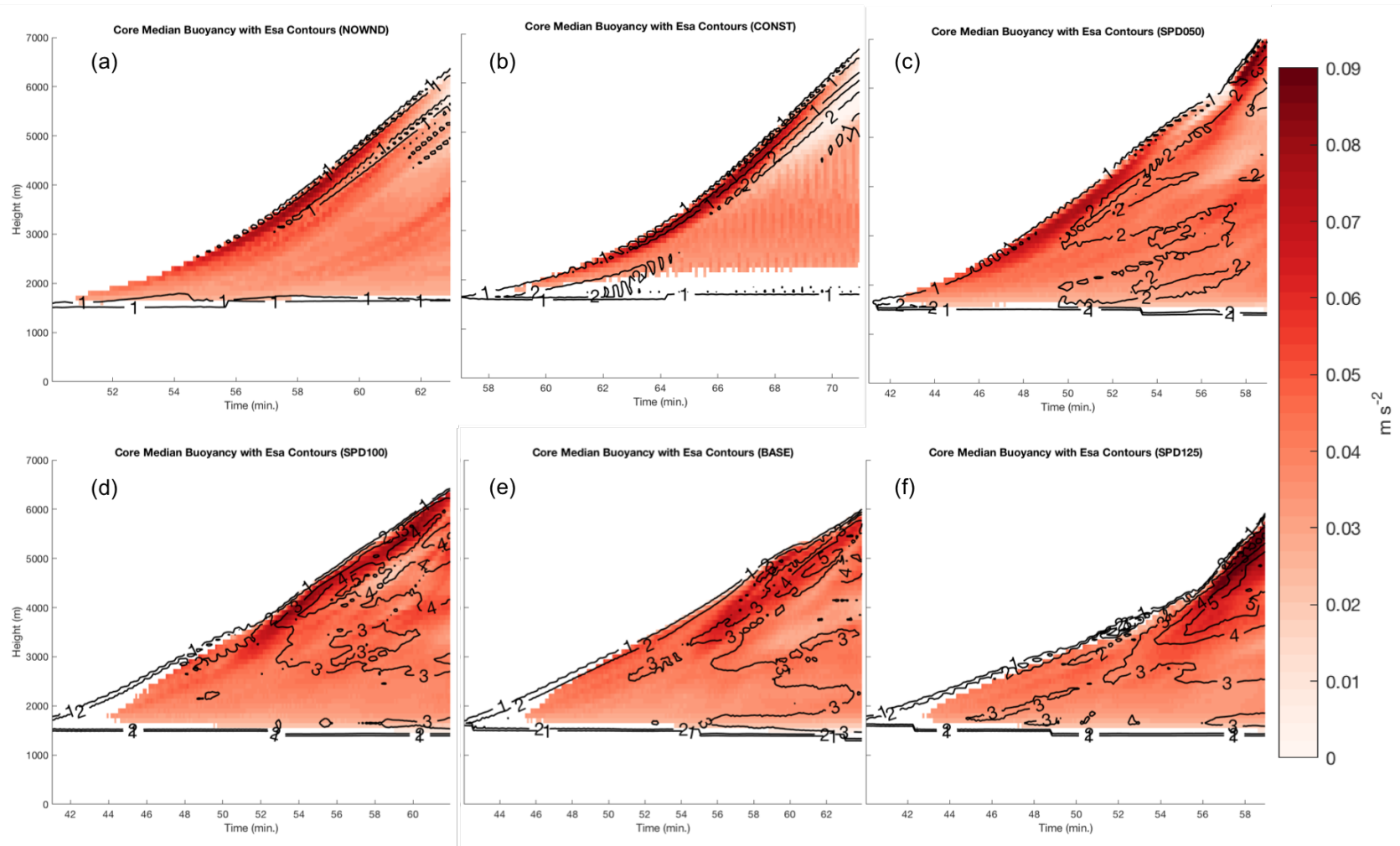
Figure 34. Time-height diagrams of median buoyancy (in m s^{-1}) within the cloud core for (a) NOWND, (b) CONST, (c) SPD050, (d) SPD100, (e) BASE, and (f) SPD125. Contours of instantaneous (i.e. at each 6-second time step) E_{SA}, calculated using the perturbation wind, are overlaid.
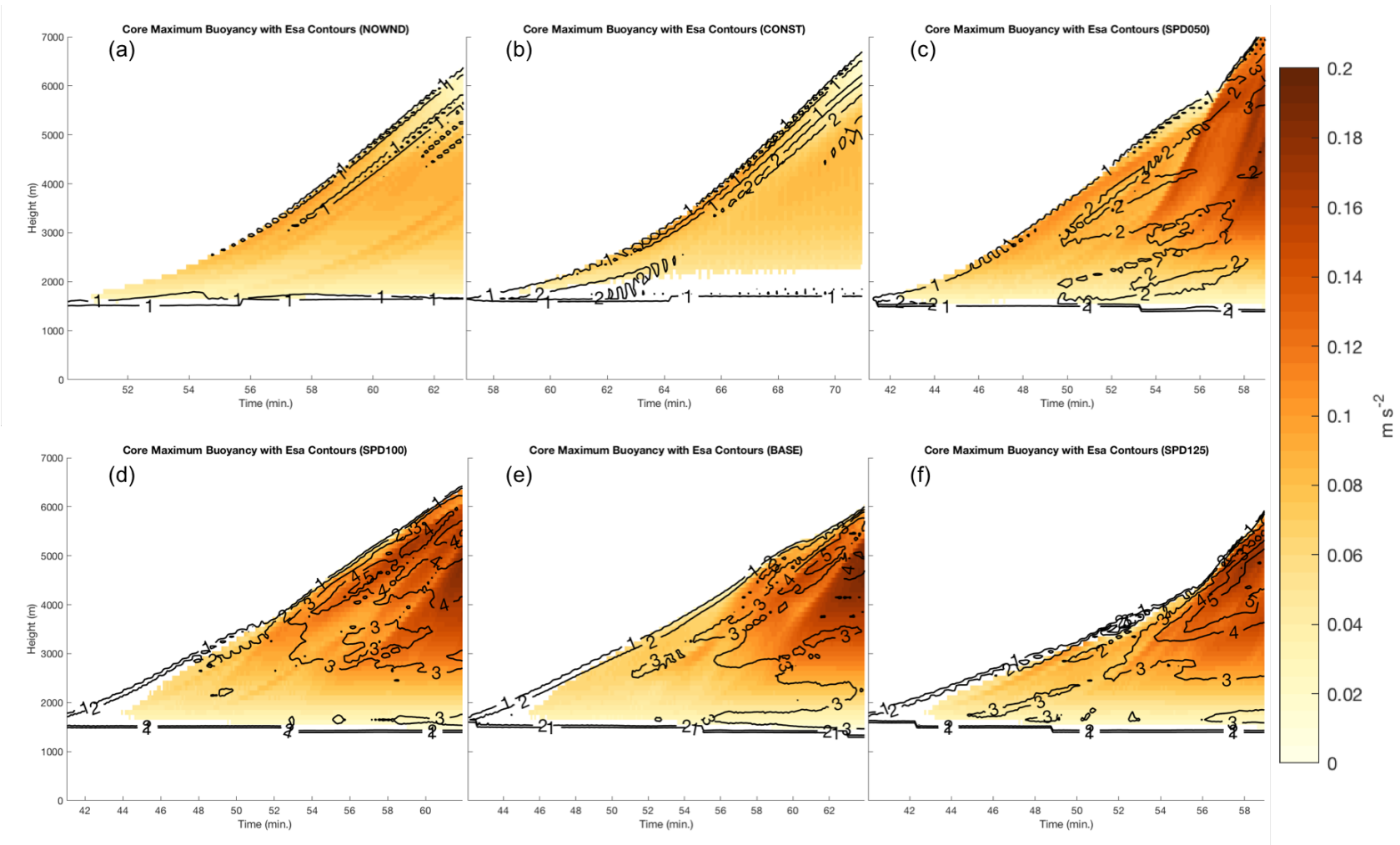
Figure 35. As in Fig. 34, except maximum buoyancy at each time and height.
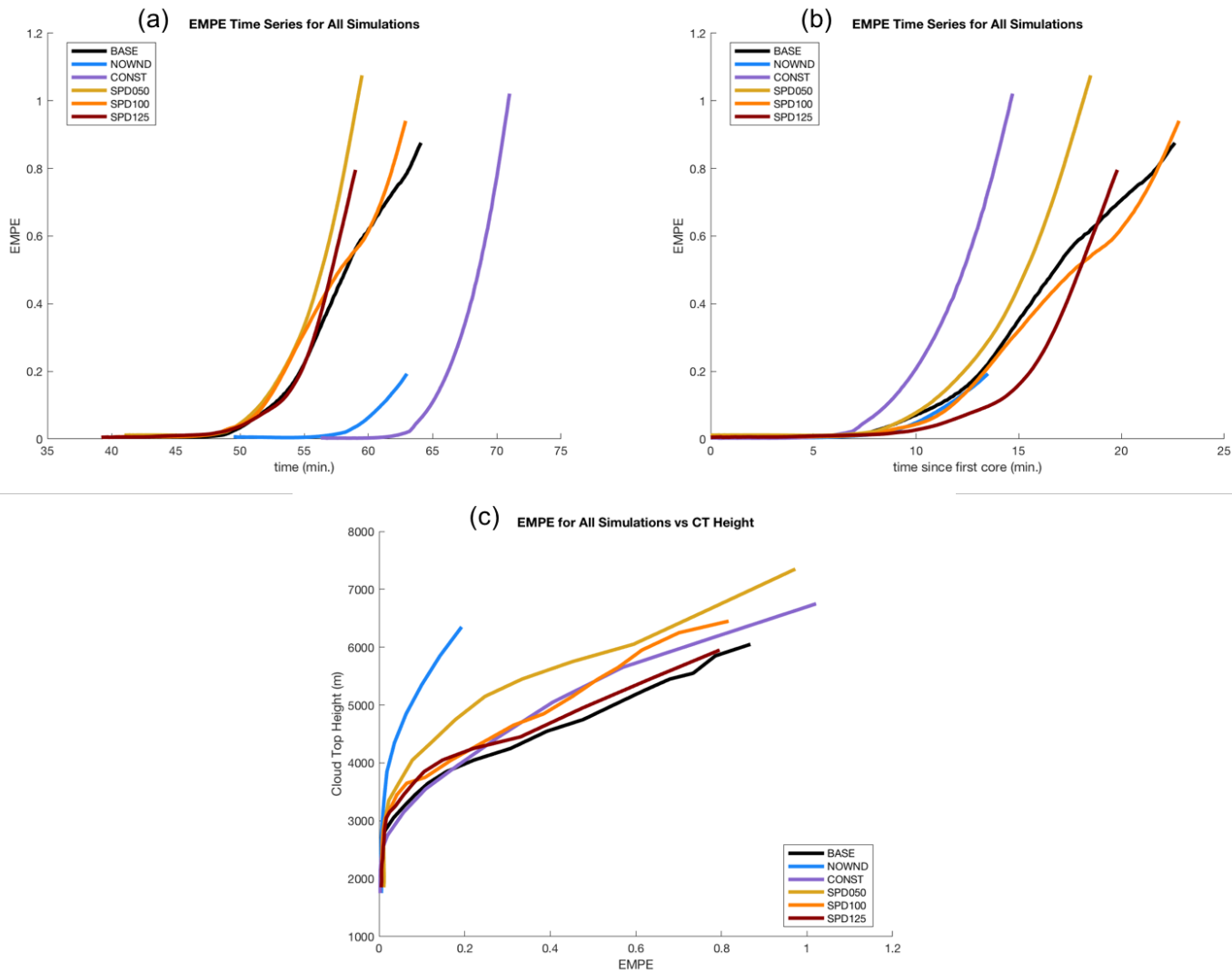
Figure 36. Values of EMPE for all simulations: (a) Time series; (b) As in (a), but time axis shifted to start of cloud core for each simulation; (c) Plotted versus cloud top height.
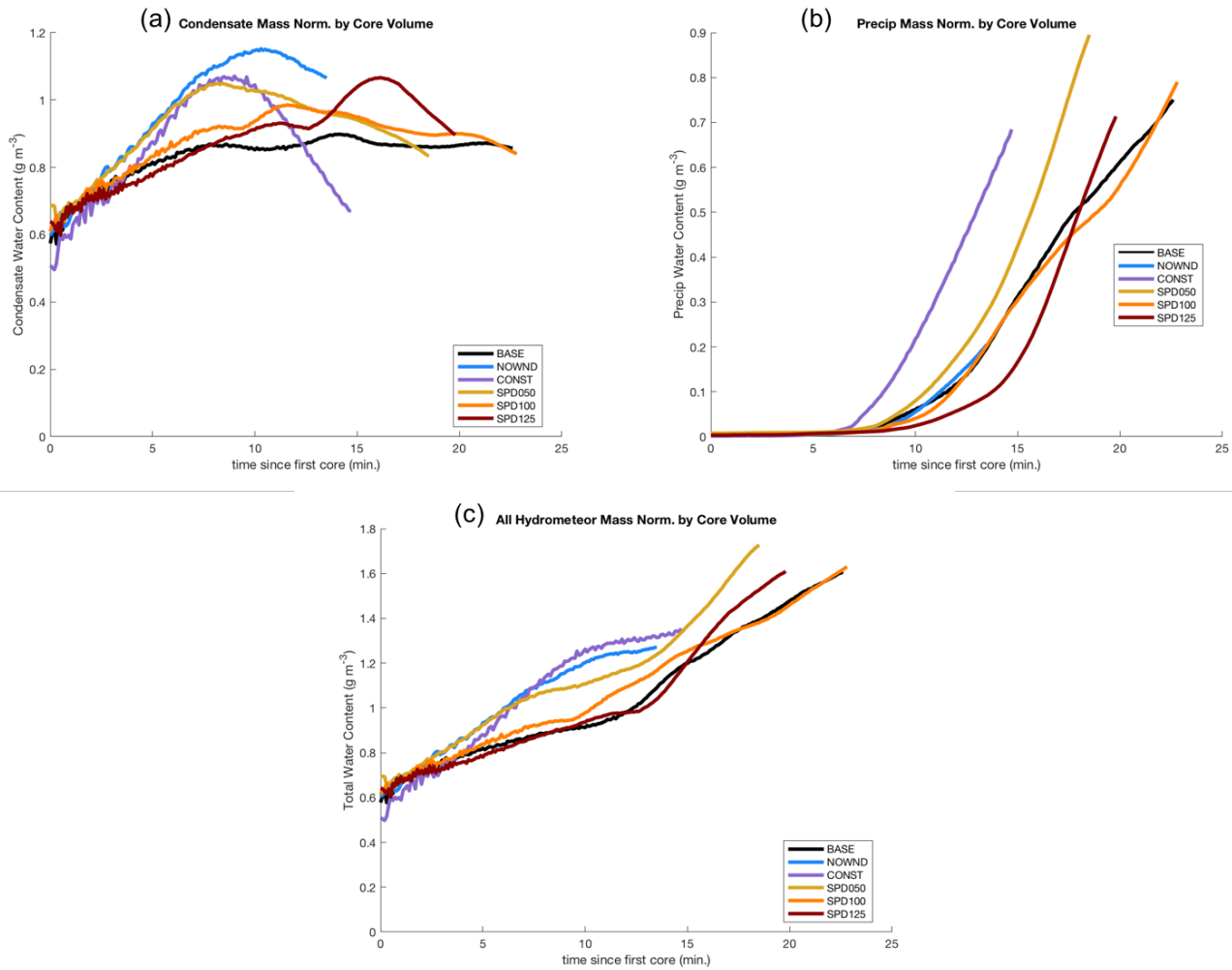
Figure 37. As in Fig. 37b, except for (a) total condensate mass (cloud water and cloud ice), (b) total precipitation mass (rain, hail, graupel, and snow), and (c) total hydrometeor mass (condensate and precipitation). All values normalized by cloud core volume.

CHAPTER 4: CONCLUSIONS

4.1 Summary and Main Findings

Six idealized high-resolution model simulations were conducted to investigate entrainment and its effects in the developing stage of thunderstorms, having environments with different amounts of vertical wind shear. The 0-6 km bulk wind shear values ranged from 0 to 40 m s^{-1}. Entrainment was directly quantified using the mass flux into a cloud core (defined using minimum thresholds of 2 m s^{-1} updraft speed and 0.5 g kg^{-1} hydrometeor mixing ratio), and dilution was quantified using evaporation and sublimation rates directly output from the model, as well as changes in hydrometeor mixing ratios and buoyancy within the cloud cores. Differences precipitation efficiency using the EMPE, i.e., the ratio of the total mass of large hydrometeors to the total mass of smaller hydrometeors within the cloud core, were also investigated as a function of entrainment.

Greater entrainment rates occurred in the simulated thunderstorms growing in stronger shear environments, with a correlation coefficient of 0.99 between the 0-6 km bulk wind shear and the maximum cloud depth-averaged entrainment rate. Equally strong, positive correlations were also found when considering the mass of entrained air normalized by the different cloud core surface areas, or by the vertical mass flux (i.e., fractional entrainment). The trend of more entrainment for greater background shear also held whether the perturbation winds or the total winds were used to calculate entrainment. Calculations with the perturbation winds helped to elucidate that both a stronger P-type circulation and stronger storm-relative inflow on the down-shear side of the cores occurred in the greater shear environments.

Qualitatively, local regions where the cloud core was diluted due to entrainment and mixing could be found in each simulation; however, quantifying the overall effect on the cloud

or the cloud core was more difficult. Regions with high evaporation and sublimation rates were almost always entirely outside the cloud core, likely having changed the location of the core edge, and thus the evaporation and sublimation rates did not provide evidence of the inner cloud core being diluted due to entrainment. There were greater maximum evaporation and sublimation rates for the simulations with stronger background flow, on the down-shear side of the core. The environmental winds led to evaporation and/or sublimation on the upwind side of the core ("environmental evaporation"), but higher rates occurred over only very small regions. Larger regions of reduced hydrometeor mass mixing ratio and buoyancy within the cloud core, associated with entrainment by overturning P-type circulations, could be clearly identified in each simulation. They primarily occurred on the down-shear side of the core in the simulations conducted with vertical wind shear, in addition to enhanced storm-relative inflow.

While regions of the cloud core were clearly diluted with regard to buoyancy and water mass, the altitude-dependent medians and maxima of these quantities often were not reduced substantially in regions of high entrainment values, particularly in the simulations initialized with vertical wind shear. The correlation between the percent change in water mass and entrainment rate was only modest at best, when excluding lower altitudes (below 4000 m). Successive thermals, present only in the shear simulations, not only entrained modified air as they ascended through lower altitudes, but also brought new condensate up to higher altitudes, obscuring some of the evidence of dilution. When no environmental wind was present, multiple thermals were also produced, but did not rise through the remnants of previous thermals. In that case, each was separated by clear air, so despite the lower entrainment rates, dilution of the core was more clear.

The width of the cores in each simulation differed, and this also influenced the degree to which entrainment could dilute them. Entrainment only appeared to affect local regions of each

cloud core, so larger cloud cores in the sheared cases also led to the effects of entrainment being less important.

The rate of precipitation development tended to be slower in the cases with more vertical wind shear, with some exceptions due again to the influence of successive thermals speeding precipitation development, as well as a faster cloud top ascent rate slowing precipitation development. These two effects certainly seemed to be greater than any effect of entrainment on EMPE.

4.2 Limitations and Future Work

Successive thermals common in the shear simulations obscured the effects of entrainment in many cases, and is clearly important in allowing some nascent storms to attain greater depths and precipitate. Growing convection has frequently been observed to contain successive thermals (e.g. Blyth and Latham 1993, French et al. 1999, Damiani et al. 2006), so the process of successive thermals seems to be crucial to convective growth. Successive thermals also complicated any comparison between the shear simulations and the simulations initialized without shear above the cloud base height, however.

Differences in the Gaussian forcing of the clouds were necessary for the different simulations, but this may have impacted some of the results. For simulations with stronger initial environmental winds, stronger forcing was needed, as the parcels heated by the forcing would be advected away from its location more quickly. Thus, there was less time for those parcels to be heated by the forcing. In addition, a stronger downward-oriented dynamic pressure acceleration occurs in clouds growing in stronger-shear environments (Peters et al. 2019), necessitating greater heating to overcome it. Thus, differences in forcing among the simulations used here

83

contributed to differences in the cloud vigor, with regard to updraft strength and possibly even liquid water content.

The grid spacing of 100 m for these simulations was chosen for practical reasons, as smaller grid spacing values would increase the computational expenses of this study greatly. However, it was unclear if 100 m was small enough for entrainment and its effects to be suitably represented in the model. Cumulative integrated entrainment values did not completely converge as the grid spacing was reduced to 100 m (Appendix A). A smaller grid spacing may result in the model representing a number of smaller eddies still critical for entrainment, and thus possibly increasing the amount of entrainment from that represented here.

The algorithm used to calculate entrainment itself presented some limitations on this study. Values of entrainment rate were always horizontally-averaged, while dilution was found to often only affect portions of any given vertical level of the cloud core. Entrainment rate values at each model grid point could have allowed for a clearer connection between entrainment and dilution than the one presented in this study.

In addition to these limitations, there are additional questions which could be answered by future work, including different methods which could improve the robustness of these results. Such possibilities are discussed in the following sub-sections.

4.2.1 Drier Environmental Sounding

The thermodynamic profile used in each simulation was fairly moist throughout the depth of the domain. The temperature and dew point did not differ by more than 10 K at any altitude. This profile, therefore, might not be the most realistic for studying growing convection, in particular entrainment and its effects. This thermodynamic profile is quite unstable, in part due to

the high moisture content of the atmosphere, and thus convection grows fairly rapidly, and this might mask some of the effects of entrainment as storms grow regardless of those effects.

One possible solution would be to modify the atmospheric moisture content in the environmental sounding. One possible sounding was tested, in which the water vapor mixing ratio (q_v) was reduced by 10% from the environment used in this study. Attempts to simulate a storm with this profile were unsuccessful, however, as there was difficulty in initiating convection. Engelsen (2018) proposed inserting "dry layers" into the sounding at different altitudes, and this might be more useful for evaluating the effects of entrainment of air with different properties into the cloud core.

4.2.2 Additional Wind Profiles

Another possible question to be addressed in future work is if "turning" of the hodograph has any effect on entrainment. In this study, BASE and SPD100 were initialized with wind profiles that were identical in magnitude, but BASE had low-level turning of the hodograph while SPD100 did not. This did not cause any notable differences in entrainment. However, all of the hodograph turning in BASE was below the cloud base altitude. A future investigation of possible differences in entrainment for a storm growing in an environment with hodograph turning in the cloud layer is warranted.

4.2.3 Alternative Measures of Precipitation Efficiency

The results of this work have shown that EMPE changes quite rapidly with time, or in other words, EMPE is sensitive to the length of time the cloud has been present in a given simulation. As a result, one simulation which had a substantial length of time with a cloud

present before it began to deepen substantially, had a very high EMPE during its developing stage relative to the developing stages of the other simulations. Successive thermals also had a large effect on EMPE, which enabled the shear simulations to have a greater EMPE than expected, despite the higher entrainment rates in those simulations. An exploration of different measures of precipitation efficiency or productivity is an important research direction to pursue, in order to better relate entrainment to precipitation production.

REFERENCES

Blyth, A. M., 1993: Entrainment in Cumulus Clouds. *J. Applied Meteorology*, 32, 626-641, doi:10.1175/1520-0450(1993)032<0626:EICC>2.0.CO;2.

— —, W. A. Cooper, and J. B. Jensen, 1988: A study of the Source of Entrained Air in Montana Cumuli. *J. Atmos. Sci.*, 45, 3944-3964, doi:10.1175/1520-0469(1988)045<3944:ASOTSO>2.0.CO;2.

— —, S. G. Lasher-Trapp, and W. A. Cooper, 2005: A study of thermals in cumulus clouds. *Q. J. R. Meteorol. Soc.*, 131, 1171–1190, doi:10.1256/qj.03.180.

— —, and J. Latham, 1993: Development of ice and precipitation in New Mexican summertime cumulus clouds. *Q. J. R. Meteorol. Soc.,* 119, 91-120, doi:10.1002/qj.49711950905.

Bryan, G. H. and J. M. Fritsch, 2002: A Benchmark Simulation for Moist Nonhydrostatic Numerical Models. *Mon. Wea. Rev.*, 130, 2917-2928, doi:10.1175/1520-0493(2002)130<2917:ABSFMN>2.0.CO;2.

Carpenter, R. L., K. K. Droegemeier, and A. M. Blyth, 1998: Entrainment and Detrainment in Numerically Simulated Cumulus Congestus Clouds. Part I: General Results. *J. Atmos. Sci.*, 55, 3417–3432, doi:10.1175/1520-0469(1998)055<3417:EADINS>2.0.CO;2.

Cooper, W. A., 1989: Effects of Variable Droplet Growth Histories on Droplet Size

    Distributions. Part I: Theory. *J. Atmos. Sci.*, 46, 1301-1311, doi:10.1175/1520-

    0469(1989)046<1301:EOVDGH>2.0.CO;2.

— —, S. G. Lasher-Trapp, A. M. Blyth, 2013: The Influence of Entrainment and Mixing on the

    Initial Formation of Rain in a Warm Cumulus Cloud. *J. Atmos. Sci.*, 70, 1727-1743,

    doi:10.1175/JAS-D-12-0128.1.

Damiani, R., G. Vali, and S. Haimov, 2006: The Structure of Thermals in Cumulus from

    Airborne Dual-Doppler Radar Observations. *J. Atmos. Sci.,* 63, 1432-1450,

    doi:10.1175/JAS3701.1.

Dawe, J. T., and P. H. Austin, 2011: Interpolation of LES Cloud Surfaces for Use in Direct

    Calculations of Entrainment and Detrainment. Mon. Weather Rev., 139, 444–456,

    doi:10.1175/2010MWR3473.1.

Deardorff, J. W., 1980: Stratocumulus-capped mixed layer derived from a three-dimensional

    model. *Bound. Layer Meteor.*, 18, 495–527.

Del Genio, A. D., 2012: Representing the Sensitivity of Convective Cloud Systems to

    Tropospheric Humidity in General Circulation Models. *Surv. Geophys.,* 33, 637-656,

    doi:10.1002/qj.828.

Derbyshire, S. H., I. Beau, P. Bechtold, J.-Y. Grandpeix, J.-M. Piriou, J.-L. Redelsperger, and P. M. M. Soares, 2004: Sensitivity of moist convection to environmental humidity. *Q. J. R. Met. Soc.*, 130, 3055-3079, doi:10.1256/qj.03.130.

de Rooy, W. C., P. Bechtold, K. Fröhlich, C. Hohenegger, H. Jonker, D. Mironov, A. P. Siebesma, J. Teiceira, and J. Yano, 2013: Entrainment and detrainment in cumulus convection: an overview. *Q. J. R. Meteorol. Soc.*, 139, 1-19, doi:10.1002/qj.1959.

Engelsen, B. N., 2018: The Effects of Entrainment in the Developing and Rotating Stages of Supercell Thunderstorms. M.S. thesis, Dept. of Atmospheric Sciences, University of Illinois at Urbana-Champaign, 59 pp.

French, J. R., G. Vali, R. D. Kelly, 1999: Evolution of Small Cumulus Clouds in Florida: Observations of Pulsating Growth. *Atmos. Research*, 52, 143-165, doi:10.1016/S0169-8095(99)00024-1.

Grabowski, W. W., and H. Pawlowska, 1993: Entrainment and Mixing in Clouds: The Paluch Mixing Diagram Revisited. *J. Appl. Meteor.*, 32, 1767-1773, doi:10.1175/1520-0450(1993)032<1767:EAMICT>2.0.CO;2.

Hannah, W. M., 2017: Entrainment versus Dilution in Tropical Deep Convection. *J. Atmos. Sci.*, 74, 3725-3747, doi:10.1175/JAS-D-16-0169.1.

Heus, T, G. van Dijk, H. J. J. Jonker, H. E. A. van den Akker, 2008: Mixing in Shallow Cumulus
Clouds Studied by Lagrangian Particle Tracking. *J. Atmos. Sci.*, 65, 2581-2597,
doi:10.1175/2008JAS2572.1.

Jonas, P. R., and B. J. Mason, 1982: Entrainment and the droplet spectrum in cumulus clouds. *Q.
J. R. Met. Soc.,* 108, 857-869, doi:10.1002/qj.49710845808.

Kirschbaum, D. J., 2011: Cloud-Resolving Simulations of Deep Convection over a Heated
Mountain. *J. Atmos. Sci.*, 68, 361-378, doi:10.1175/2010JAS3642.1.

Kitchen, M., and S. J. Caughey, 1981: Tethered-balloon observations of the structure of small
cumulus clouds. *Q. J. R. Meteorol. Soc.*, 107, 853–874, doi:10.1002/qj.49710745407.

Klemp, J. B., and R. B. Wilhelmson, 1978: The Simulation of Three-Dimensional Convective
Storm Dynamics. *J. Atmos. Sci.*, 35, 1070–1096, doi:10.1175/1520-
0469(1978)035<1070:TSOTDC>2.0.CO;2.

Klocke, D., R. Pincus, and J. Quaas, 2011, On constraining estimates of climate sensitivity with
present-day observations through model weighting, *J. Clim.*, 24(23), 6092–6099.
doi:10.1175/2011JCLI4193.1.

Knight, C. G., et al., 2007, Association of parameter, software, and hardware variation with large-scale behavior across 57,000 climate models, *Proc. Natl. Acad. Sci. U. S. A.*, 104(30), 12,259–12,264, doi:10.1073/pnas.0608144104.

LaMontagne, R. G., and J. W. Telford, 1983: Cloud Top Mixing in Small Cumuli. *J. Atmos. Sci.*, 40, 2148-2156, doi:10.1175/1520-0469(1983)040<2148:CTMISC>2.0.CO;2.

Lasher-Trapp, S. G., W. A. Cooper, and A. M. Blyth, 2005: Broadening of droplet size distributions from entrainment and mixing in a cumulus cloud. *Q. J. R. Meteorol. Soc.,* 131, 195-220, doi:10.1256/qj.03.199.

Malkus, J. S., 1949: Effects of wind shear on some aspects of convection, *Eos Trans. AGU*, 30, 19-25, doi:10.1029/TR030i001p00019.

— —, 1954: SOME RESULTS OF A TRADE-CUMULUS CLOUD INVESTIGATION. *J. Meteorology*, 11, 220-237, doi:10.1175/1520-0469(1954)011<0220:SROATC>2.0.CO;2.

— —, and R. S. Scorer, 1955: THE EROSION OF CUMULUS TOWERS. *J. Meteorology,* 12, 43-57, doi:10.1175/1520-0469(1955)012<0000:TEOCT>2.0.CO;2.

Mansell, E. R., C. L. Ziegler, and E. C. Bruning, 2010: Simulated Electrification of a Small Thunderstorm with Two-Moment Bulk Microphysics. *J. Atmos. Sci.*, 67, 171-194, doi:10.1175/2009JAS2965.1.

91

Morton, B. R., G. Taylor, and J. S. Turner, 1956: Turbulent gravitational convection from maintained and instantaneous sources. *Proc. Roy. Soc. London*, A234, 1-23.

Moser, D. H., and S. Lasher-Trapp, 2017: The influence of successive thermals on entrainment and dilution in a simulated cumulus congestus. *J. Atmos. Sci.,* 74, 375– 392, doi: 10.1175/JAS-D-16-0144.1.

Naylor, J., M. S. Gilmore, R. L. Thompson, R. Edwards, and R. B. Wilhelmson, 2012: Comparison of Objective Supercell Identification Techniques Using an Idealized Cloud Model. *Mon. Weather Rev.*, 140, 2090-2102, doi:10.1175/MWR-D-11-00209.1.

Paluch, I. R., 1979: The Entrainment Mechanism in Colorado Cumuli. *J. Atmos. Sci.*, 36, 2467-2478, doi:10.1175/1520-0469(1979)036<2467:TEMICC>2.0.CO;2.

Peters, J. M., W. Hannah, and H. Morrison, 2019: The Influence of Vertical Wind Shear on Moist Thermals. *J. Atmos. Sci.*, 76, 1645-1659. doi:10.1175/JAS-D-18-0296.1.

Romps, D. M., 2010: A Direct Measure of Entrainment. *J. Atmos. Sci.,* 67, 1908-1927, doi:10.1175/2010JAS3371.1.

— —, and Kuang, Z., 2010: Nature versus Nurture in Shallow Convection. *J. Atmos. Sci.*, 67, 1655-1666, doi:10.1175/2009JAS3307.1.

Saunders, P. M., 1961: An Observational Study of Cumulus. *J. Meteorology*, 18, 451-467, doi:10.1175/1520-0469(1961)018<0451:AOSOC>2.0.CO;2.

Scorer, R. S., 1957: Experiments on convection of isolated masses of buoyant fluid. *J. Fluid Mech.*, 2, 583-594, doi:10.1017/S0022112057000397.

— —, and F. H. Ludlam, 1953: Bubble theory of penetrative convection. *Q. J. R. Meteorol. Soc.,* 79, 94–103, doi:10.1002/qj.49707933908.

Siebesma, A. P., and J. W. M. Cuijpers, 1995: Evaluation of Parametric Assumptions for Shallow Cumulus Convection. *J. Atmos. Sci*., 52, 650-666, doi:10.1175/1520-0469(1995)052<0650:EOPAFS>2.0.CO;2.

Squires, P, 1958: Penetrative Downdrafts in Cumuli. *Tellus,* 10, 381-389, doi:10.3402/tellusa.v10i3.9243.

Stommel, H, 1947: Entrainment of Air into a Cumulus Cloud. *J. Meteorology,* 4, 91-94, doi:10.1175/1520-0469(1947)004%3C0091:EOAIAC%3E2.0.CO;2.

Turner, J. S., 1962: The 'starting plume' in neutral surroundings. *J. Fluid Mech*., 13, 356-368, doi:10.1017/S0022112062000762.

Warner, J., 1955: The Water Content of Cumuliform Cloud. *Tellus*, 7, 449-457, doi:10.1111/j.2153-3490.1955.tb01183.x.

Weisman, M. L., and J. B. Klemp, 1982: The Dependence of Numerically Simulated Convective Storms on Vertical Wind Shear and Buoyancy. *Mon. Wea. Rev.,* 110, 504-520, doi:10.1175/1520-0493(1982)110<0504:TDONSC>2.0.CO;2.

——, and J. B. Klemp, 1984: The Structure for Classification of Numerically Simulated Convective Storms in Directionally Varying Wind Shears. *Mon. Wea. Rev.,* 112, 2479-2498. doi:10.1175/1520-0493(1984)112<2479:TSACON>2.0.CO;2.

Woodward, B., 1959: The motion in and around isolated thermals. *Q. J. R. Met. Soc.,* 85, 144-151, doi:10.1002/qj.49708536407.

Zhao, M., and P. H. Austin, 2005: Life Cycle of Numerically Simulated Shallow Cumulus Clouds. Part II: Mixing Dynamics. *J. Atmos. Sci.,* 62, 1291-1310, doi:https://doi.org/10.1175/JAS3415.1.

APPENDIX A: SENSITIVITY TO MODEL RESOLUTION

Tests were conducted in order to evaluate the effect of grid spacing upon the quantified entrainment. Previous numerical modeling studies of entrainment have used grid spacing values for smaller cumuli of 25 m (e.g. Dawe and Austin 2011, Cooper et al. 2013) or 50 m (e.g. Carpenter et al. 1998, Romps 2010, Moser and Lasher-Trapp 2017, 2018), and for larger convective storms of 100 m (e.g. Engelsen 2018, Peters et al. 2019). The relatively large scale of clouds necessitated a larger model domain in simulations with wind shear used in this study; environmental winds cannot be "subtracted out" to retain the storm within the model domain as in other studies, as it affects the entrainment calculations. For practicality, larger grid spacing was desired in order to limit computational expense. However, a sufficiently small grid spacing to resolve the eddies producing most of the entrainment was required.

Therefore, simulations were performed at three different grid spacing values: 100 m, 200 m, and 500 m. (Grid spacing less than 100 m was not deemed practical for the many simulations required for this study). These simulations will be referred to as 100M_BASE, 200M_BASE, and 500M_BASE, respectively. All of these simulations were identical, using the sounding and model parameters from the general base case used in the main study (100M_BASE), except for differences in the grid spacing and the peak value of the Gaussian heat flux used for convective initiation (H_g, see Section 2.1). Stronger forcing was necessary to initiate convection in simulations with coarser grid spacing because the energy applied to a grid cell by the forcing is dispersed over a larger volume. The peak values of H_g were 500 W m^{-2}, 650 W m^{-2}, and 800 W m^{-2} for the 100M_BASE, 200M_BASE, and 500M_BASE simulations, respectively.

In order to assess the effects of the grid spacing upon entrainment, both E_{SA} and integrated entrainment values ($E_{SA,t}$, $E_{SA,total}$, and E_{total}) were used, as described in Section 2.3

and Section 2.4. The cloud core definition was identical for all simulations. Plots of the cloud top height versus time are shown in Figure A.1. At all times, the coarsest resolution simulation had the highest cloud top, and the highest resolution simulation had the lowest cloud top, a result of both the different forcing that had to be used to initiate the storm, as well as differences in entrainment.

Different values of entrainment, calculated with the perturbation winds, are plotted versus cloud top height in Fig. A.2, and show some clear trends. The entrainment rate is often larger for the coarsest resolution run (Fig. A.2.a), but does not start until the cloud top is higher than in the other runs. For cloud top heights below 2.75 km, the 100 m grid spacing simulation has the greatest entrainment rate, which is expected as the most eddies are being resolved, and the entrainment rate for the 500 m simulation is zero. For cloud top heights above approximately 3 km, the 500 m grid spacing simulation tends to have the highest entrainment rate. This is because the smallest resolved eddies with 500 m grid spacing are much larger than those in the higher resolution simulations. As a result, these eddies take more time to begin overturning, but entrain more air than the smaller eddies, once they do begin overturning. Above 3 km cloud top height until the end of the developing stage, $E_{SA,t}$ varies among the simulations between 2.4 kg m^{-2} s^{-1} and 3.5 kg m^{-2} s^{-1}, with no clear relationship as a function of grid spacing except for the delayed start in the 500M_BASE simulation.

However, cumulative values of entrainment (Fig. A.2b,c) illustrate the expected relationship: the entrained mass is generally greater in 100M_BASE, and the least in 500M_BASE, with 200M_BASE lying in between the two extremes. Although the entrainment rates are greater at later stages in the 500M_BASE run, the initial entrainment rates (i.e. at lower cloud top heights) are greatest for the 100M_BASE run. Entrainment has had more time to act on

the cloud in that simulation up to a given cloud top height (Fig. A.1). By the end of the

developing stage, approximately 33% more mass per unit surface area was entrained into the

cloud core in 100M_BASE than in 200M_BASE. This result indicates that grid spacing of 100 m

or smaller is likely necessary for evaluating entrainment in the environments studied, as the

results had not yet converged for 100 m grid spacing. Bryan et al. (2003) evaluated the turbulent

kinetic energy (TKE) trends in simulated deep convection versus the grid spacing used, and

found that the ratio of subgrid TKE to total TKE decreased with decreasing grid spacing

(between 1000 m and 125 m) for simulations of squall line convection. At 125 m grid spacing,

Bryan et al. (2003) found that this ratio slightly exceeded 10% in parts of the convective region,

which is generally appropriate for LES studies. This result affirms that a grid spacing of $O(100$

m) should be appropriate for investigating entrainment due to turbulent eddies in deep

convection. Given the size of the domain and duration of the simulations, a grid spacing of less
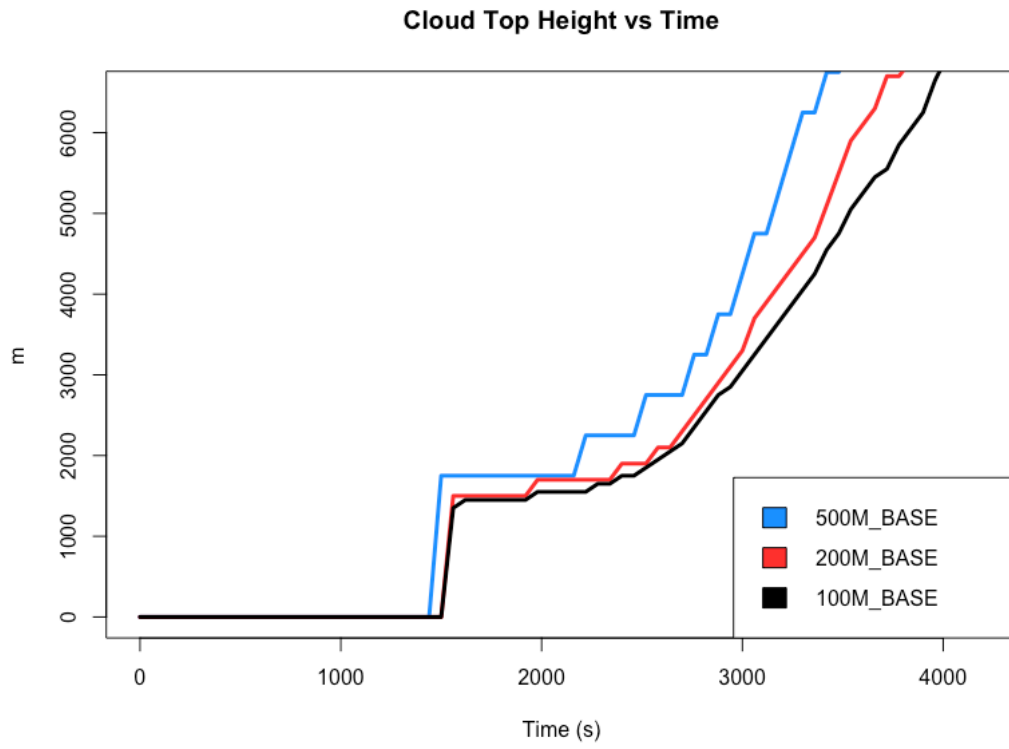
than 100 m was not practical.

Figure A.1. Time series of cloud top height for simulations with different grid spacing using the
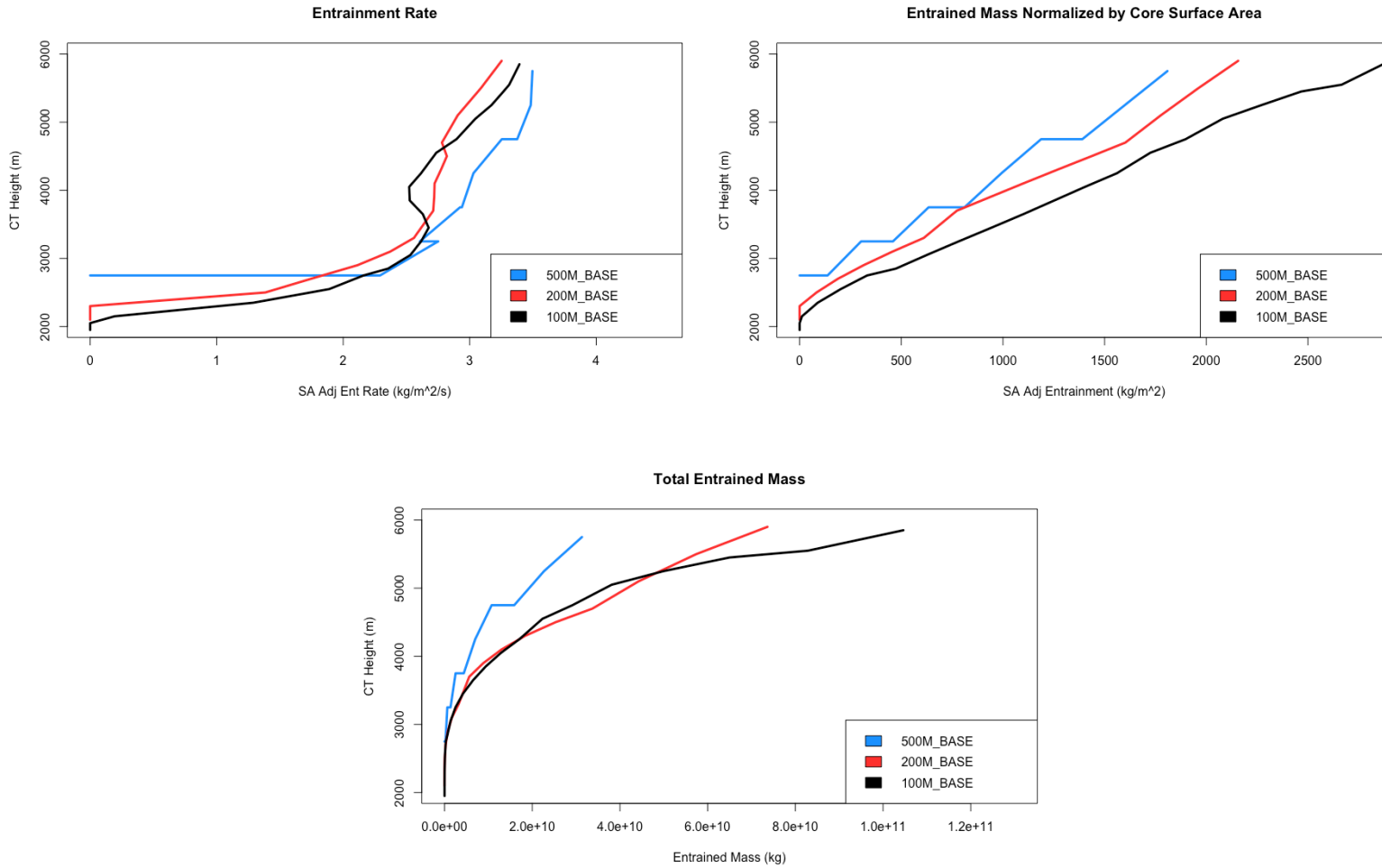
sounding from BASE.

Figure A.2. Plots of integrated entrainment (using perturbation winds) versus cloud top height, for simulations of BASE conducted with grid spacing at the values indicated: (a) Entrainment rate $E_{SA,t}$; (b) Cumulative entrained mass normalized by core surface area $E_{SA,total}$; (c) Cumulative total entrained air mass E_{total}.